Summer 2024

In-Depth Characterization of the Selective Oxidation Products of Hafnium Carbide

Jonathan Allen Scott
Missouri University of Science and Technology

Department: Materials Science and Engineering

IN-DEPTH CHARACTERIZATION OF THE SELECTIVE OXIDATION PRODUCTS OF HAFNIUM CARBIDE

by

JONATHAN ALLEN SCOTT

A DISSERTATION

Presented to the Graduate Faculty of the

MISSOURI UNIVERSITY OF SCIENCE AND TECHNOLOGY

In Partial Fulfillment of the Requirements for the Degree

DOCTOR OF PHILOSOPHY

in

Materials Science and Engineering

2024

Approved by:

Dr. David Lipke, Advisor
Dr. William Fahrenholtz
Dr. Ronald O'Malley
Dr. F Scott Miller
Dr. Xiaoqing He

PUBLICATION DISSERTATION OPTION

This dissertation consists of the following three articles, formatted in the style used by the Missouri University of Science and Technology:

Paper I, found on pages 26-55 “The Role of Microstructure on High Temperature Oxidation Behavior of Hafnium Carbide,” was published in the *Journal of the American Ceramic Society* in volume 106 Issue 5 in 2022.

Paper II, found on pages 56-72 “High Temperature Oxidation Regime Transitions in Hafnium Carbide,” was submitted for publication in the *Journal of the American Ceramic Society,* in January 2024.

Paper III, found on pages 73-94 “Enthalpies of Formation of Hafnium Carbides and Nitrides by Combustion Calorimetry,” is intended for submission to the *Journal of Solid State Chemistry*.

ABSTRACT

Materials capable of withstanding oxidative environments at temperatures >2000°C are necessary for hypersonic applications. Hafnium carbide (HfC) shows a combination of properties that lends itself toward these applications; however, its oxidation behavior is poorly understood. At 1300°C, HfC was found to oxidize via the following mechanism: 1) Initial oxidation of both C and Hf present in the system, 2) Formation of an interconnected pore network, whose size is related to the volume of gases being generated during the oxidation process, 3) Growth of the oxide scale to become sufficiently protective, 4) Formation of an initially amorphous "HfO_2C" at the interface between the protective scale and the parent carbide material, on the order of nanometers, 5) subsequent decomposition of "HfO_2C" into nanocrystalline HfO_2 and turbostratic C, leading to nanoscale microstructures that are responsible for the observed gas phase diffusion-controlled oxidation kinetics. The oxidation of HfC at T > 1800°C developed oxide scales containing only HfO_2; oxidation behavior of this material appeared to change between 1600°C-1800°C. Microstructural observations of the oxide scales formed indicated a change in oxidation regime from gas-phase-controlled to solid-state diffusion controlled. This transition was found to correlate with the max range of the thermodynamically predicted HfO_2 + C interlayer, which was affected by carbon substoichiometry of the system. The maximum predicted HfO_2 + C stability was calculated to be 2070°C for highly substoichiometric HfC, providing a theoretical mechanism for extending gas-phase diffusion limited oxidation control to higher temperatures. Investigations of the enthalpies of formation of HfC_{1-x} and HfN_{1-y} showed good agreement with theoretical predictions.

ACKNOWLEDGMENTS

I would like to begin by thanking my immediate friends and family for their constant enthusiasm and motivation in getting me across the finish line. Without their support, I would undoubtedly have been unsuccessful in my completion of the dissertation.

I would also like to extend thanks to Dr. Gregory Hilmas, Dr. William Fahrenholtz and Dr. Paul Brune for allowing me to begin my career as an undergraduate researcher. I would like to extend a special thank you to Dr. Jeremy Watts and Dr. Kelley Wilkerson for their unwavering support and dedication to the success of all students. A special thanks to Amelia Martinez and Brennan Long is warranted for their immense help with research.

I would be remiss to not thank the fellow researchers that I worked alongside in the ultrahigh temperature ceramics group, namely Anna Dorner, Austin and Anna Stanfield, Evan and Rachel Schwind and Paul Brune. In addition to the previous researchers, I thank my current research group members: you all provided constant encouragement, stimulating discussions, and generally put up with me on a day-to-day basis. Dr. Bohannan, your technical expertise in XRD is only matched by your humor.

To my fellow CoorsTek employees, especially Denton Reel, Jackson Langhout and Brandon Pilcher, thank you for your constant (if sometimes nagging) support and encouragement, even if I don't always show a "higher level of thinking".

And to Jamie Young, your constant support and compassion, even through all of the trials and tribulations of life, have served as an anchor for me. I quite literally could not have done this without you by my side. There are not enough words to express my thanks. Thank you for everything.

TABLE OF CONTENTS

LIST OF ILLUSTRATIONS

SECTION Page

LIST OF TABLES

1. INTRODUCTION

This dissertation describes investigations into the nature of oxidation of hafnium carbide (HfC) as a function of temperature and stoichiometry.

The main thrust for this research is for the development of materials for extreme environments. There is a burgeoning need for reusable, controllable hypersonic flight vehicles, which require structural materials that can withstand extreme temperatures and oxidative environments. Currently, the state-of-the-art for hypersonic applications is some combination of C or SiC in a fiber-reinforced composite, which is ultimately limited in service temperatures to ~1700°C, restricting available flight trajectories. The limitation in service temperature is related to the oxidation behavior of these composites. C composites that do not contain SiC exhibit aggressive oxidation at high temperatures due to the lack of a protective oxide scale. For SiC-containing composites, this temperature limitation reflects when volatilization of the passivating oxide scale can occur, which results in a lack of protection of the underlying material to the oxidizing atmosphere.

Investigations into the oxidation behavior of HfC in past studies showed the formation of a dense, intermediate layer whose properties were indicative of a stable, refractory material that served to limit further oxidation of the parent carbide material. This behavior was observed in numerous types of oxidation trials, including an arcjet test where the HfC material was exposed to surface temperatures as high as 2400°C. No volatilization of the oxide scale was observed in these tests. The prevalence of this stable, intermediate oxide layer under these test conditions indicates a potential avenue to confer prolonged high temperature oxidation protection at temperatures greater than 1700°C.

The focus of the research outlined in this dissertation was to identify the nature of the intermediate layer that forms upon oxidation of HfC, and in doing so, provide guidance as to the driving forces for its formation and its role in the oxidation process of hafnium carbide. A few key points will be addressed regarding the analysis of the oxidation products of HfC:

1. What thermodynamic or kinetic driving forces are responsible for the observed oxidation phenomena in HfC?
2. What is the effect of nano-/microstructure on the oxidation behavior of HfC?
3. How does temperature affect the mechanisms by which HfC oxidizes?

2. LITERATURE REVIEW

2.1. HAFNIUM CARBIDE

Hafnium carbide (HfC) is a refractory ceramic material that possesses the rocksalt prototypical cubic structure (Space Group #225, Fm-3m) shown in Figure 2.1. Hafnium carbide also exhibits a wide range of stoichiometry, varying from as low as $HfC_{0.5}$ to as high as $HfC_{1.0}$. Non-stoichiometry in hafnium carbide is due to the formation of carbon vacancies.[1] This wide range of carbon stoichiometry allows for the tailoring of material properties for various applications, as the hardness, coefficient of thermal expansion and elastic modulus all vary substantially as a function of carbon content.[2] It possesses a congruent melting point of 3942°C at a carbon content of $HfC_{0.94}$, making it one of the highest known melting point compounds.[3] This combination of material properties makes HfC an interesting candidate material for applications where extreme temperatures and mechanical loads will be experienced, such as in hypersonic applications.

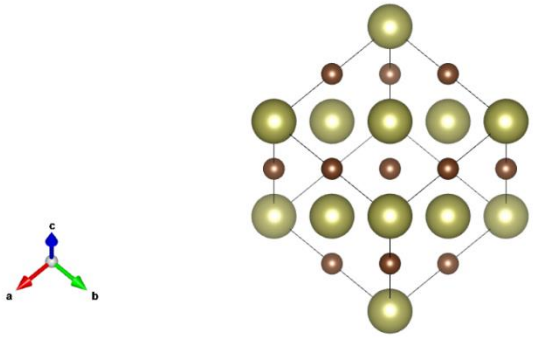

Figure 2.1 Crystal structure of HfC. Hafnium atoms are denoted by gold spheres, while C atoms are denoted by brown spheres.

In hypersonic applications, high temperatures and large mechanical loads are not the only external influences that need to be accounted for. High-temperature stability, chemical compatibility with the underlying substrate and oxidation resistance above 1800°C are all important characteristics of candidate materials in these applications.[4] Travelling through the atmosphere at Mach 5 or greater means that, in addition to large mechanical stresses and heat fluxes, there are serious corrosion issues due to the presence of oxidizing gas species that need to be understood and accounted for.[5] Currently, most hypersonic systems use composites that implement either C/C, SiC/SiC, or C/SiC (fiber/matrix) materials for protection from high temperatures.[6] While desirable due to their high strength/weight ratio, all of these composite systems have drawbacks. C/C systems do not confer prolonged oxidation protection, meaning serious recession of the system can occur during extended exposure to test conditions. SiC/SiC and C/SiC systems are both limited in their maximum use temperatures as a result of the decreased stiffness of SiC at elevated temperatures, as well as the passive-to-active transition during the oxidation of SiC.[7,8] During this passive-to-active transition, the initially protective SiO_2 scale that forms on the surface of the material decomposes via reaction with the underlying SiC to form $SiO_{(g)}$ which volatilizes and removes the protective scale that has formed. This phenomenon can be described thermodynamically by considering the temperatures and partial pressures of oxygen at which the partial pressure of $SiO_{(g)}$ exceeds the equilibrium value. This transition occurs at approximately 1500°C at a total pressure of 1 bar, $pO_2 = 1x10^{-4}$ bar. Thus, it is important to find an alternative that can withstand temperatures greater than this.[8]

In addition to high temperature stability considerations, substrate compatibility is extremely important. CTE mismatch at the interface of the material results in the generation

of thermal stresses that can lead to crack formation, leading to further oxidative degradation. Since carbide-based materials are natural materials choices for coatings on C-based components due to their ability to form strong, adherent interfaces with the C substrate, the ability to vary the CTE through carbon stoichiometry is very appealing for these applications. Group IV transition metal carbides are an attractive candidate class of materials for hypersonic applications, as they possess high-temperature stability and chemical compatibility.

Carbides of the Group IV transition metals have seen a great deal of investigation due to the formation of native oxides whose melting points exceed 2000°C. For example, HfC oxidizes to form HfO_2, an oxide that possesses a melting point of ~2810°C.[9] Pure HfO_2 exhibits three primary polymorphs as a function of temperature at ambient pressures. At room temperature, HfO_2 is monoclinic (space group #14: $P2_1/c$). At 1715°C, monoclinic HfO_2 transforms to a tetragonal phase (space group #137: P42/nmc), and at 2244°C, HfO_2 exhibits a tetragonal-to- cubic transformation (space group #225: Fm-3m). This is shown in Figure 2.2. The transformation from monoclinic to tetragonal is diffusionless/displacive, meaning that it can occur rapidly without breaking or reforming bonds, and is associated with a large volume expansion (calculated to be ~4%) on cooling.[10,11] This can lead to damage in the oxide scale during cooling, as large stresses can generate cracks that propagate through the oxide scale, which can hinder the protection conferred by the oxide scale.

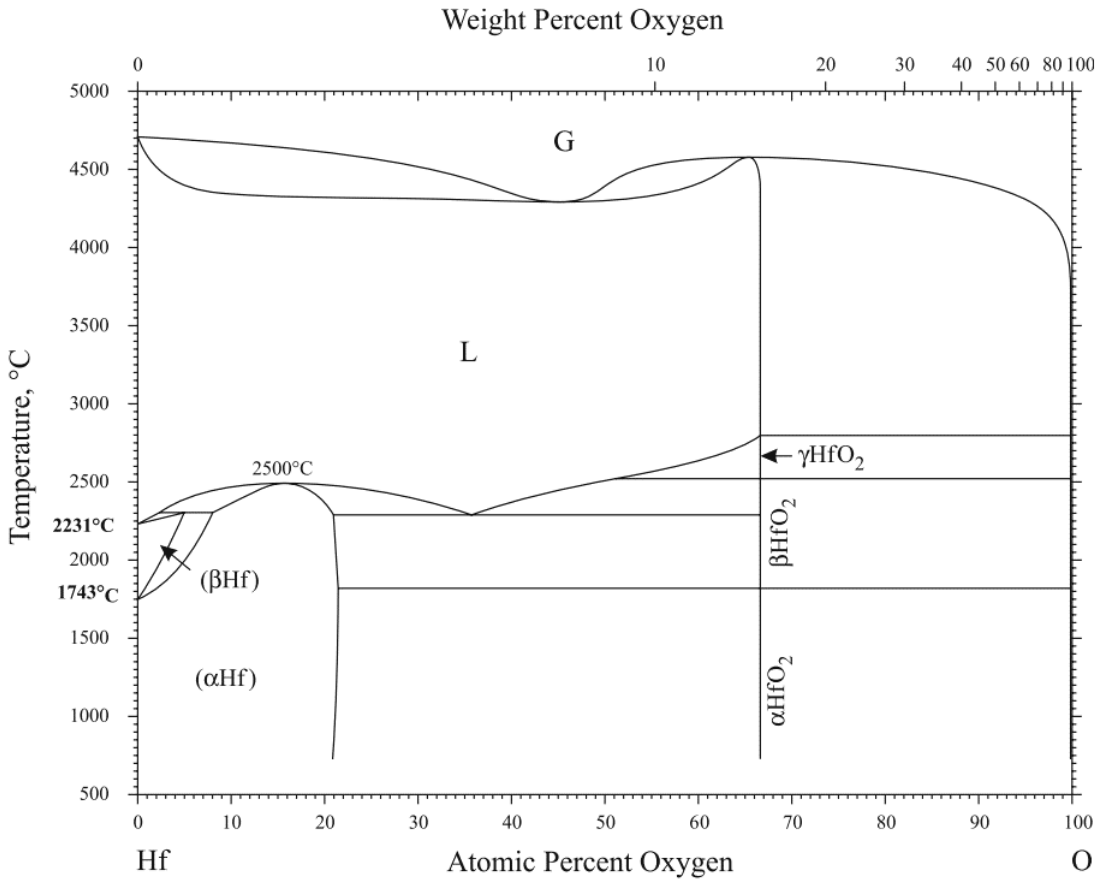

Figure 2.2: Phase diagram of the Hf-O system, showing the presence of three ambient-pressure polymorphs of HfO_2. Monoclinic HfO_2 is the lowest temperature polymorph, changing to tetragonal HfO_2, followed by cubic HfO_2 at the highest temperatures.[7]

2.2. OXIDATION OF HAFNIUM CARBIDE

Hafnium carbide experiences the observable formation of an oxide scale at temperatures as low as 500°C, irrespective of the partial pressure of oxygen used in the trial.[12] Berkowitz-Mattuck in [13] studied the oxidation of HfC formed from the carbothermal reduction of HfO_2. Their results indicated that at temperatures ranging from 1517 - 1727°C oxidation rate kinetics were linear and occurred preferentially around the grain boundaries of the material. The presence of iron impurities in the starting material is

thought to impart less oxidation resistance to the carbide material, obfuscating the real oxidation behavior. Compositional descriptions of the oxide scale only claimed the presence of HfO_2 and Fe-containing impurities.[13] In certain oxidation studies, the presence of an multi-layer oxide scale with distinct morphology is formed.[12,14-18] The morphology and thickness of this interlayer varies as a function of temperature; however, it is generally described as dense, featureless and well-adherent to the underlying parent carbide material. Voitovich-Pugach in [19] studied the oxidation of HfC at temperatures ranging from 500-1200°C and observed the presence of multi-phased oxide scale comprising both monoclinic and tetragonal HfO_2, as well as C. They claim that the presence of C in the oxide scale stabilizes the tetragonal HfO_2 phase, although that has been explored through computational modelling more recently in [20], showing that that is likely not the main stabilizing mechanism for the presence of t-HfO_2. Shimada et al. studied HfC oxidation using single crystals of HfC cut parallel to either the (200) or (220) plane and thermogravimetric analysis (TGA) at temperatures of 500-1500°C and oxygen partial pressures of 0.02-80 kPa. During TGA analysis, degrees of oxidation exceeded 100% compared to the theoretical oxidation mass gain of $HfC + O_2 \rightarrow HfO_2 + CO_2$, indicating that the samples formed carbon in addition to hafnia. Shimada et al. used WDS to observe the composition of the interlayer and found that it contained carbon. The thickness of this interlayer was temperature dependent and gradually increased to a maximum thickness of 13 μm at 1300°C, followed by a decrease in thickness at 1500°C. X-ray diffraction results of the oxidized single-crystal surfaces indicated a preferred orientation of $(200)_{m\text{-}HfO2}//\{200\}_{HfC}$ below 900°C, and $(002)/(020)_{m\text{-}HfO2}//\{200\}_{HfC}$ above 900°C.

Bargeron et al. in [15,16] also studied the oxidation of HfC at temperatures up to 2100°C for varying times, although their tests were performed on HfC films formed via CVD which possessed a carbon stoichiometry of $HfC_{0.5}$, as determined by lattice parameter measurements via x-ray diffraction (XRD). Their results indicated the formation of a very thick (>75 μm) interlayer that was featureless and adherent to the underlying parent HfC film (see Figure 2.3). Chemical analysis of the interlayer indicated the presence of Hf, C and O. Using a moving boundary diffusion model, the relative motion of the interfaces was assessed by incorporating experimental observations of the thicknesses of each layer of the oxide scale to fit parabolic rate constants to scale thicknesses, allowing them to determine effective oxygen diffusion coefficients at temperatures of 1400 and 2060°C. Their results showed that at both temperatures of interest, the oxygen diffusion coefficient of the interlayer was an order of magnitude lower than for the outer oxide scale, indicating a protective nature of the interlayer. In addition, Knoop indentations taken at 100 gf and 200 gf of the interlayer material indicated a hardness matching the parent carbide material. The results of Bargeron et al. indicate that the main mass transport mechanism responsible for the protective nature is solid-state diffusion through the bulk of the interlayer material.

Wuchina et al. in [14] studied the oxidation of HfC in both static furnace atmospheres (T = 1500°C, P_{tot} = 1 atm, 10-60 min) as well as at low pressure in an arcjet (T = 2000-2400°C , P_{tot} = 0.58 atm, pO_2 = 10 kPa, 3 minutes) and at high pressure in a rocket motor chamber (T = 2000°C; P_{tot} = 34 and102 atm; 5, 10 and 20 seconds). In this study, an interlayer was reported at all test temperatures, although the nature of the interlayer varied between test methods.

The interlayer formed on samples tested in a furnace was found via Fourier Transfer Infrared Spectroscopy (FTIR) to contain both amorphous carbon and graphitic carbon.

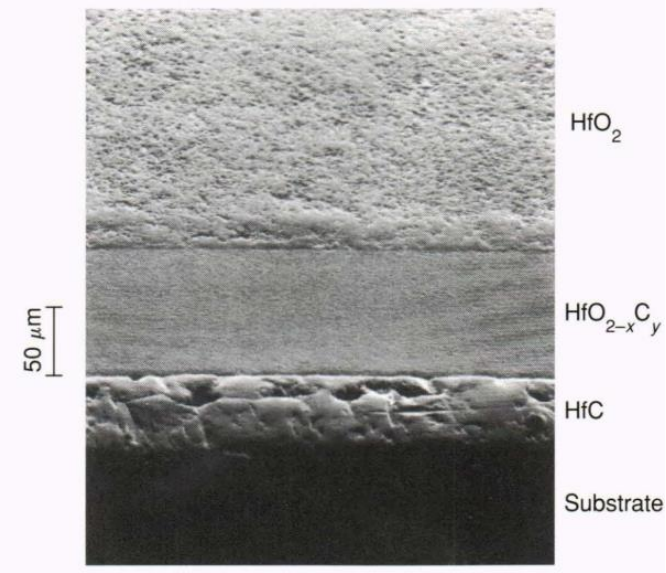

Figure 2.3: Cross-sectional scanning electron microscope image showing the oxide scale formed upon oxidation of chemical vapor deposited HfC films at 1865°C for 600 s in 7% O_2 balanced with Ar.[14]

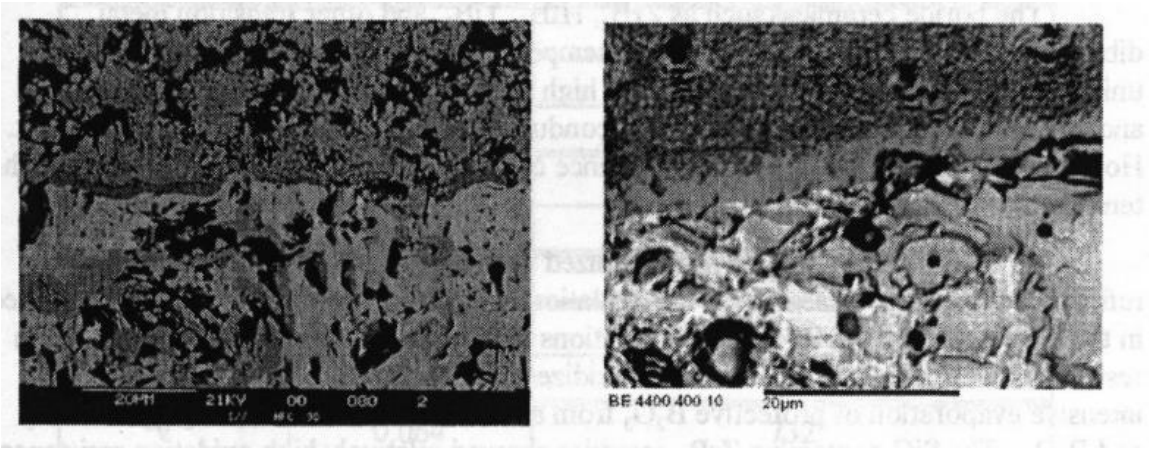

Figure 4: Oxide scales formed upon oxidation of HfC under arcjet and rocket motor test conditions. A thin, featureless band of material can be observed at the interface between the scale and the substrate in both methods.[12]

Arcjet testing of these materials also showed the presence of an interlayer with Hf, O and C. Rocket motor testing resulted in the formation of an adherent oxide scale, with an interlayer comprising Hf, O and C, thought to be similar in nature to the "hafnium oxycarbide" reported by Bargeron et al. Oxide scales of both tests are shown below in Figure 4.

Holcomb and Courtright researched the oxidation of hafnium carbide from 1200-2200°C using TGA below 1600°C and laser heating above 1800°C and found that the parabolic rate constant slowly decreased until ~1800°C, where it rapidly increased with increasing temperature, as shown in Figure 2.5.[17] Above 1800°C, a dense, narrow layer was observed that was relatively featureless, other than remnant pores from the bulk material, shown in Figure 2.6. No other report was given on the composition of this band of material. In all trials, the oxide scale tended to crack and spall; this was qualitatively determined to be due to cooling stresses and the associated tetragonal-to-monoclinic transformation.

The outer oxide scale that forms during the initial stage of the oxidation process has also been studied by authors. In most cases, where the temperature experienced on the top surface of the oxide scale is < 1700°C, the porosity in the oxide scale appears to reflect the relative rate of oxidation during the earlier stages of the oxidation process.[18] In other words, earlier in the oxidation process when the exposed surface area is large, the oxidation rate is faster and more gas is generated by the oxidation of C to form CO/CO_2. Since the Hf is being oxidized simultaneously with C, the porosity in the scale reflects the amount of CO/CO_2 being generated and moving away from the oxidation front. This was first described by Metcalfe in [21].

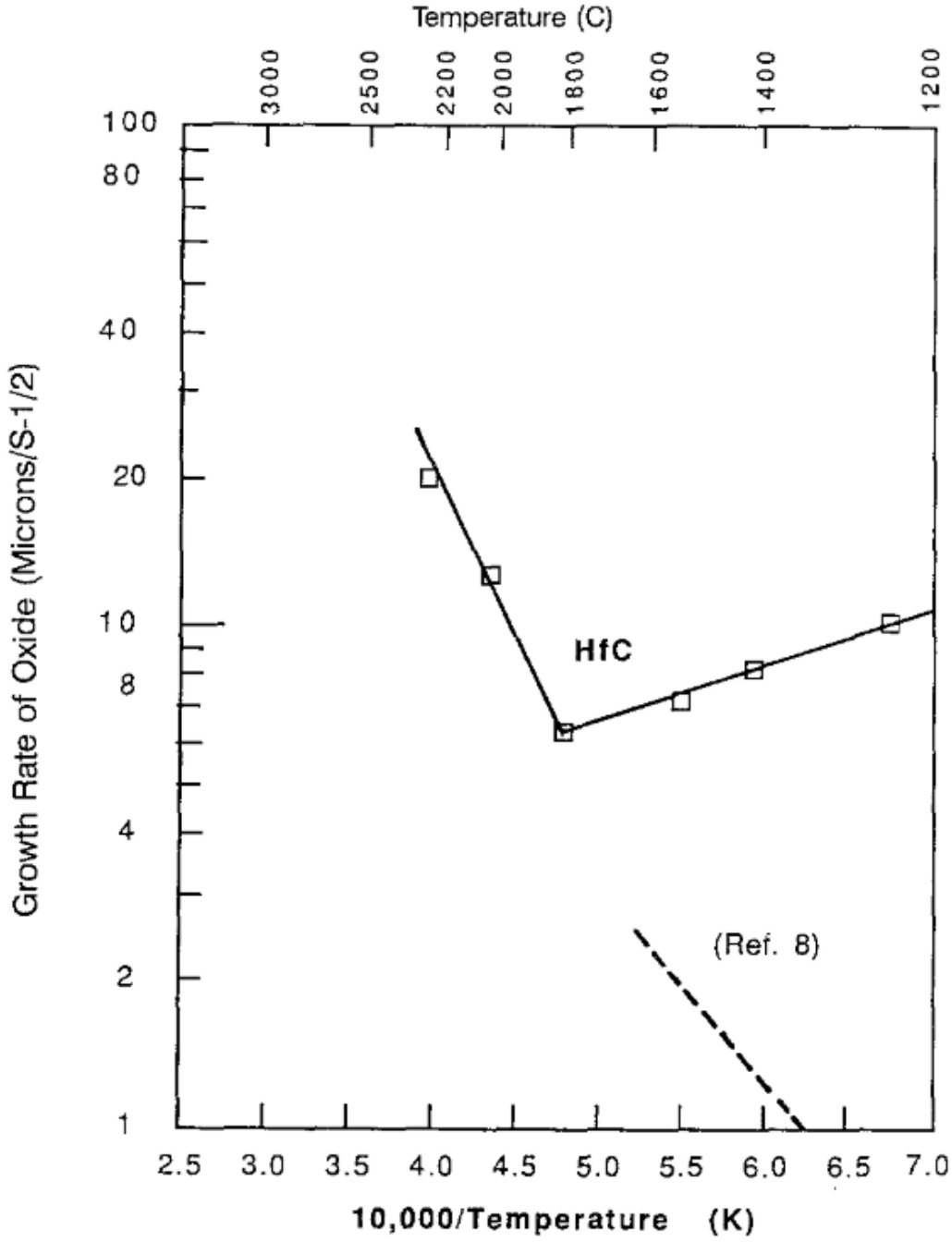

Figure 2.5: Experimental growth rates of HfO_2 on HfC from oxidation experiments. A discontinuity is shown around 1800°C, above which the oxide growth rate rapidly increases.[15]

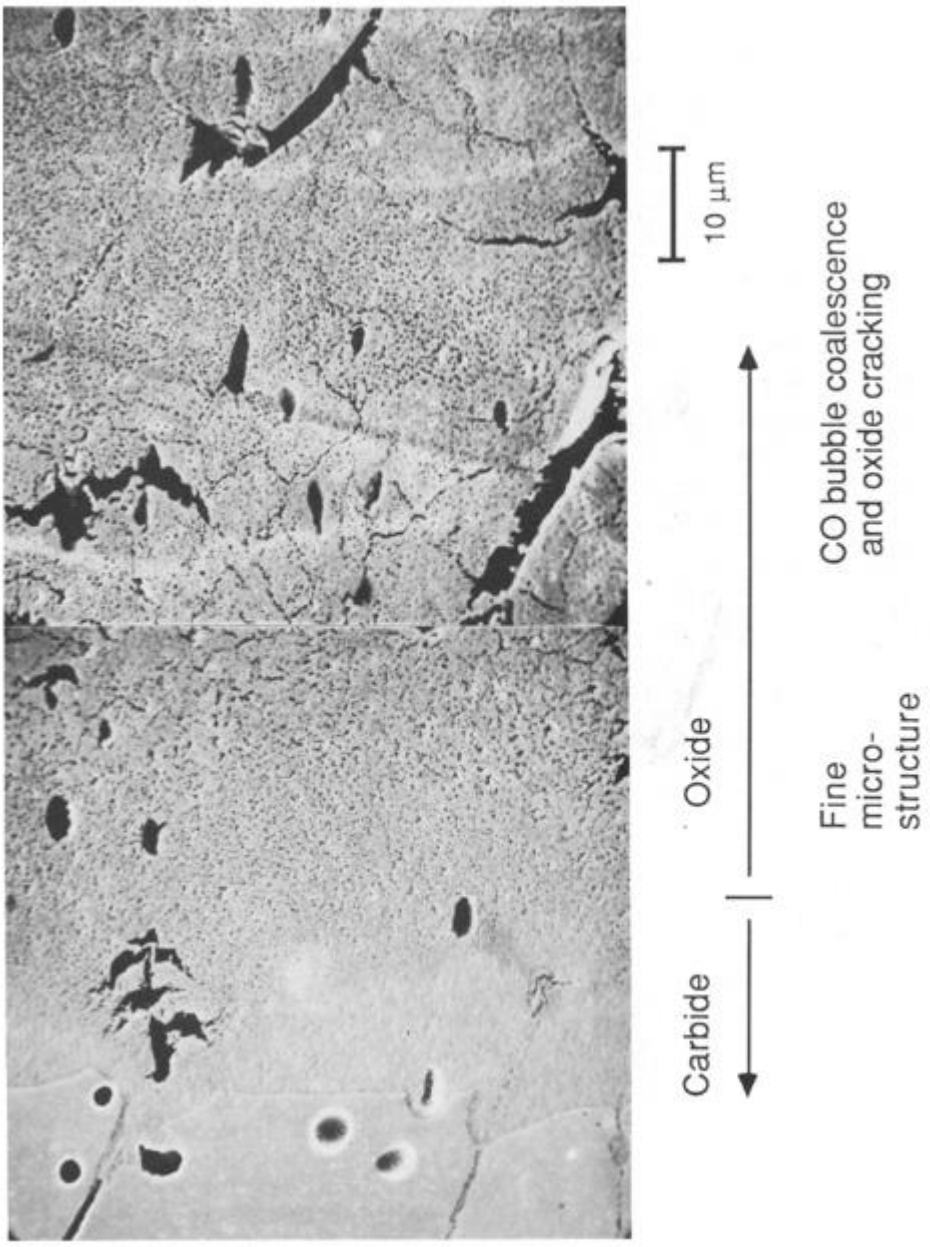

Figure 2.6: Cross-section of HfC oxidized at 2000°C for 5 minutes. A dense region is located very near the interface of the carbide and the oxide. The outer oxide scale is tremendously porous and possesses numerous cracks.

Holcomb and Courtright in [17,18] used a counter-current diffusion model to determine gas compositions through the oxide scale, calculate diffusion coefficients of gaseous species in the oxide scale, and in turn, determine parabolic rate constants as a function of experimentally determined percent porosity and pore size at various temperatures.[18] Their findings indicated that gas-phase diffusion was likely rate-controlling at these temperatures.

The addition of secondary elements to HfC to aid in enhancing oxidation performance has also been investigated. Since the outer oxide scale possesses large amounts of coarse, interconnected porosity, the permeability of oxygen through the oxide scale is relatively large.[17] Marnoch investigated the oxidation of Hf metal alloys and found that the addition of 20-30 wt% Ta led to the formation of dense oxide scales with lowered oxide growth at 2200°C.[11] Thus, Holcomb and Courtright investigated the oxidation of HfC alloyed with 25 wt% TaC to see if the addition of Ta to the carbide resulted in improved oxidation performance. Results of oxidation at temperatures greater than 1800°C were the formation of a damaged oxide scale that was highly irregular and tended to crack, with a composition of HfO_2 and $Ta_2Hf_6O_{19}$. Compared to HfC oxidized under the same conditions, the cracks were more severe and tended to extend through the entire scale. Due to these flaws in the oxide scale, the measured growth rate of the oxide scale tended to be larger for the TaC-doped HfC samples.[17] The addition of PrC_2 was also explored in an attempt to stabilize the formation of Hf-containing pyrochlores, thought to possess lower mobilities for anions through the lattice. Oxidation of the PrC_2-doped HfC materials resulted in runaway oxidation, due to internal oxidation of Pr and volatilization of the Pr metal. Oxidation kinetic trials of bulk HfC in this study indicated that the recession rate of the oxide scale

into the parent carbide decreased until roughly 1800°C, above which the recession rate rapidly increased. This was thought to be due to the change in reaction mechanism to solid-state diffusion control, as oxidation at and above 1800°C was similar in rate to the growth rates for metallic hafnium.

Reduction of porosity in the oxide scale was investigated through the oxidation of substoichiometric HfC_x by Wuchina et al.[14] Generally, samples with lower carbon contents possessed thinner oxide scales and resulted in the generation of less gaseous species, assisting in retaining scale integrity. In these tests, the presence of an intermediate layer was also observed. During static air furnace tests, the interlayer was identified with a composition of amorphous/graphitic carbon, while interlayers formed during high temperature arcjet and flame tests were identified as HfC_xO_y. Differences in oxidation mechanisms were observed at temperatures less than 1500°C, with grain boundary diffusion being ascribed to the lower temperature behavior and bulk diffusion for higher temperature oxidation. A microstructurally supported, mechanistic description of oxidation of HfC that describes differences in observed oxidation kinetics is currently lacking in the literature.

2.3. THERMODYNAMIC STABILITY OF THE INTERLAYER FORMED UPON OXIDATION OF HfC

The thermodynamic equilibrium between monoclinic HfO_2, graphitic carbon and HfC can be evaluated using phase stability diagrams, where a system of reactions governing the system is established, and the relationship between oxygen partial pressure, phase stability

and temperature is calculated. For the Hf-O-C system, the primary reactions can be written as follows:

$$HfC + O_2 \rightarrow HfO_2 + C \quad (6)$$

$$C + O_2 \rightarrow CO_2 \quad (7)$$

$$HfC + 2O_2 \rightarrow HfO_2 + CO_2 \quad (6+7)$$

By writing out thermodynamic equilibrium constants, the dependence of the reaction equilibrium on the partial pressure of oxygen can be established, assuming gas phase ideality. These are shown below:

$$K_1 = \frac{pCO2}{pO2^2} \quad (8)$$

$$K_2 = \frac{1}{pO2} \quad (9)$$

$$K_3 = \frac{pCO2}{pO2} \quad (10)$$

Equilibrium values of K (K_1, K_2, K_3) are evaluated by using tabulated data for the standard state free energies of formation of each phase in the reactions listed above, and then determining their values at nonstandard state using the equation below:

$$\Delta G = \Delta G^0 + RTln(Q) \quad (11)$$

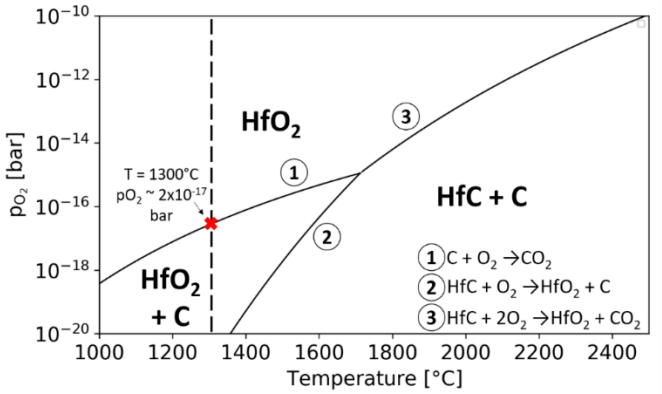

Figure 2.7: Phase stability diagram of the Hf-O-C system, showing the regions of stability of the solid, condensed phases. Total pressure of 1 bar was assumed, alongside graphite as the standard reference state for carbon, and monoclinic hafnia was assumed to be the standard phase for HfO_2. A triple point exists around ~1712°C, indicating that tests above this temperature should not exhibit interlayer formation.[23]

2.4. CONDITIONS AFFECTING THE "HfO_2 + C" STABILITY REGIME

Various conditions can affect the stability of the phase fields shown on the diagram. For example, the phase stability diagram shown in Figure 2.7 assumes a total pressure of 1 bar. Qualitatively, increasing the total pressure of the system should suppress the decomposition of the C in the system, extending the region of phase stability. Conversely, decreasing the total pressure of the system should increase the decomposition. This is shown in Figure 2.8. For high pressure reaction processes, the phase stability of the HfO_2 + C phase field is able to extend to higher temperatures, whereas for lower pressure processes (i.e. arcjet), the HfO_2 + C phase field is expected to shift to lower temperatures.

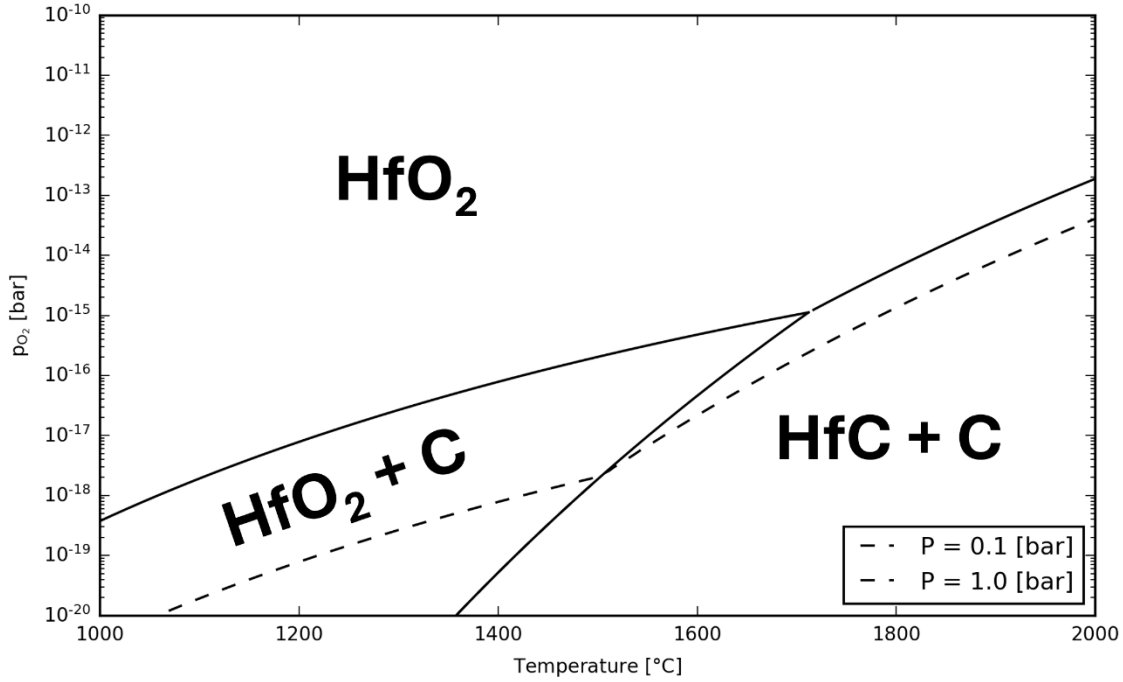

Figure 2.8: Phase stability diagram showing the effect of changing total pressure.

2.5. CHARACTERIZATION

Observations of the oxidation products of hafnium carbide have been carried out in the past using numerous characterization techniques. Spectroscopic techniques including FTIR and Raman have been used in the past in conjunction with elemental analyses such as energy-dispersive x-ray spectroscopy (EDS) and WDS.[12,14-18] Scanning electron microscopy (SEM) and transmission electron microscopy (TEM) have also been used to observe the morphology of the intermediate layer, with x-ray diffraction being used to characterize the structure of the phases. Synthesizing the results of all of these techniques led to the conclusion that the intermediate layer was composed primarily of monoclinic HfO_2 and graphitic carbon that persisted to temperatures well above thermodynamic predictions.

Raman spectroscopy is a spectroscopy technique involving the use of lasers to measure vibrational energy modes of samples. In this technique, a laser is shone onto the sample and the scattered light is collected using a detector. If photons of light are scattered inelastically (i.e., with a change in energy), then the scattering event is considered to be a Raman scattering event. Collecting traces of these Raman scattering events across wavenumbers leads to the formation of a Raman spectrum, whose peaks are characteristic of the vibrational modes of the structure and are directly related to the crystallographic point group of the crystal.[23]

Graphite is extremely sensitive to Raman spectroscopy and has been extensively studied in past literature.[24-26] Graphite shows primary peaks at ~1350 cm^{-1} (D band), 1580 cm^{-1} (G band), 1610 cm^{-1} (D* band), and 2660 cm^{-1} (2D band). The D and G bands are typically used to assess the crystallinity of the graphite in the sample, the defectiveness of the graphite, and they can also be used to determine the size of graphite crystallites in the sample through the use of I_D/I_G ratios, where I_D is the intensity of the D peak and I_D is the intensity of the G band.[27] The defectiveness of graphite is assessed by using I_D/I_G ratios as well. Since the D band is only present when the graphite in the sample is defected, the I_D/I_G ratio is a qualitative assessment of the amount of disorder in the graphite crystal structure. That is, larger ratios of I_D/I_G correspond to shorter correlation lengths of graphite crystallites and clusters in the system.

X-ray diffraction is a characterization technique that utilizes x-rays (typically Cu $K_{\alpha 1}$ λ = 1.54 Å) to probe the crystal structure of a material. X-rays interact with matter by absorption, scattering, reflection, transmission and diffraction. Diffraction is a special case of x-ray scattering where the scattered x-rays possess the same energy and phase as the

incident x-rays and are scattered at the same angle as the incident rays impinged upon the sample. Thus, diffraction is defined as the elastic (no energy change) and coherent (no phase change) scattering of x-rays by a material.[28] Bragg's Law describes the geometrical relation of the incident and scattered x-rays in diffraction, and is written mathematically in Equation 1 as:

$$n\lambda = 2dsin\theta \quad (1)$$

where n is the order of diffraction (assumed to be 1), λ is the wavelength of the x-rays used, d is the d-spacing of the diffracting plane in the crystal structure, and θ is the angle of the incident and diffracted beams. Crystalline materials (both single-crystal and polycrystalline) are identified through x-ray diffraction patterns by typically sharp peaks at angles characteristic of the d-spacing of the material, whereas amorphous materials are indicated by broad regions of increased intensity. Similar principles apply to other types of diffraction, such as electron diffraction, where a beam of electrons is used to probe the structure, or neutron diffraction, where neutrons are used to probe the structure.

Other useful information can be gleaned from the shapes of the peaks in a diffraction pattern for a crystalline material, such as the size of crystallites in the material, or the strain in a material. As crystallites of a strain-free material become smaller and smaller, the full-width at half maximum of a diffraction peak in the pattern will increase according to the Scherrer equation below:

$$\tau = \frac{K\lambda}{\beta cos\theta} \quad (2)$$

where τ is the crystallite size, K is a shape factor of the crystallite (typically around 1), β is the difference in FWHM between the measured peak and the instrumental broadening measured from a standard, and θ is the diffraction angle of the peak. Uniform strain of a material can cause shifts in relative peak positions compared to powder diffraction files (PDFs), while nonuniform strain can lead to peak broadening.[28]

The ambient pressure polymorphs of HfO_2 can be difficult to distinguish via diffraction techniques. Qualitatively, this can be described on the basis of crystal classes and displacive transformations. The polymorphic transition sequence of monoclinic to tetragonal can be viewed as a shifting of the a-c axes to change the β angle of the unit cell, and the tetragonal to cubic unit cell can be viewed as a simple length along the non-uniform axis (original monoclinic b-axis). The (020) plane for m-HfO_2 has a d-spacing of 2.524 Å (PDF #34-0104) while the (002) plane for c-HfO_2 has a d-spacing of 2.547 Å (PDF #53-0560), and the (110) plane for t-HfO_2 has a d-spacing of 2.579 Å (PDF #1-087-3320). Small amounts of either uniform or non-uniform strain within the lattice can shift these values substantially enough to make delineation between peaks in diffraction extremely difficult within the resolution of standard x-ray diffractometers/electron diffraction patterns.

To complicate issues further, HfO_2 also exhibits varying polymorphic stability based on the crystallite size. For unconstrained crystals of HfO_2 at room temperature and ambient pressure, by using enthalpies of formation of the polymorphs of oxides in combination with their respective surface energies, regions of phase stability were assessed for the hafnium oxides. These calculations indicated that amorphous hafnia is stable at the lowest crystallite sizes. This stability changes between 3.75 and 21 nm, c-HfO_2 is the most stable polymorph,

whereas between 21 and 38 nm t-HfO_2 is the most stable polymorph. Above 38 nm, m-HfO_2 is the most stable phase.[29] This, in conjunction with strain effects, as well as the presence of interfaces between phases can complicate the analysis of the polymorphs of HfO_2 that are present.

Detection of carbon via x-ray diffraction can be especially difficult when in a two-phase mixture, as the higher-mass elements tend to absorb and scatter x-rays more efficiently than the lower-mass elements. This can be described by mass attenuation coefficients using the following equation[28]:

$$\frac{\mu}{\rho} = w_1(\frac{\mu}{\rho})_1 + w_2(\frac{\mu}{\rho})_2 + \cdots \quad (3)$$

Where $\frac{\mu}{\rho}$ is defined as the mass attenuation coefficient for the given material, w_1 is defined as the weight fraction of component 1, $(\frac{\mu}{\rho})_1$ is the mass attenuation coefficient of component 1, and so on. Through this equation, it can be seen that for a mixture of equimolar amounts of HfO_2 + C, the calculated mass attenuation coefficient (combined effect of scattering and absorption) is 0.039944 cm^2/g, ~95% of which is contributed by the HfO_2 in the mixture, meaning that most of the scattered x-rays will be from the HfO_2, leading to inefficient data collection for the carbon in the mixture. Clearly, characterization of HfO_2 and C requires multiple careful methods of analysis for proper determination of the phase assemblage, morphology and structure of the intermediate layer.

2.6. IMPACT OF FURNACE DESIGN ON EXPERIMENTATION

Heating of samples for scientific testing is traditionally carried out in furnaces. Specific types of furnaces can have marked impacts on the ability to perform certain experiments. Certain types of furnaces are limited by the ability to ramp to temperatures at slow rates, whereas some furnaces are incapable of providing the necessary atmospheres for tests. For example, tests aiming to investigate the effect of thermodynamic activities of carbon less than 1 in a system should not use graphite furnaces, since the final equilibrium of the system will include bulk graphite from both the furnace elements and the furnace chamber, pinning the activity at 1 in the case of assumed gas-solid interfacial equilibrium. In cases like this, furnaces avoiding the presence of carbon are beneficial; however, the presence of heating elements leads to the inability to heat the sample directly, reducing the maximum test capabilities. In addition, the effect of the chemical makeup of the furnace also plays a major, albeit more practical, role in experimental design. A tungsten heating element furnace, for example, may be able to achieve the temperatures necessary for testing (>2000°C); however, the presence of carbon in materials being tested can lead to carburization and embrittlement of the furnace elements and body. In these situations, directed power systems, such as those using photon sources are important as they enable testing at high temperatures and can be designed to operate in an environment that is atmosphere controlled.

Directed power systems have been used extensively in the exploration of advanced materials testing and processing.[30,31] Typically, these systems implement monochromatic, high-intensity light/lasers focused to very fine spots. This enables extremely high heat fluxes localized in a small region on the sample, which can be precisely adjusted for

advanced testing. Benefits of this test method are the extremely high heat fluxes, and the ease of temperature measurements through pyrometry, since only one narrow bandwidth needs to be excluded from the measured sample emission spectrum.

Other forms of directed power systems are solar simulators, as well as quadrupole light furnaces and solar furnaces.[32-35] In solar simulators and quadrupole light furnaces, high-power lamps, typically Xe arc short arc lamps or halogen lamps, are housed in mirrors that focus light onto the sample. The reflectors are chosen to be a specific geometry, usually parabolic or ellipsoidal, depending on the required type of light focus. Since the emissions spectrum from a Xe lamp is similar to the spectrum of sunlight, these lamps are capable of emulating exposure conditions that photovoltaic solar cells may experience.[36] In test systems where the generated light is focused to a small spot to enable high heat fluxes, the spectrum of light coming off the sample is complicated. For opaque test samples (i.e., no transmission of any wavelengths of light being generated by the lamp), using light focused from a lamp confounds the traditional radiation curve with light that is reflected off of the sample surface. This effectively "poisons" the spectrum, meaning that advanced instrumentation methods and design are required to accurately measure the temperature of the surface of the sample. One way that this can be performed is through the use of high-speed shutters and a spectral pyrometer.

Pyrometry is the determination of sample temperature through the measurement of light radiated from a sample. Every real material emits thermal radiation at any temperature above absolute zero. Materials that perfectly absorb and emit thermal radiation are called "blackbodies".[37] The location of the peak maxima for "blackbodies" can be described by the Planck equation below:

$$\rho_T(\nu)d\nu = \frac{8\pi\nu^2}{c^3}\frac{h\nu}{\exp\left(\frac{h\nu}{kT}\right)-1}d\nu \quad (4)$$

Where $\rho_T(\nu)$ is the spectral radiant energy density, ν is the frequency, c is the speed of light in a vacuum, h is Planck's constant, and k is Boltzmann's constant. Most real materials emit thermal radiation at some fraction of the overall spectral radiance. This fraction is defined as the spectral emissivity of a material. The emissivity of a material is unique in that it is material dependent but tends to vary based on the range of wavelengths, as well as viewing angle (directional emissivity corresponds to emittance at one viewing angle, whereas hemispherical emissivity corresponds to the total emittance). Certain materials may emit radiation perfectly at a given temperature in a specific wavelength range, while emitting more like a "graybody" under another wavelength range at the same temperature. In addition, the emittance of a material is dependent upon the surface roughness of a material, as the absorption of light for materials will increase with increasing roughness as a result of enhanced internal reflection inside the surface flaws. Knowledge of the physics behind radiation enables the usage of pyrometers for non-contact temperature measurement.

Pyrometry is the determination of sample temperature by measurement of thermal radiation. Numerous types of pyrometers exist, such as disappearing filament pyrometers, where the brightness of a tungsten filament is changed by adjusting the current in order to match the brightness of the object being observed, and two color pyrometers, where two wavelengths of light are observed, and temperature is calculated by assuming the emissivity at these two wavelengths is the same (greybody assumption).

$$T = \frac{\frac{1}{\lambda_1} - \frac{1}{\lambda_2}}{\frac{1}{\lambda_1 T_{NBB}(\lambda_1)} - \frac{1}{\lambda_2 T_{NBB}(\lambda_2)}} \quad (5)$$

Two color pyrometers have the benefit of eliminating the need to know the material's emissivity; however, this is only practical if the material meets the graybody assumption.

Going a step further, spectral pyrometers perform the calculation above at narrow bandwidths hundreds of times through the use of computational algorithms. By doing this, changes in emissivity can be effectively ignored, allowing for more accurate determinations of sample temperatures without knowing the spectral response of the material at various wavelength ranges.[38]

PAPER

I. THE ROLE OF MICROSTRUCTURE ON HIGH TEMPERATURE OXIDATION BEHAVIOR OF HAFNIUM CARBIDE

Published in the *Journal of the American Ceramic Society* Dec. 2022

Jonathan A. Scott[a], Xiaoqing He[b], David W. Lipke[a]

a) Department of Materials Science & Engineering, Missouri University of Science and Technology, Rolla, MO 65409, USA

b) Electron Microscopy Core and Department of Mechanical & Aerospace Engineering, University of Missouri, Columbia, MO 65211, USA

ABSTRACT

Microstructure development of the products formed upon oxidation of hafnium carbide (HfC_x, x = 0.67, 0.84, or 0.94) at 1300°C and 0.8 mbar oxygen pressure was investigated using Raman spectroscopy, x-ray diffraction, electron microscopy and electron energy loss spectroscopy. For all specimens a multi-layer oxide scale was observed featuring an outermost porous hafnia layer and an interlayer adjacent to the parent carbide containing hafnia interspersed with carbon. The outermost hafnia features coarse pores presumably formed during initial stages of oxidation to allow rapidly evolving gaseous products to escape from the oxidation front. As the oxidation scale thickens, diffusional resistance results in slower oxidation rates and smaller quantities of gaseous products that are removed via networks of increasingly fine pores until the local oxygen partial pressure is sufficiently low to selectively oxidize the parent carbide. Electron microscopy studies suggest that the oxidation sequence at this stage begins with the

transformation of parent carbide to an amorphous material having empirical formula HfO_2C_x that subsequently phase separates into hafnia and carbon domains. Hafnia polymorphs in the phase separated region vary from cubic to monoclinic as grains coarsen from ca. 2-20 nm, respectively. Immediately adjacent to the phase separated region is carbon-free mesoporous hafnia whose pore morphology is inherited from that of prior carbon domains. The average pore size and pore volume fraction observed in mesoporous hafnia are consistent with predictions from kinetic models that ascribe gaseous diffusion through a pore network as the rate determining step in oxidation behavior of hafnium carbide. These observations imply that high temperature oxidation behavior of hafnium carbide under the employed test conditions is linked to microstructure development via phase separation and coarsening behaviors of an initially formed amorphous HfO_2C_x product.

1. INTRODUCTION

Ultra-high temperature ceramics (UHTCs) are a class of materials principally comprising Group IV-V transition metal borides, carbides, and nitrides that, on account of their ultra-high melting points (> 3000°C), are candidate materials for service in extreme environment applications such as leading edges of hypersonic vehicles.[1–4] Hafnium carbide (HfC_x) is among the most refractory UHTCs, possessing a melting temperature $T_M = 3950 \pm 40$°C for $x = 0.94 \pm 0.01$.[5] The primary oxidation product of HfC_x, hafnium oxide (HfO_2), melts at ca. 2800°C,[6] making HfC_x particularly attractive for use in high temperature oxidizing environments.

Pure, dense HfC_x forms multi-layered oxidation scales in test environments ranging from static furnaces to arc-jets corresponding to a variety of test temperatures and oxygen partial pressures.[7–10] Reportedly, the parent carbide is initially saturated with oxygen to form HfC_xO_y where y is < 0.10 at 1650°C, followed by the formation of a pore-free interlayer whose composition is variously given as $HfO_{2-x}C_y$ "where x is small compared to 2 and y is probably closer to 0 than 1,"[9,10] or, contrarily, where "y is closer to 1".[11] Several diffusion-based models have been put forward to rationalize experimental observations based on a transformation sequence starting from the oxygen-saturated parent carbide, to a carbon-containing interlayer, and finally to hafnia upon continued oxidation. These models make different assumptions concerning rate-limiting transport mechanisms responsible for the kinetics of scale formation. In the model put forward by Bargeron et al.,[10] a moving boundary formalism is used to interpret the parabolic kinetics of oxide layer growth. Bargeron et al. conclude that inward lattice diffusion of oxygen is likely rate-limiting based on the presence of microstructural features generally consistent with this mechanism as seen in high temperature oxidation of metals, namely planar interfaces normal to the growth direction and apparent chemical homogeneity of the interlayer at the analytical length scale discernable by electron microprobe. While the model provides reasonable parabolic rate constants and effective diffusion coefficients, it does not account for the effects of oxidation scale microstructure. Alternatively, Holcomb et al.[12] interpret the high temperature oxidation behavior of HfC_x using a mechanistic model that assumes the rate-limiting mechanism is capillary diffusion of gaseous species through a network of pores. The capillary diffusion model predicts parabolic oxidation constants for HfC_x across

a range of temperatures and oxygen partial pressures that are consistent with observations using a two-parameter fit for pore volume fraction (ca. 0.02) and pore radius (ca. 0.01 μm).

Despite the success of the model of Holcomb et al. to explain macroscopic oxidation behavior of HfC_x, the processes responsible for pore formation and oxide scale evolution in the vicinity of the carbide-oxide interface remain unclear. This work reports on oxidation studies of HfC_x (x = 0.67, 0.84, or 0.94) at 1300°C and 0.8 mbar oxygen pressure aimed at disambiguation of the mechanisms of microstructure development in oxidation scale formation in this technologically important UHTC material.

2. EXPERIMENTAL PROCEDURE

Hafnium carbide powder (>99.9%, -325 mesh; H.C. Starck, Newton, MA) with measured composition of $HfC_{0.94}$ was mixed with hafnium hydride powder (min. 95%, max. d_{50} = 6.0 μm, Albemarle, Langelsheim, Germany) via ball milling using ethanol and yttria-stabilized zirconia milling media to produce powder mixtures targeting three different compositions of HfC_x (x = 0.67, 0.84, and 0.94). These powder mixtures were subsequently dried using a rotary evaporator and passed through a 50-mesh sieve. Each powder mixture was then loaded into a 1” diameter circular graphite die lined with 0.005”-thick graphite foil (NeoGraf Solutions, Lakewood, OH). The powder compacts were subsequently densified to >95% relative density, either by hot pressing at 2200°C and 32 MPa for 2 hours or by spark-plasma sintering at 2200°C and 50 MPa for 5 minutes. Any flashing or graphite foil left from sintering was removed by surface grinding (FSG-618; Chevalier; Sante Fe Springs, CA). Density was measured via the Archimedes method

following a modified version of ASTM B962-17[13] where specimens were boiled for 2 hours, rather than 24 hours, in distilled water. The carbon content of the pressed specimens was measured using a carbon analyzer (CS600; LECO Corporation; St. Joseph, MI) on powders of crushed bulk specimens that had been passed through a 200-mesh sieve. Pressed discs were mounted in an acrylic resin (VariDur 20-3756; Buehler, Lake Bluff, IL), polished to a 0.25 µm finish, and analyzed using scanning electron microscopy (SEM) to determine an average grain size. For $HfC_{0.67}$ and $HfC_{0.84}$, a thermal etching treatment at 1800°C for 30 minutes was necessary to reveal grain boundaries. At least 300 grains observed from multiple random fields of view were analyzed with image analysis software (ImageJ; National Institutes of Health; Bethesda, MD) using an intercept method. For the intercept method, 20 lines per sample were used on 3 fields of view for each specimen.

Hot pressed specimens were cut into ca. 4x4x4 mm cubes and subsequently oxidized in an atmosphere-controlled tube furnace under flowing Ar at a rate of 100 mL/min until the furnace temperature reached 1300°C, at which point the furnace atmosphere was switched to a flowing Ar/O_2 gas blend with O_2 partial pressure of 0.8 mbar for an oxidation test duration of four hours. Oxygen concentrations were monitored using an oxygen analyzer with ppm sensitivity (AMETEK Thermox CG1000 Oxygen Analyzer; AMETEK; Pittsburgh, PA). Oxidized specimens were mounted, sectioned, and polished to a 0.25 µm finish and their oxide scales were investigated using optical microscopy, SEM, Raman spectroscopy (LabRAM Aramis; HORIBA Jobin Yvon; Kyoto, Japan) and x-ray diffraction (XRD) (X'Pert MRD; Malvern PANalytical ltd.; Malvern, United Kingdom). For one $HfC_{0.94}$ specimen, tape was used to mechanically separate the oxide scale from the underlying carbide material and was subsequently analyzed following the same

experimental procedure. Raman spectroscopy scans were collected from 500-3000 cm^{-1} using a HeNe laser (λ = 632.8 nm). Prior to analysis, spectrometer calibration was performed using a silicon standard. XRD scans were performed in a standard Bragg-Brentano geometry using Ni-filtered Cu-Kα radiation as well as in an azimuthal geometry to generate pole figures used to characterize crystallographic texturing in parent $HfC_{0.94}$ specimens and as-formed oxide scales.

A focused ion beam (FIB) (Scios DualBeam FIB SEM; FEI; Hillsboro, OR) was used to lift out specimens perpendicular to the interface between the HfC_x and oxide scale interlayer, which were subsequently analyzed using transmission electron microscopy (TEM) (Tecnai TF30 Twin; FEI; Hillsboro, OR) and scanning transmission electron microscopy (STEM). Electron energy-loss spectroscopy (EELS) was used to determine the elemental chemistry of selected regions in the vicinity of the interlayer.

Berkovich-tip nanoindentation measurements were carried out on polished cross-sections of oxidized $HfC_{0.94}$ specimens for the determination of both hardness and Young's modulus values for the oxide scale, interlayer, and the parent carbide material using an Agilent G200 nanoindenter (Keysight Technologies, Santa Rosa, CA). Indentations were created on each specimen using a 200 mN max load, applied in 10 cycles per indentation and holding for 10 seconds at the maximum load. Twenty indentations were made for the parent $HfC_{0.94}$ material and the outer HfO_2 layer, while nine indentations were made for the interlayer.

3. RESULTS AND DISCUSSION

3.1. ORIGINS AND ROLE OF THE HfC_x INTERLAYER

Table 1 lists the relative densities and average grain sizes of sintered HfC_x specimens. Significant grain growth in the $HfC_{0.65}$ and $HfC_{0.81}$ specimens was observed with maximum measured grain sizes of 180.7 μm and 58.0 μm, respectively. XRD analyses of the sintered HfC_x specimens indicated the presence of only HfC with no detectable second phases. Comparison of observed versus expected relative peak intensities showed no evidence of crystallographic texturing in parent carbide materials.

Table 1: Relative densities and average grain sizes of SPS-synthesized HfC_x specimens.

Composition	**Relative Density (%)**	**Average Grain Size (μm)**
$HfC_{0.65\pm0.01}$	97.4 ± 0.1	57 ± 2
$HfC_{0.81\pm0.02}$	95.8 ± 0.1	19 ± 1
$HfC_{0.94\pm0.01}$	94.7 ± 0.1	2 ± 1

Optical micrographs of oxidized HfC_x specimens are shown in Figure 1A-C. All specimens exhibited similar oxide scale morphologies, with a dark, black carbon-containing inner oxide layer and a light, white outer oxide scale featuring a multi-layered "Maltese cross" shape where the oxide scale is cracked and split at edges. This shape, thought to form due to tensile thermal-elastic mismatch stresses in the oxide scale concentrated at specimen corners and edges, became less pronounced for specimens with lower carbon content.[14] The oxide scales of each specimen are composed of multiple layers

identifiable by distinguishing characteristics. The innermost layer of the oxide scale (i.e., the 'interlayer') exhibits noticeable grain boundary oxidation and shows an increasing thickness with increasing carbon content for identical oxidation conditions: 5 ± 1μm for $HfC_{0.65}$, 11 ± 2 μm for $HfC_{0.81}$, and 20 ± 1 μm for $HfC_{0.94}$. Grain boundary oxidation is more pronounced for $HfC_{0.84}$ and $HfC_{0.94}$ specimens as compared to relatively coarse grained $HfC_{0.65}$. Oxidation scales formed upon $HfC_{0.65}$ also exhibit bands of material that run from the oxidized region through to the parent carbide. Energy-dispersive x-ray spectroscopy (EDS) scans of these bands revealed the presence of hafnium and oxygen (Supplemental Figure 1). Adjacent to the interlayer/oxide scale (IL/OS) boundary, a region of fine porosity (i.e., having pore radii as small as 12 nm) is observed. Pore size and total apparent porosity increase with distance away from the IL/OS boundary, which is consistent with previous reports.[10,15–17] Based on analysis of FIB liftouts, pore size was found to increase linearly up to ca. 3 μm away from the IL/OS boundary (Figure 2).

On all specimens the interlayer is found to contain carbon and hafnia as determined by Raman spectroscopy, the results of which are shown in Figure 3. D and G peak ratios produced I(D)/I(G) values of 1.24 ($HfC_{0.94}$), 1.77 ($HfC_{0.81}$) and 1.69 ($HfC_{0.65}$), indicating disordering and defectiveness of the graphitic carbon in each specimen.[18] The D peak is also downshifted from ~1350 cm^{-1} to ~1332 cm^{-1} in all specimens. This is due to the dispersive nature of the D peak with the wavelength of the laser used (λ_{HeNe} = 632.8 nm), which causes the excitation energy required for a Raman scattering event to be reduced, and correspondingly reduces the wavenumber at which the D peak occurs.[18,19] The shape of the 2D peak located at ~2661 cm^{-1} also indicates that the graphitic carbon is multiple layers thick, as it is beginning to approach the shape of the 2D peak for bulk graphite.[19]

Raman spectra of the outer oxide scale indicate only the presence of hafnia, as no D or G peaks associated with free carbon were identified.

Figure 4 shows XRD patterns of the top surfaces of the oxidized HfC_x specimens. Some mild texturing is observed in the peak intensities of the (200) and $(\bar{2}02)$ diffraction peaks. The pattern for $HfC_{0.94}$ contains diffraction peaks for monoclinic hafnia (m-HfO_2) with trace amounts of tetragonal hafnia (t-HfO_2). XRD scans performed on exposed interlayer product from the oxidation of $HfC_{0.94}$ indicate the presence of m-HfO_2 as well as t-HfO_2 and trace graphite. The 100% intensity peak for t-HfO_2 was not directly observed in these measurements, likely due to spectral resolution issues preventing deconvolution of the t-HfO_2 (101) and $CaCO_3$ (104) peaks (29.651° versus 29.406°, respectively), with the latter a constituent of the duct tape backing used to mechanically separate the oxide scale to expose the interlayer for analysis.[20] The amount of t-HfO_2 present could not be quantitatively determined via Rietveld refinement because of texturing effects within the pattern as well as the low intensity of the reflections associated with this phase.

The underlying carbide on oxidized $HfC_{0.94}$ shows no crystallographic texturing (Supplemental Figure 2). TEM observations of the oxide scale that forms immediately upon grains of $HfC_{0.94}$, shows a grain-by-grain orientation dependence. This indicates preferential growth directions of HfO_2; grains of HfO_2 whose preferred growth directions are closest to the normal of the oxidation front will "win out" and lead to the observed texturing in the oxide scale, e.g., if a grain of HfC has the [111] normal to the surface of the sample, then the (111) plane of HfO_2 will tend to grow preferentially.[21]

TEM micrographs collected near the parent $HfC_{0.94}$-interlayer (PC/IL) boundary provide insights into the initial stages of oxidation. Based on HRTEM shown Figure 5E

and Fourier Fast Transforms (FFT) of the HRTEM shown in Figure 6A, there is an amorphous band of oxide material surrounding the parent carbide grain. Electron diffraction patterns in this region show no long-range order/crystalline diffraction spots. This amorphous band of material persists 20 ± 2 nm away from the parent carbide grain before it begins to phase separate, leading to the nanoscale structures shown in Figure 1G-I and Figure 5D. As viewed under HRTEM, the phase separated region appears to comprise hafnia and disordered graphitic carbon with ~3.4 Å d-spacing. The defected nature of the carbon domain corroborates increased D peak intensities seen in Raman spectra as shown in Figure 3. Gasparrini et al. and Shimada et al. also observed interlayer structures in specimens of zirconium carbide oxidized comprised of amorphous carbon and nanocrystalline zirconia precipitates;[14,22] however, the amorphous layer observed herein contains no precipitates.

EELS and EDS chemical analysis of the amorphous region formed upon $HfC_{0.94}$ indicated compositions of $HfO_{2.1}C_{1.0}$ and $HfO_{1.9}C_{0.9}$, respectively. This overall elemental composition likely indicates that the phase forms via selective oxidation where Hf is oxidized without loss of carbon. Selective oxidation is a process wherein a compound or solution is exposed to an oxygen chemical potential sufficient to induce oxidation of thermodynamically less noble constituents while more noble constituents remain stable. This phenomenon may be illustrated using a predominance diagram as shown in Figure 7. If the partial pressure of oxygen at the PC/IL interface at 1300°C and 1 bar total pressure is between $1x10^{-22}$ bar and $2x10^{-17}$ bar, then selective oxidation is predicted to occur and result in two equilibrium phases (i.e., graphite and m-HfO_2).

Microstructure development of the oxide scale is consistent with the sequence shown schematically in Figure 8. During the initial stages of oxidation prior to the formation of a protective outer oxide scale, the local oxygen pressure at the parent carbide boundary is sufficiently high to oxidize both Hf and carbon. The porosity of the oxide scale reflects the necessary volume to allow gaseous oxidation products to escape from the reaction front via Poiseuille flow (pressure-induced flow through long, narrow channels) in proportion to their rate of generation.[12,17] Thus, in the absence of microstructure evolution by diffusion or plastic flow, the observed distribution of porosity through the thickness of the oxide scale acts as a record of the specimen oxidation rate history (i.e., regions with higher amounts of coarse porosity correspond to initially fast oxidation rates, with subsequent decreases in the amount and size of porosity chronicling progression toward a passive oxidation regime). As the oxide scale becomes increasingly protective, diffusive transport becomes rate limiting and overall oxidation kinetics slow, resulting in decreased rates of gaseous product generation. Consequently, scale porosity needed to accommodate escaping gases decreases, which is reflected in observed reductions in apparent pore size approaching the interlayer as shown in Figure 2. Increasing diffusive resistance serves to reduce the oxygen partial pressure at the parent carbide boundary until selective oxidation of Hf becomes thermodynamically favorable and an interlayer forms. Then, the oxidation transformation sequence can be described in three steps: formation of an amorphous HfO_2C_x upon the oxygen-saturated parent carbide; phase separation of the amorphous material into carbon and hafnia domains; and, finally, removal of carbon resulting in a network of fine pores at the IL/OS boundary.

The characteristic size of pores near the IL/OS boundary is commensurate with the final observed degree of coarseness of the carbon domains in the adjoining phase separated interlayer. In addition, the area fraction of pores measured by image thresholding corresponds to the approximate volume percentage of carbon in the starting material, further supporting that the amount and size of pores in this region are inherited from the phase-separated carbon network. Threshold image analysis on three 1 μm x 1 μm regions in the outer oxide scale yielded an average pore fraction of 22 ± 4%, which is close to the volume fraction of carbon calculated from the molar volumes and stoichiometric coefficients of HfO_2 and C (~20%). Threshold image analysis of the interlayer carbon area fraction resulted in values of 19%. The observed porosity near the IL/OS boundary is consistent with values calculated by Holcomb et al. using their counter-current diffusion model, supporting gaseous diffusion through a fine pore network as the rate limiting kinetic mechanism for HfC_x oxidation.[12] Consequently, high temperature oxidation behavior of HfC_x is linked to the phase separation behavior of the amorphous oxidation product and its subsequent coarsening kinetics.

3.2. ADDITIONAL OBSERVATIONS CONCERNING HfC_x OXIDATION SCALE

TEM/STEM observations indicate that the phase separated domains present in the interlayer evolve as a function of crystallite size according to the following sequence: amorphous HfO_2C_x > phase separated c-HfO_2 + C > t-HfO_2 + C > m-HfO_2 + C. The size-dependent stability of HfO_2 polymorphs has been explained by Sharma et al. based on a surface energy relaxation model that predicts a sequence starting from amorphous HfO_2 at a crystallite size less than 3.75 nm, to c-HfO_2 at crystallite sizes ranging 3.75 – 21 nm, then t-HfO_2 between 21 – 38 nm and finally m-HfO_2 at the largest crystallite sizes.[23] Selected

area electron diffraction patterns (SAEDs) (Figure 9B) and FFTs of HRTEM patterns of the oxidized material (see Supplemental Figure 3) show that c-HfO_2 is the first crystalline polymorph that nucleates upon phase separation and that the magnitude of the crystallite size transitions appears consistent with literature. Traces of c-HfO_2 could be detected on the HfC_x side of the PC/IL boundary. When amorphous HfO_2C_x is not present and the HfO_2 crystallites have coarsened appreciably, only spots corresponding to t-HfO_2 and m-HfO_2 are present in the SADPs.[24–26] At the OS/IL boundary, HfO_2 crystallites were observed whose dimensions were dependent on parent carbide composition. For $HfC_{0.94}$, the crystallites were 17-20 nm wide and ~140 nm long, while for $HfC_{0.67}$, the crystallites were ~50 nm wide while remaining similar in length (~154 nm) to $HfC_{0.94}$. These elongated crystallites are likely responsible for the texturing effects observed in XRD.

The origins of texturing can also be observed from the amorphous region as shown in Figure 6C. As the interlayer material is initially developing, HfO_2 and C begin to phase separate and develop a columnar structure that grows outward, eventually impinging on neighboring phase separated domains, leading to the structures shown in Figure 1G-I and Figure 5C. The same type of growth behavior was observed in $HfC_{0.84}$; however, significant differences were noted with regards to $HfC_{0.67}$, as shown in Figure 1G. In $HfC_{0.67}$, the phase separated HfO_2 and C structures appear to grow with the elongated axis parallel to the PC/IL boundary, resulting in discernibly larger crystallites of HfO_2, as well as crystalline bands of HfO_2 that grow continuously from the underlying parent carbide to the outer oxide scale. Chemical analysis of these bands via TEM-EDS indicates the presence of only Hf and O (Supplemental Figure 1).

Nanoindentation measurements performed on the oxidation products of $HfC_{0.94}$ supports the conclusion that the interlayer is composed of a discrete, phase-separated mixture of hafnia and carbon. Results of nanoindentation analyses are summarized in Table 2. For the HfO_2 phase, measured Young's moduli are in close agreement with values reported for nanoindentation performed on HfO_2 thin films; however, measured hardness values are lower than reported for HfO_2 thin films.[27] In several indentation load-displacement curves, crack pop-in behavior was observed, likely due to the presence of microcracks and porosity in the outer oxide layer.

Nanoindentation measurements of parent carbide Young's modulus and hardness indicate values that are lower than those reported for microindentation and nanoindentation of bulk specimens, but that are consistent with values reported for nanoindentation of HfC coatings.[28,29] The hardness values measured for the interlayer material were found to closely match that of the outer oxide layer. This observation is in disagreement with the assessment by Bargeron et al. that the interlayer hardness is comparable to that of the starting carbide.[10] However, these differences might be ascribed to different measurement techniques, as a Berkovich indenter was used in the nanoindentation measurements in the present study, whereas Bargeron et al. used a Knoop indenter.[10] Alternatively, given the higher oxidation temperatures used by Bargeron et al. in their study, it is possible that an interlayer material with different properties was produced as compared to the phase-separated interlayer material reported in this work. Additional study of the interlayer formed upon oxidation as a function of temperature may disambiguate this discrepancy.

Table 2: Berkovich-tip nanoindentation results for the Young's modulus and hardness of the different sample zones of $HfC_{0.94}$.

Young's Modulus (GPa)	**Hardness (GPa)**	**Reference**
Parent carbide		
343±19	19±2	[this work]
N/A	9.5	[10]
350	15	[28]
Interlayer		
150±20	3.3±0.9	[this work]
N/A	9.7	[10]
Outer oxide scale		
85±18	3.3±1.1	[this work]
N/A	2.9	[10]
82	4.9	[27]

4. CONCLUSIONS

The primary conclusion from this work is that the high temperature oxidation behavior of HfC_x is linked to the phase separation behavior of the first amorphous oxidation product HfO_2C_x and its subsequent coarsening kinetics. This conclusion is supported by observation of microstructure evolution of the products formed upon oxidation of dense (>95% theoretical density) HfC_x (x = 0.67, 0.84, or 0.94) at 1300°C and 0.8 mbar oxygen pressure as characterized by Raman spectroscopy, x-ray diffraction, electron microscopy and electron energy loss spectroscopy.

At early stages of oxidation, generation of large volumes of gaseous products leads to the formation of highly porous oxide scale. As the scale thickens, diffusive resistance lowers the oxygen partial pressure at the parent carbide boundary until selective oxidation may occur. Subsequently, the interlayer comprising the selective oxidation products of hafnia and carbon may be formed. At this stage, the HfC_x oxidation sequence comprises oxygen saturation of the parent carbide followed by transformation to amorphous HfO_2C_x, phase separation into turbostratic carbon and hafnia polymorphs varying from cubic to tetragonal/monoclinic as crystallite domains coarsen from ~2-20 nm, and finally carbon removal via oxidation from the phase separated interlayer. The porosity in the oxide scale immediately adjacent to the interlayer appears to be inherited from that of the prior carbon in the phase separated region and is generally consistent with calculated literature values for gaseous diffusion rate-limited kinetic models.

Indentation measurements performed on the interlayer material support the proposed model of oxidation of HfC at this temperature but may not correspond to higher

temperature oxide scale morphologies, as the hardness of the interlayer material was closer to that of the pure oxide, rather than possessing hardness analogous to the underlying parent carbide.

ACKNOWLEDGEMENTS

This material is based upon research supported by, or in part by, the U. S. Office of Naval Research under award number N00014-17-1-2931 (Dr. Eric Marineau, program officer, and Dr. Eric Wuchina, technical advisor). The authors gratefully acknowledge:

- Dr. Eric Bohannon and the Missouri S&T Materials Research Center (MRC) and Advanced Materials Characterization Lab (AMCL) for use of facilities for x-ray diffraction and Raman spectroscopy analysis.
- University of Missouri Electron Microscopy Core Facility for assistance with SEM/FIB/TEM and partial funding through the Excellence in Electron Microscopy Award.
- Dr. Matthew Maschmann, Dr. Cherian Joseph Mathai, and the University of Missouri Advanced Nanostructures Group for assistance with nanoindentation.

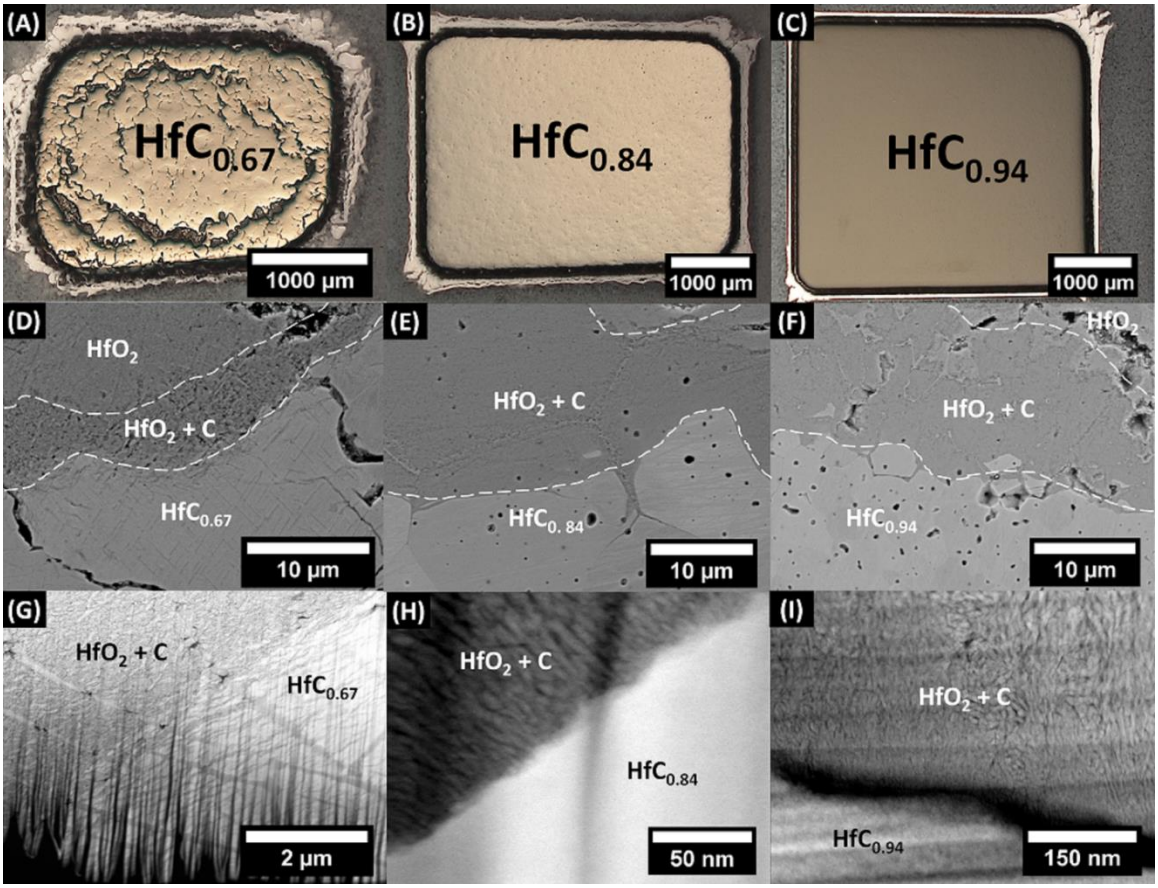

Figure 1: Composite image showing the observed morphology of the oxide scale/interlayer material as a function of carbon content. (a-c) Optical micrographs showing macroscopic scale morphology as a function of carbon content. In each micrograph, a polished carbide core is observed, immediately surrounded by a dark, black inner oxide layer containing free, graphitic carbon and a light, white outer oxide layer. (d-f) SEM images showing the innermost interface for each specimen as a function of carbon content. (g-i) STEM-HAADF images showcasing the differences in oxide scale morphology of the interlayer as a function of carbon content. At “low” carbon contents, microstructure development is markedly different than at “intermediate” and “high” carbon contents.

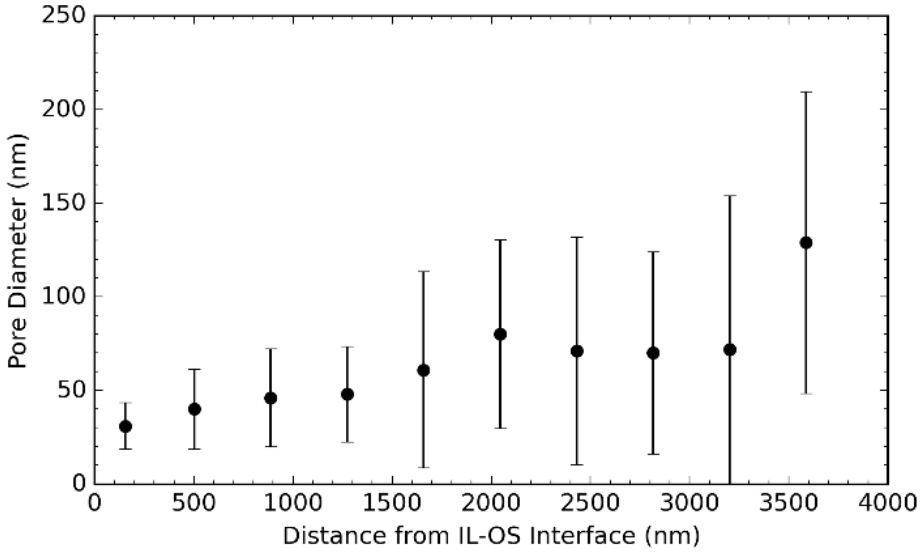

Figure 2: Plot of pore size (diameter) as a function of distance from the interlayer-oxide scale interface on $HfC_{0.94}$.

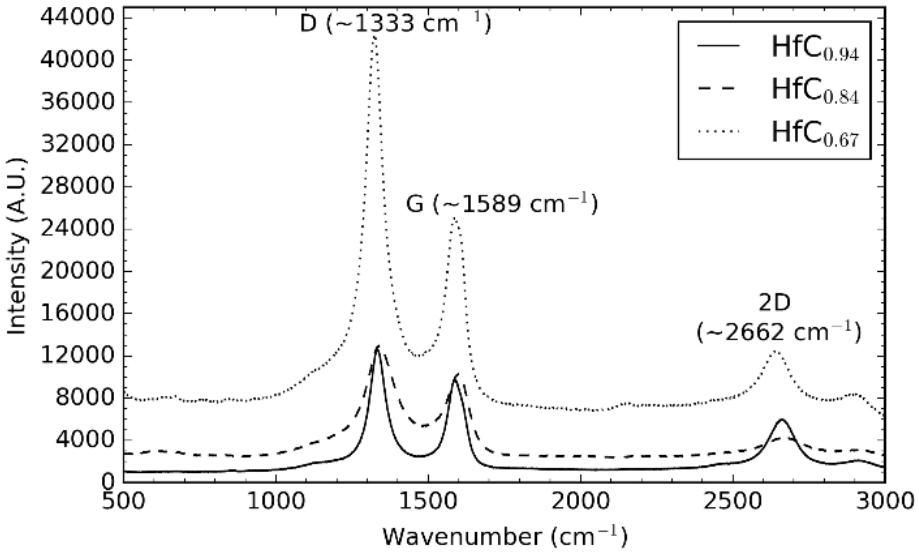

Figure 3: Raman spectra collected from the innermost oxide scale of the oxidized HfC_x specimens. Peaks attributed to graphitic carbon dominate the spectrum, but some trace peaks of hafnia can be observed at lower wavenumbers.

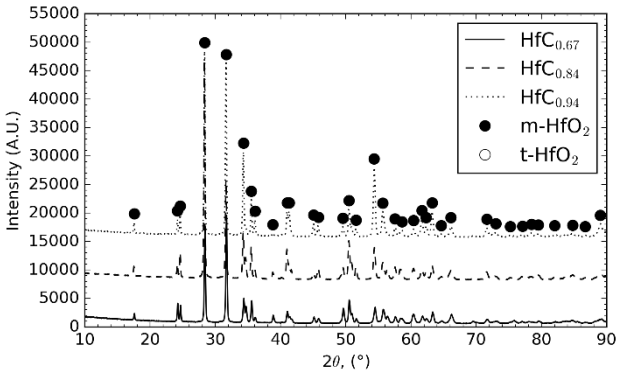

Figure 4: XRD patterns (Cu-Kα λ = 0.1541 nm) of the top surface of the oxide scale on oxidized $HfC_{0.67}$, $HfC_{0.84}$ and $HfC_{0.94}$ indicating strong texturing of the hafnium oxide. m-HfO_2 (PDF #01-074-1506) exhibits texturing-based intensity changes in the (200) and $(\bar{2}02)$ reflections.

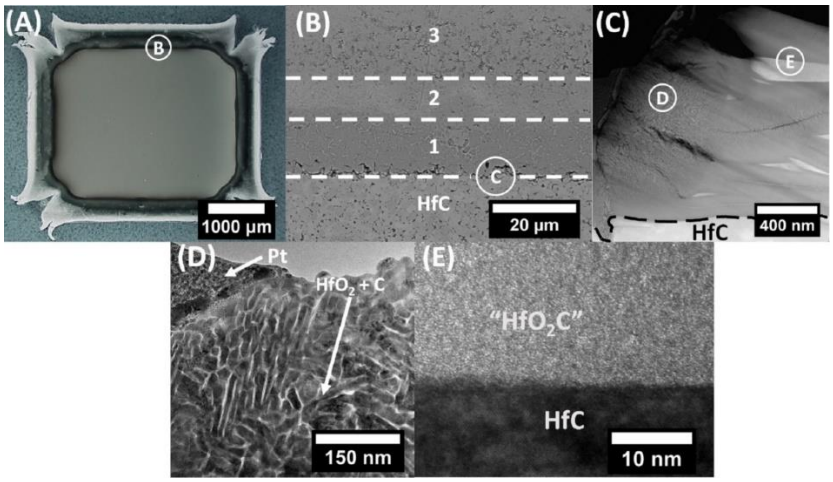

Figure 5: Oxidation products of $HfC_{0.94}$ (T = 1300°C, pO_2 = 0.08 kPa, t = 4 hr) from macro- to nano-scale. Letters in circles indicate the representative region of the corresponding panel. (A) Optical micrograph of an oxidized HfC specimen showing the "Maltese Cross" shape. (B) SEM image of the oxide scale showing three distinct layers. (C) STEM – HAADF image of the interface between HfC and zone 1, which possesses an initially amorphous material around the vicinity of the HfC that proceeds to phase separate. (D) Bright-field TEM image showing the fine phase-separation of the oxide scale into crystalline HfO_2 (dark) and graphite (bright). (E) Close-up BF TEM image of the amorphous material near grains of HfC.

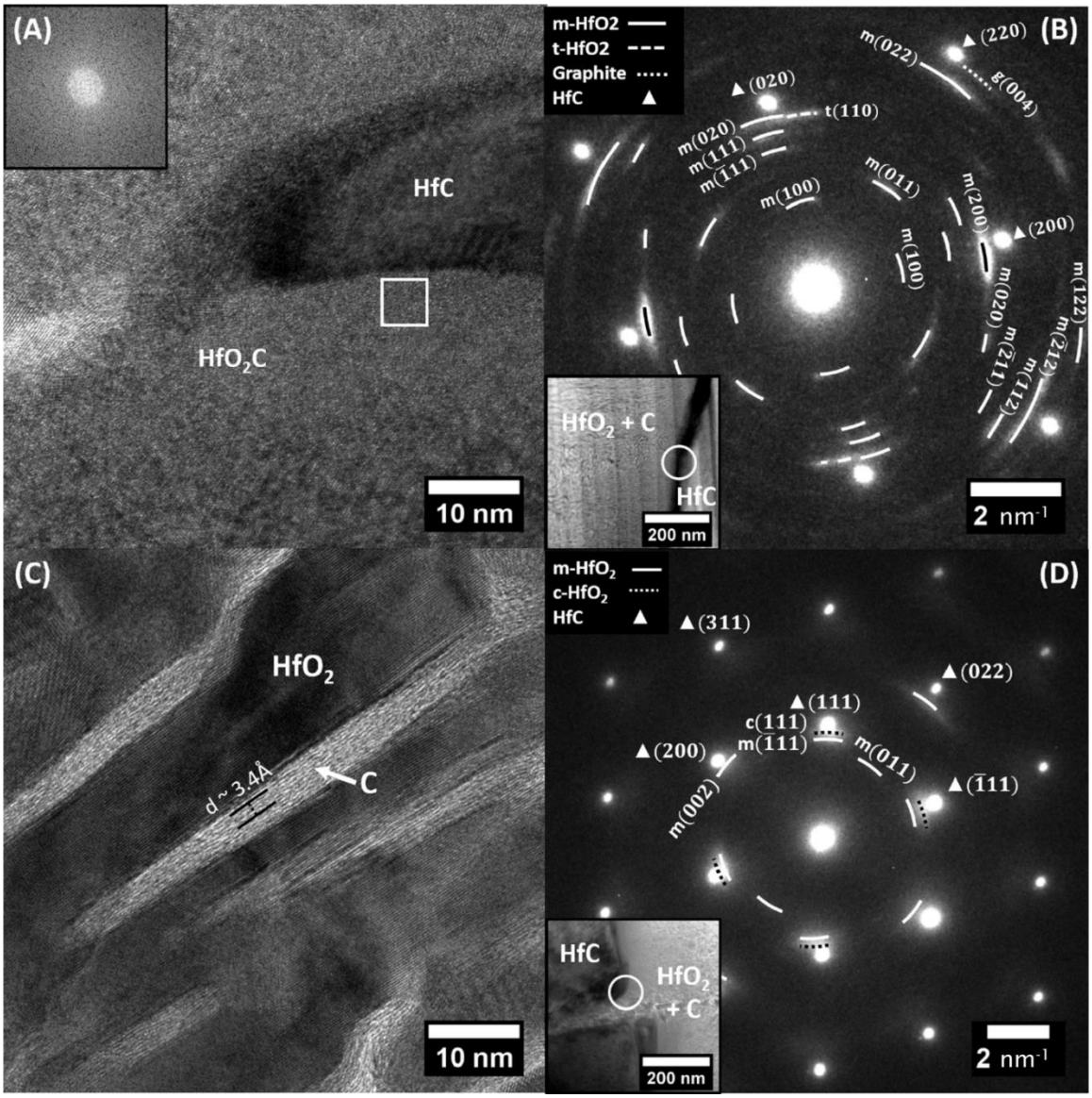

Figure 6: A) Brightfield TEM image of oxidized $HfC_{0.94}$ with an inset FFT showing the amorphous nature of the initial oxide scale. B) SAED pattern of a TEM lift-out near the phase-separated region along the [**001**] zone axis of HfC containing crystallites of t-HfO_2 and graphite. C) Brightfield HRTEM image of phase-separated HfO_2 (dark) and C (bright) after crystallization and coarsening. C (002) lattice fringes are visibly buckled and distorted. D) SAED pattern of a TEM lift-out near the amorphous region along the [**1$\bar{1}$0**] zone axis of $HfC_{0.94}$. Textured m- and c-HfO_2 that were polycrystalline in nature were detected, as was C.

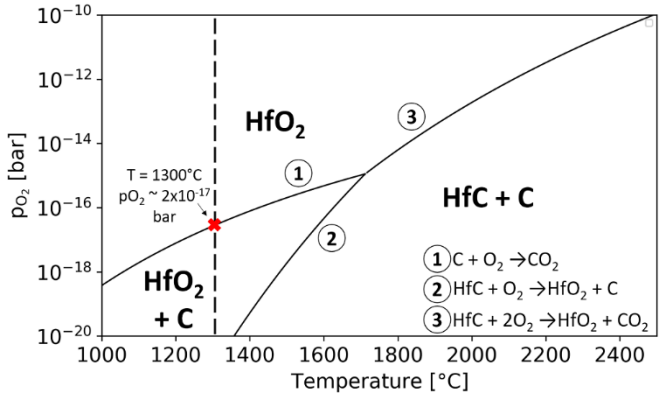

Figure 7: Predominance diagram showing the regions of phase stability during the oxidation of stoichiometric HfC at 1 bar total pressure. Carbon refers to graphite as standard reference state.

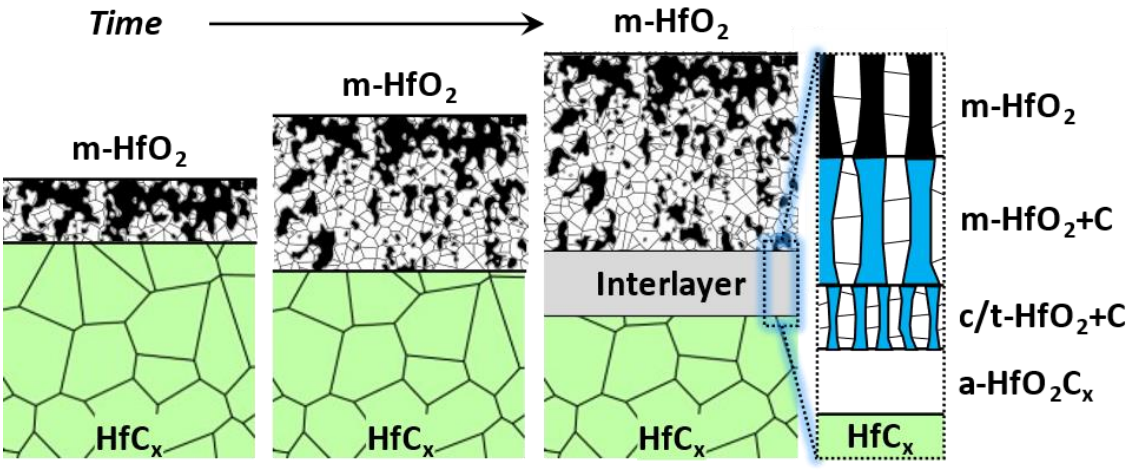

Figure 8: Schematic illustration of high temperature oxidation of HfC. First, HfO_2 oxide scales with coarse porosity are formed. Subsequently, the size and total volume of porosity is reduced in proportion to the rate of oxidation at the PC/IL interface. If a sufficiently protective oxide scale is formed, then the local oxygen pressure at the PC/IL interface eventually reaches a threshold for selective oxidation of hafnium with carbon formation. The transformation sequence then proceeds from an initial amorphous HfO_2C_x product that phase separates into c/t-HfO_2 + C followed by polymorphic transformations to lower symmetry HfO_2 as crystallites coarsen. The IL/OS interface denotes oxidation of phase separated carbon domains to yield a fine scale pore network that apparently controls the rate of gaseous diffusion and thereby determines high temperature oxidation kinetics of HfC.

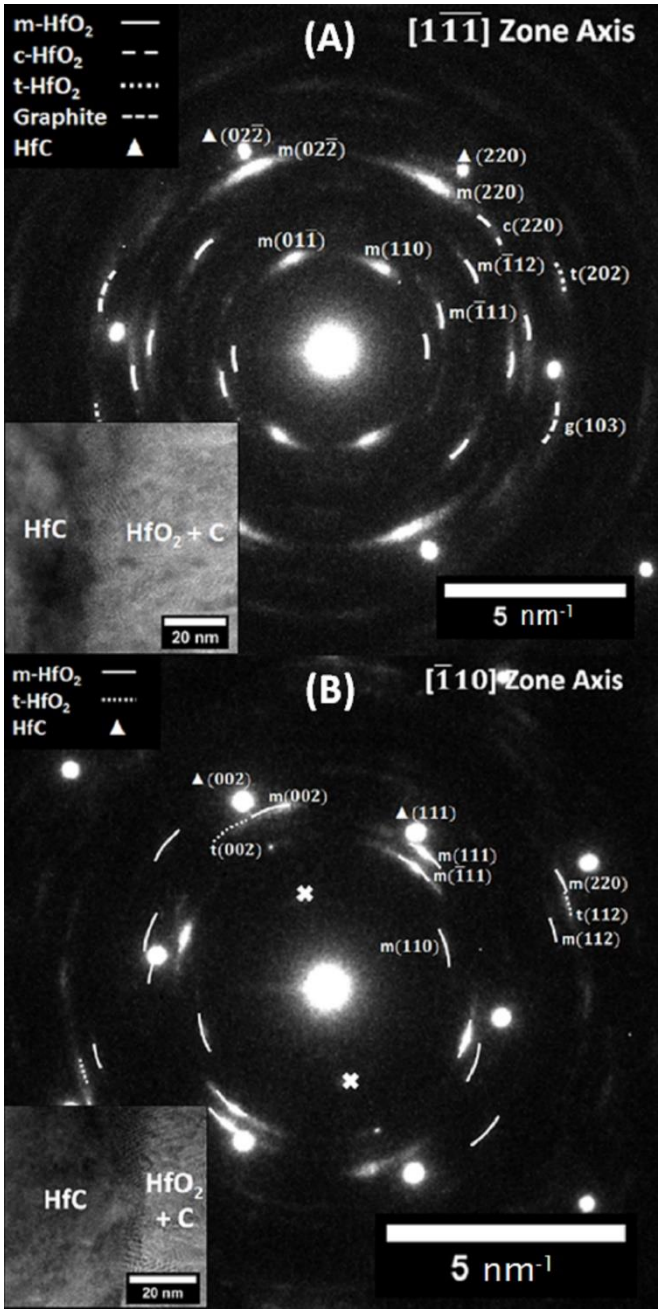

Figure 9: Selected area electron diffraction patterns (SAED) of (A) $HfC_{0.84}$ along [$\mathbf{1\bar{1}\bar{1}}$] zone axis and (B) $HfC_{0.94}$ along [$\mathbf{\bar{1}10}$] zone axis. Epitaxial growth with a slight misorientation is present in both cases.

REFERENCES

1. Fleischer RL. High-Temperature, High-Strength Materials - An Overview. *J Met*. 1985; 37 (12):16–20.

2. Fahrenholtz, W.G., Wuchina, E.J., Lee, W.E., Zhou Y. Ultra-High Temperature Ceramics Materials for Extreme Environment Applications. 1st ed. Hoboken, NJ: John Wiley & Sons;

3. Binner J, Porter M, Baker B, *et al*. Selection, processing, properties and applications of ultra-high temperature ceramic matrix composites, UHTCMCs–a review. *Int Mater Rev*. 2020; 65 (7):389–444.

4. Wang CR, Yang JM, Hoffman W. Thermal stability of refractory carbide/boride composites. *Mater Chem Phys*. 2002; 74 (3):272–281.

5. Okamoto H. The C-Hf (carbon-hafnium) system. *Bull Alloy Phase Diagrams*. 1990; 11:396–403.

6. Shin D, Arróyave R, Liu Z-K. Thermodynamic modeling of the Hf-Si-O system. *Comput Coupling Phase Diagrams Thermochem*. 2018; 1 (0):1–13.

7. Opeka MM, Talmy IG, Zaykoski JA UHTCs Oxidation-based materials selection for 2000^{o}C+. *J Mater Sci*. 2004; 9 (39):5887–5904.

8. Wuchina, EJ, Opeka M. The Oxidation Behavior of HfC, HfN, and HfB2. *High Temp Corros Mater Chem III*. 2001; 3:136–143.

9. Shimada S, Yunazar F. Oxidation of Hafnium Carbide and Titanium Carbide Single Crystals with the Formation of Carbon at High Temperatures and Low Oxygen Pressures. *J Am Ceram Soc*. 2000; 28 (189395):721–728.

10. Bargeron CB, Benson RC, Newman RW, Jette AN, Phillips TE. Oxidation mechanisms of hafnium carbide and hafnium diboride in the temperature range 1400 to 2100°C. *Johns Hopkins APL Tech Dig Applied Phys Lab*. 1993; 14 (1):29–36.

11. Réjasse F, Rapaud O, Trolliard G, Masson O, Maître A. Experimental investigation and thermodynamic evaluation of the C–Hf–O ternary system. *J Am Ceram Soc*. 2017; 100 (8):3757–3770.

12. Holcomb GR, Pierre GRS. Application of a counter-current gaseous diffusion model to the oxidation of hafnium carbide at 1200 to 1530°C. *Oxid Met*. 1993; 40 (1–2):109–118.

13. ASTM International. Standard Test Methods for Density of Compacted or Sintered Powder Metallurgy (PM) Products Using Archimedes' Principle. *Astm B962-13*. 2013:1–7.

14. Gasparrini C, Podor R, Horlait D, Chater R, Lee WE. Zirconium Carbide Oxidation: Maltese Cross Formation and Interface Characterization. *Oxid Met*. 2017; 88 (3–4):509–519.

15. Shimada S. Oxidation and Mechanism of Single Crystal Carbides with Formation of Carbon. *J Ceram Soc Japan*. 2001; 109 (1267):S33–S42.

16. Voitovich RF, Pugach EA. High-temperature oxidation of ZrC and HfC. *Sov Powder Metall Met Ceram*. 1973; 12 (11):916–921.

17. Metcalfe AG. Gas Evolution During Oxidation of Refractory Borides and Carbides at 1500°C to 2700°C. *ECS Trans*. 2019; 3 (14):131–142.

18. Ferrari A, Robertson J. Interpretation of Raman spectra of disordered and amorphous carbon. *Phys Rev B - Condens Matter Mater Phys*. 2000; 61 (20):14095–14107.

19. Ferrari AC. Raman spectroscopy of graphene and graphite: Disorder, electron-phonon coupling, doping and nonadiabatic effects. *Solid State Commun*. 2007; 143 (1–2):47–57.

20. Mehltretter AH, Bradley MJ. Forensic Analysis and Discrimination of Duct Tapes. *Jastee*. 2012; 3 (1).

21. Rodriguez-Navarro AB. Model of texture development in polycrystalline films growing on amorphous substrates with different topographies. *Thin Solid Films*. 2001; 389 (1–2):288–295.

22. Shimada S. TEM Observation of the ZrC / ZrO 2 Interface Formed by Oxidation of ZrC Single Crystals. 1998; 6 (3):191–195.

23. Sharma G, Ushakov S V., Navrotsky A. Size driven thermodynamic crossovers in phase stability in zirconia and hafnia. *J Am Ceram Soc*. 2018; 101 (1):31–35.

24. Luo X, Demkov AA. Structure, thermodynamics, and crystallization of amorphous hafnia. *J Appl Phys*. 2015; 118 (12).

25. Parija A, Waetzig GR, Andrews JL, Banerjee S. Traversing Energy Landscapes Away from Equilibrium: Strategies for Accessing and Utilizing Metastable Phase Space. *J Phys Chem C*. 2018; 122 (45):25709–25728.

26. Ushakov S V., Navrotsky A, Yang Y, *et al.* Crystallization in hafnia- and zirconia-based systems. *Phys Status Solidi Basic Res*. 2004; 241 (10):2268–2278.

27. Wiatrowski A, Obstarczyk A, Mazur M, Kaczmarek D, Wojcieszak D. Characterization of HfO2 Optical Coatings Deposited by MF Magnetron Sputtering. *Coatings*. 2019; 9 (2):106.

28. Sciti D, Guicciardi S, Nygren M. Densification and mechanical behavior of HfC and HfB2 fabricated by spark plasma sintering. *J Am Ceram Soc*. 2008; 91 (5):1433–1440.

29. Wang YL, Xiong X, Li GD, *et al.* Ablation behavior of HfC protective coatings for carbon/carbon composites in an oxyacetylene combustion flame. *Corros Sci*. 2012; 65:549–555.

APPENDIX

ADDITIONAL CHARACTERIZATION OF OXIDIZED SPECIMENS

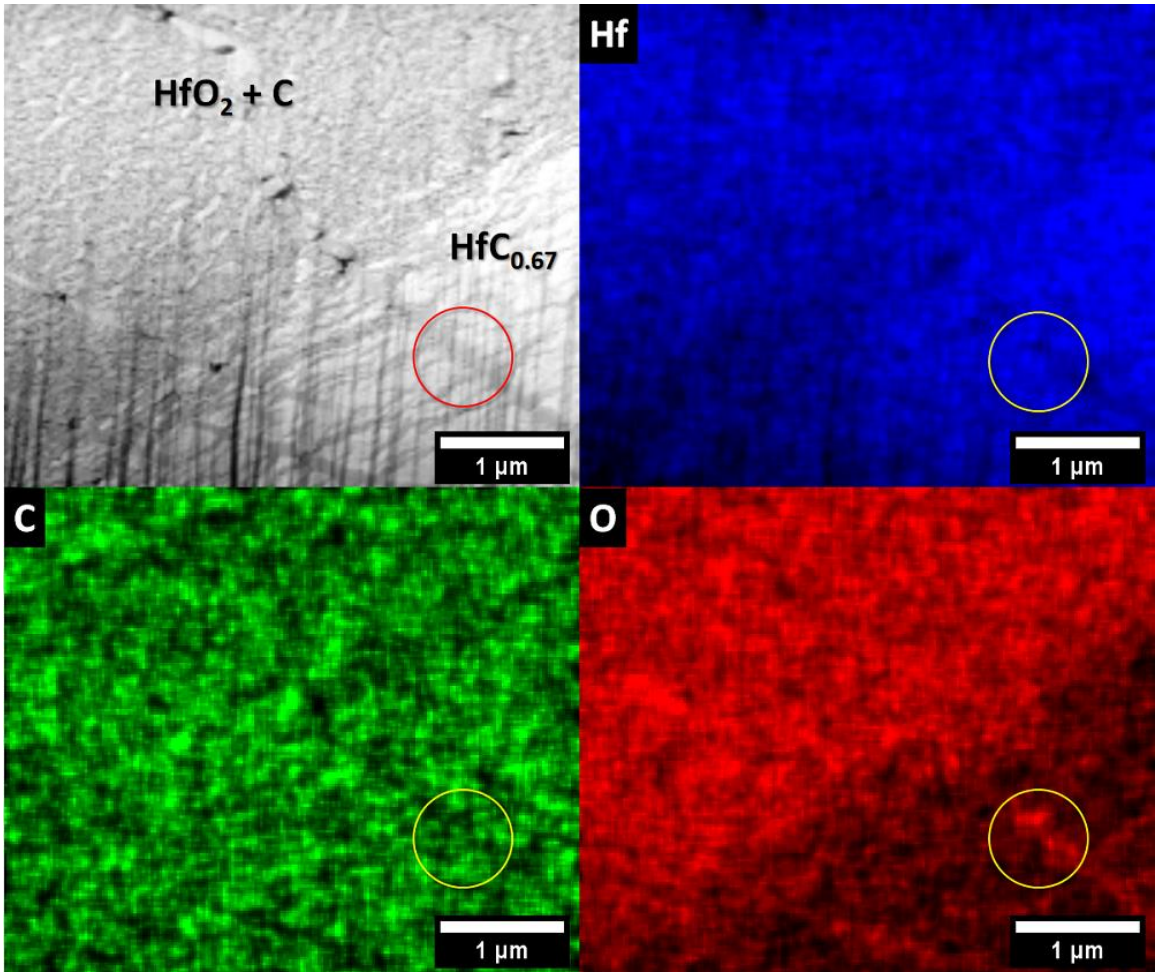

Supplemental Figure 1: TEM-EDS maps of $HfC_{0.67}$ showing the distribution of Hf, C and O near the carbide/interlayer interface.

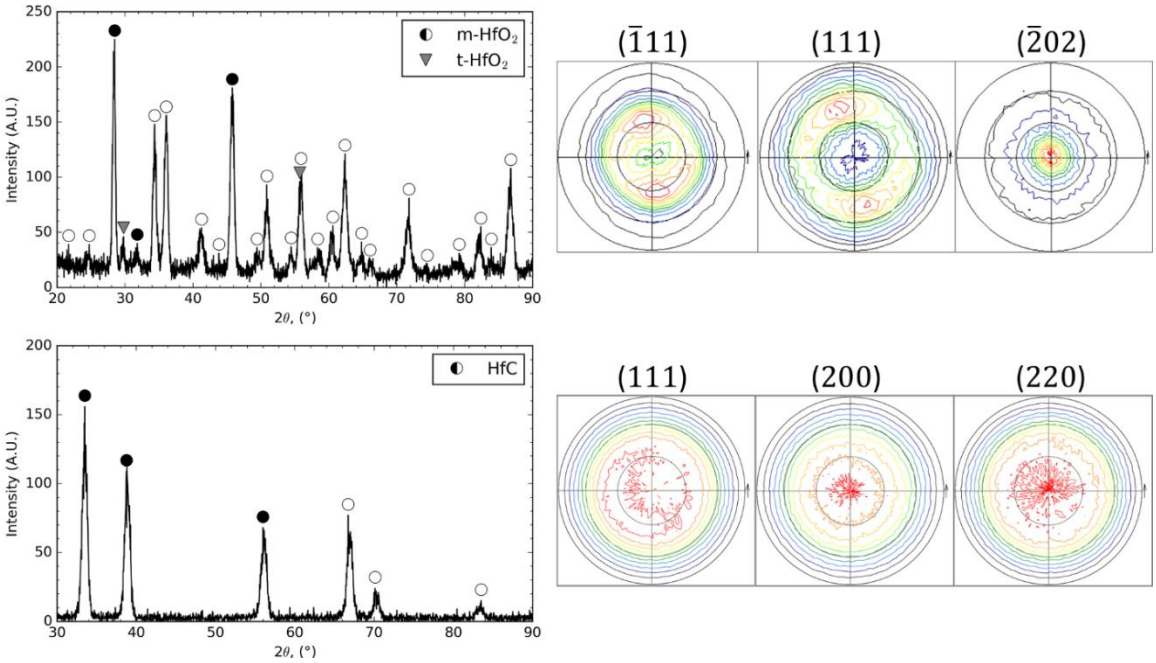

Supplemental Figure 2: (Top) XRD Diffraction scans (Cu-Kα λ = 0.1541 nm) of oxide scale formed via oxidation of $HfC_{0.94}$. Primarily, peaks for m-HfO_2 (PDF #01-074-1506) were observed; however, some small amounts of t-HfO_2 (PDF #04-005-5599) peaks were also observed. (Bottom) XRD scans of the parent $HfC_{0.94}$ material before oxidation showing a lack of initial texture. Pole figures correspond from left to right with the peaks labelled with a black circle. Planes in the oxide analyzed via pole figures were selected based on the largest observed differences between calculated intensities and observed intensities.

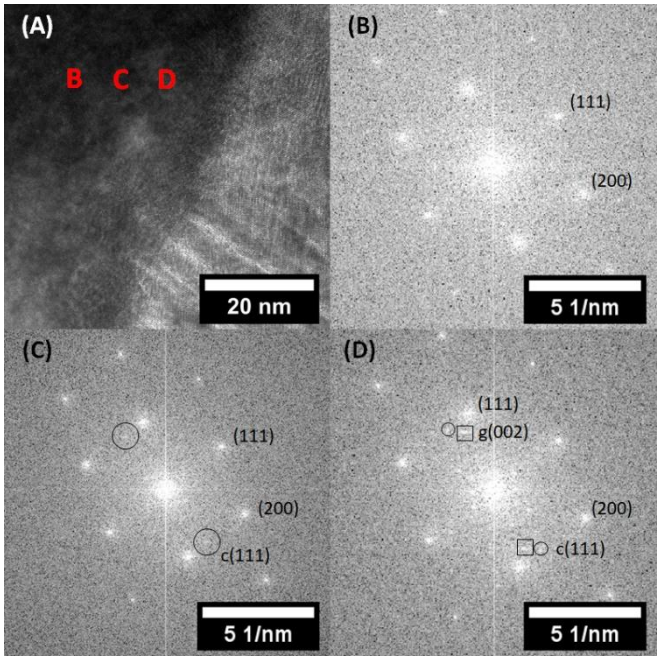

Supplemental Figure 3: A): Brightfield TEM image of interlayer immediately phase-separating adjacent to a grain of $HfC_{0.94}$ on the left. In the three regions indicated by red letters, the initial formation of nuclei of c-HfO_2 (traces of c-HfO_2 (111) plane) was observed by FFT analysis. c-HfO_2 was the first observed phase to form ~20 nm BEFORE the oxide scale interface, followed by graphitic carbon (traces of graphite (002) plane).

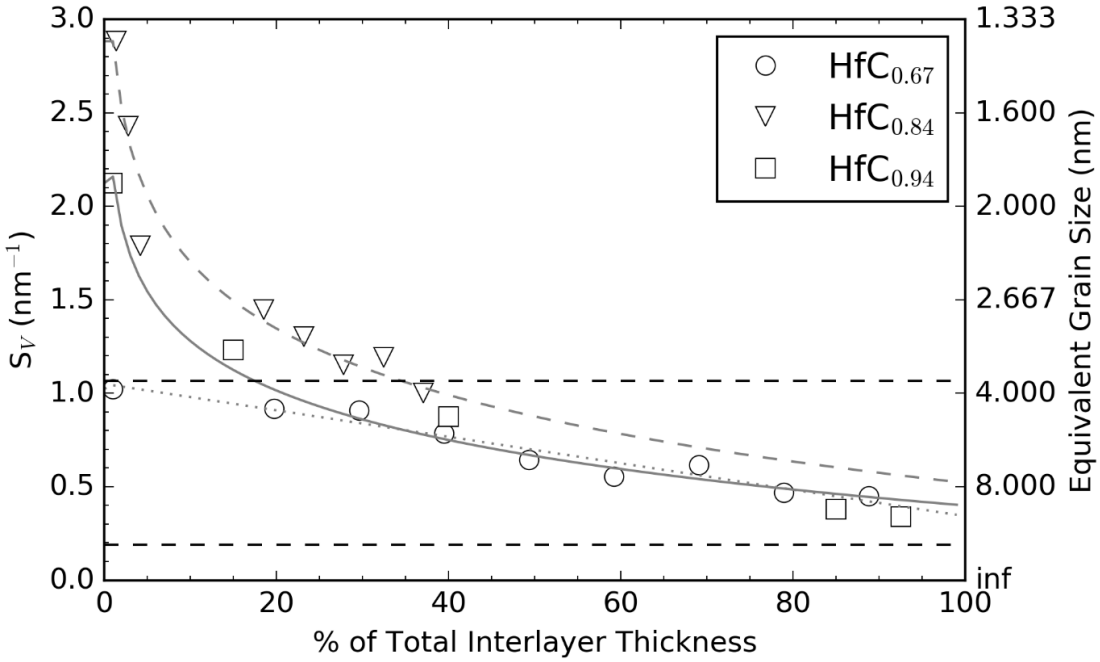

Supplemental Figure 4: Plot of surface area-to-volume ratio (S_V) of HfO_2 crystallites within the phase-separated region of the interlayer showing that HfO_2 crystallites coarsen as a function of distance away from the interface between HfC and the interlayer. Dashed black lines denote the critical S_V's corresponding to a-HfO_2>c-HfO_2 transformation (top line) and the c-HfO_2>t-HfO_2 transformation (bottom line) [27]. S_V values are calculated assuming cylindrical geometry.

II. HIGH TEMPERATURE OXIDATION REGIME TRANSITIONS IN HAFNIUM CARBIDE

Submitted to the Journal of the American Ceramic Society

Jonathan A. Scott[a], Xiaoqing He[b], David W. Lipke[a]

a) Department of Materials Science & Engineering, Missouri University of Science and Technology, Rolla, MO 65409, USA

b) Electron Microscopy Core and Department of Mechanical & Aerospace Engineering, University of Missouri, Columbia, MO 65211, USA

ABSTRACT

Understanding the oxidation behavior of hafnium carbide is crucial to its application in extreme environments. In this work, the transition in high temperature oxidation kinetics regimes in hafnium carbide is explained based on phase equilibria considerations supported by observed changes in oxide scale microstructure evolution associated with different transformation pathways. Below a composition-dependent critical temperature and oxygen pressure, hafnium carbide first transforms to an amorphous material with nominal composition HfO_2C followed by phase separation into carbon and hafnia domains. Subsequently, gaseous transport through a nanometric pore network formed by oxidative removal of phase-separated carbon becomes rate-limiting. Above this critical point, the oxidation sequence involves direct transformation from hafnium carbide to hafnia and gaseous products, leading to dissimilar scale morphologies responsible for the reported transition from gaseous to solid-state diffusion limited oxidation regimes at ultra-high temperatures.

1. INTRODUCTION

Hafnium carbide possesses the highest known melting point of any compound (estimated at 4232 ± 84 K,[1] 4201 ± 20K,[2,3] and 4223 ± 40K[4]) which, in combination with the refractory character of its primary oxidation product hafnia, makes it an attractive candidate for extreme environment applications. Despite the thermal stability of hafnium carbide, its limited high temperature oxidation resistance has motivated numerous studies into its oxidation behavior, including kinetic studies in controlled-atmosphere furnace conditions up to 2100°C [5-8] or using custom laser-heated apparatus up to 2250°C,[9] as well as assessments of oxidative ablation resistance in arc-jet[10] or oxyacetylene torch test conditions[11] at surface temperatures exceeding the melting point of hafnia. Reviews of prior works highlight several key findings.[12,13] Under most test conditions, the oxide scale microstructure is reported to comprise two distinct product layers: a porous outer layer of monoclinic hafnia and a dense carbon-containing interlayer adjacent to the parent carbide. Parabolic oxidation kinetics are generally observed above 1200°C and attributed to diffusion-limited scale growth across two different temperature regimes. At 1200-1550°C, a model for gaseous diffusion through a nanometric pore network is consistent with observed temperature and oxygen partial pressure dependencies of determined parabolic rate constants. Recent work by the present authors has revealed the detailed morphology and mechanism by which the carbon-containing interlayer forms.[14] The layer comprises interconnected nanocrystalline domains of monoclinic hafnia and defected graphitic carbon. The phase evolution sequence resulting in this morphology comprises three steps. First, the oxygen-saturated parent carbide forms a short-lived amorphous phase of nominal

composition HfO_2C. Second, phase separation into hafnia and carbon domains occurs. Third, hafnia progresses from cubic/tetragonal to monoclinic as a function of crystal size as the phase separated domains coarsen. The nanometric pore network responsible for limiting transport via gaseous diffusion as first modeled by Holcomb and St. Pierre[15] was shown to result from oxidative removal of carbon with the pore structure inherited from the phase separated carbon domain.

Above ca. 1800°C, comparatively stronger temperature dependence of observed parabolic rate constants is consistent with dissolution of oxygen into the parent carbide via solid-state diffusion. Detailed morphological studies of the oxide scale in the temperature regime where solid-state diffusion of oxygen appears to be rate limiting have not been previously reported. In this work, the high temperature oxidation behavior of hafnium carbide is studied with the purpose of understanding and rationalizing microstructural origins of the transition between oxidation regimes.

2. MATERIALS AND METHODS

Hafnium carbide powder ($HfC_{0.94}$, −325 mesh; H.C. Starck; Newton, MA) was ball milled in acetone for four hours, dried on a rotary evaporator, and passed through a 50-mesh sieve before loading into a graphite foil-lined graphite die. Dense billets were obtained via spark plasma sintering (SPS) (DCS-10; Thermal Technology LLC; Minden, NV) at 2200°C, 32 MPa for 5 minutes. After SPS consolidation, any adhered graphite foil or flashing was removed using 80-grit SiC sandpaper and billets were machined to be flat and parallel using a diamond surface grinder. Specimens for oxidation tests, ca. 4 × 4 × 4 mm cubes, were cut from machined billets via electric discharge machining (EDM),

surface ground using 220-grit SiC sandpaper, and ultrasonically cleaned to remove brass deposits from the EDM process. Portions of machined billets were crushed in a hammer mill for elemental analysis (CS600; LECO Corporation; St. Joseph, MI) to confirm carbon content.

Oxidation testing was conducted in a custom arc-image optical heating facility comprising four 6.5 kW Xenon short-arc lamps housed in ellipsoidal mirrors (Sciencetech Inc.; London, ON, Canada). Light cones are focused onto a nominal one-inch diameter spot inside a vacuum chamber (12×12×12 Cubic Modular Vacuum Chamber; Ideal Vacuum Products, LLC; Albuquerque, NM) through a fused silica window. Specimens are placed within a water-cooled copper hearth on a yttria-stabilized zirconia setter plate and the chamber position is adjusted so that the top of the specimen coincides with the lamp focal plane. A water-cooled off-axis parabolic mirror whose focus is coincident with that of the lamps enables monitoring of specimen temperature using an emissivity-correcting spectral pyrometer (FMPI Spectropyrometer; FAR Associates; Macedonia, OH). A shutter system comprising four high-speed stepper motors with anodized aluminum leaves is used to momentarily block lamp irradiance during temperature measurement to eliminate spectral contamination. Shutter closure times were adjusted to ensure adequate time for signal acquisition without excessive radiative heat loss from specimens (500 ms was found to be suitable under tested conditions).

Oxidation experiments were performed by evacuating and backfilling the vacuum chamber with argon gas under continuous 500 cm^3/min. flow. Heating was conducted by increasing lamp power in increments of ten percent maximum rated current every five minutes, with shuttered specimen temperature measurements taken after each increment

had elapsed. Upon attaining target specimen temperatures, gas flows were switched to a blend of one percent oxygen in argon at 50 cm^3/min. flow for thirty-minute test durations with temperature measurements taken every ten minutes to verify the test condition was maintained. Upon completion of each experiment, lamp power was shut off and the gas flow switched to argon gas at 500 cm^3/min. flow.

Oxidized specimens were mounted, sectioned, and polished to 0.25 μm finish, and their oxide scales were investigated using scanning electron microscopy (SEM), Raman spectroscopy (LabRAM Aramis; HORIBA Jobin Yvon; Kyoto, Japan), and X-ray diffraction (XRD) (X'Pert MRD; Malvern PANalytical Ltd.; Malvern, UK). Raman spectra were collected from 500 to 3000 cm^{-1} using an HeNe laser (λ = 632.8 nm). A focused ion beam (FIB) (Scios DualBeam FIB SEM; FEI; Hillsboro, OR) was used to lift out specimens perpendicular to the interface between the parent carbide and oxide scale, which were subsequently analyzed using transmission electron microscopy (TEM) (Thermo Fisher Scientific Spectra 300; FEI; Waltham, MA), scanning transmission electron microscopy (STEM), energy dispersive X-ray spectroscopy (EDS), and selected area electron diffraction (SAED).

3. RESULTS

Oxide scales formed upon hafnium carbide markedly differ near its reported oxidation regime transition as evidenced by microstructural analyses of $HfC_{0.94}$ specimens oxidized above and below 1800°C. Specimens oxidized below ca. 1800°C (Figure A) displayed two distinct product layers comprising porous hafnia layer atop a relatively dense interlayer. Phase identification analyses of XRD scans taken from the top surface of specimens

oxidized below ca. 1800°C indicated single-phase monoclinic hafnia with no other polymorphs observed above the phase detection limit of the diffractometer. Specimens oxidized above ca. 1800°C (Figure B) displayed only a single porous (ca. 15% porosity) hafnia layer absent any discernable interlayer, with trace amounts of tetragonal hafnia retained among primarily monoclinic hafnia product. Total oxide scale thicknesses varied with temperature at constant 30 min. exposure (75 ± 2 μm at 1810°C vs. 50 ± 2 μm at 1707°C vs. 126 ± 2 μm at 1668°C). It is speculated that enhanced sintering of the hafnia scale (ca. 5% porosity) near the gas-solid interface where irradiant intensity is greatest may have helped to establish an effective barrier to oxygen ingress during testing; however, the authors urge caution in making direct comparisons of scale thickness as a metric for oxidation kinetics given differing scale morphologies.

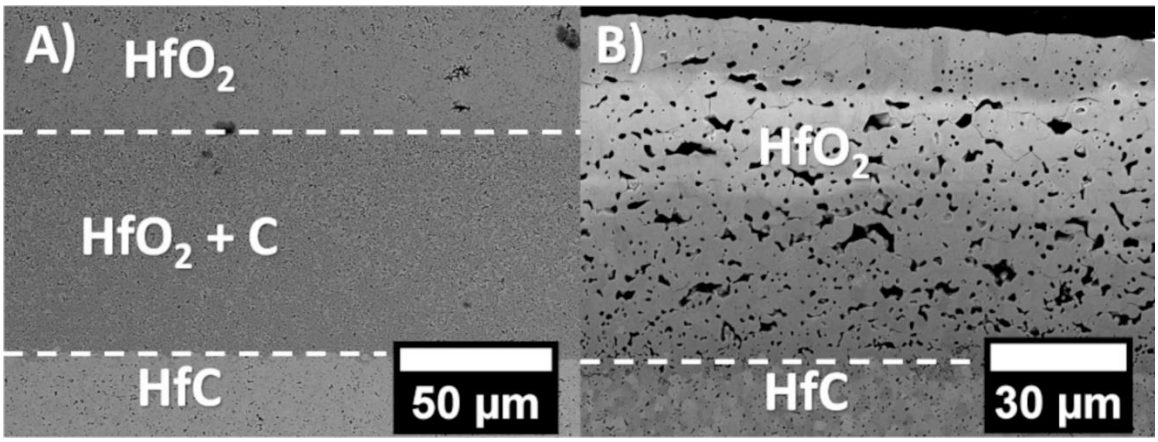

Figure 1: Representative SEM micrographs illustrating the differences in microstructure between samples of $HfC_{0.94}$ oxidized at 1668°C (A) and 1810°C (B).

Raman spectroscopy from the interlayer region near the interface with the parent carbide on specimens oxidized below ca. 1800°C (Figure 2A) produced strong, characteristic peaks associated with graphite as well as some lower intensity peaks ranging

from 100-1000 cm^{-1} corresponding to monoclinic hafnia. For each sample, the intensity ratios of D-band to G-band peaks, I(D)/I(G), varied; however, all ratios were less than 1, indicating a more strongly ordered graphite structure. This is supported by the position of the G band of graphite being at ~1580 cm^{-1}, rather than being positioned at larger wavenumbers, which is characteristic of lower graphitization. For a given specimen, I(D)/I(G) ratios decreased with distance from the parent carbide (Figure 2B), consistent with coarsening of the graphitic domains. Similarly, I(D)/I(G) ratios also decrease with oxidation temperature at similar positions within the interlayer (e.g., nearest the parent carbide interface, I(D)/I(G) ≈ 0.98 for specimens oxidized at 1668°C versus I(D)/I(G) ≈ 0.46 for specimens oxidized at 1707°C). In specimens oxidized above ca. 1800°C, Raman spectra of the oxide scale immediately adjacent to the parent carbide indicate trace peaks likely corresponding to carbon; however, primary observed Raman peaks were all attributable to monoclinic hafnia. Within the oxide scale at all locations except immediately adjacent to the parent carbide, graphitic peaks were absent from Raman spectra.

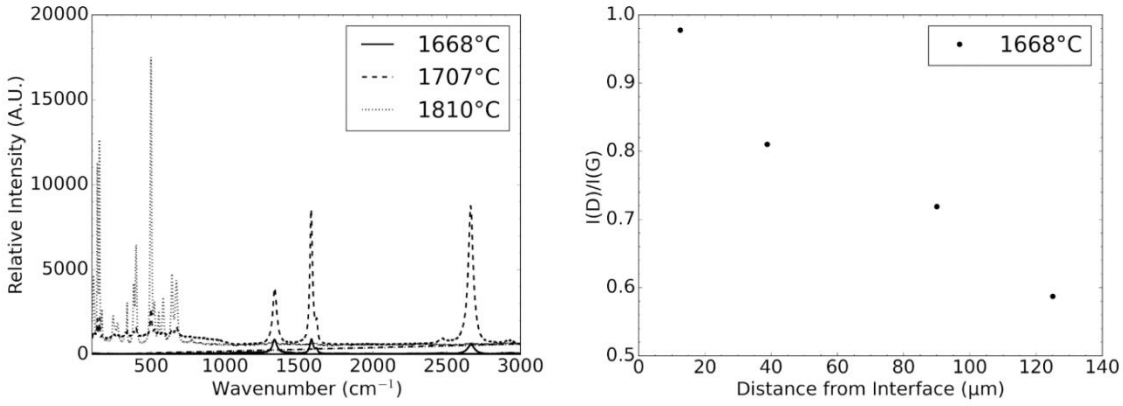

Figure 2: (A): Raman spectra for $HfC_{0.94}$ specimens oxidized at 1668°C, 1707°C, and 1810°C. For the specimen oxidized at 1810°C, no bulk graphitic carbon is observed. (B): I(D)/I(G) ratio as a function of position for $HfC_{0.94}$ oxidized at 1668°C.

TEM analyses of the $HfC_{0.94}$ specimen oxidized at 1668°C reveal the presence of a two-phase mixture of hafnia and carbon (Figure 3A) whose morphology is similar albeit coarsened as compared to those reported previously on scales oxidized at lower temperatures.[14] Hafnia crystallites varied from ca. 40 nm near the parent carbide interface to ca. 70 nm at a distance of 330 nm from the interface while carbon domain sizes varied from ca. 5-13 nm and interlamellar spacings varied from ca. 50-80 nm in the same region. Selected area diffraction patterns taken at the interface between the parent carbide and the oxide scale (Figure 4B) revealed a growth relationship between the carbon domains and the parent carbide. Reciprocal lattice vectors corresponding to the (002) plane of graphite and the (111) of hafnium carbide were rotated by approximately 8°, indicating that graphitic domains likely grow from the closest-packed carbon planes of the parent carbide. TEM observations of the interface between hafnia crystallites and carbon domains indicates that the $(\bar{1}11)$ plane of monoclinic hafnia forms a coherent interface with the graphite (002) planes. TEM-EDS analyses near the interface (Figure 4C-E) shows a planar interface whereby the parent carbide decomposes into hafnia and carbon domains. In contrast, TEM analyses of the $HfC_{0.94}$ specimen oxidized at 1810°C (Figure 3B) showed a substantially different scale morphology compared to samples oxidized below 1800°C. Most notably, the observed oxide scale shows no interconnected carbon domains and features coarser hafnia crystallites ranging from ca. 100 nm near the interface to over 1000 nm in length further away from the interface.

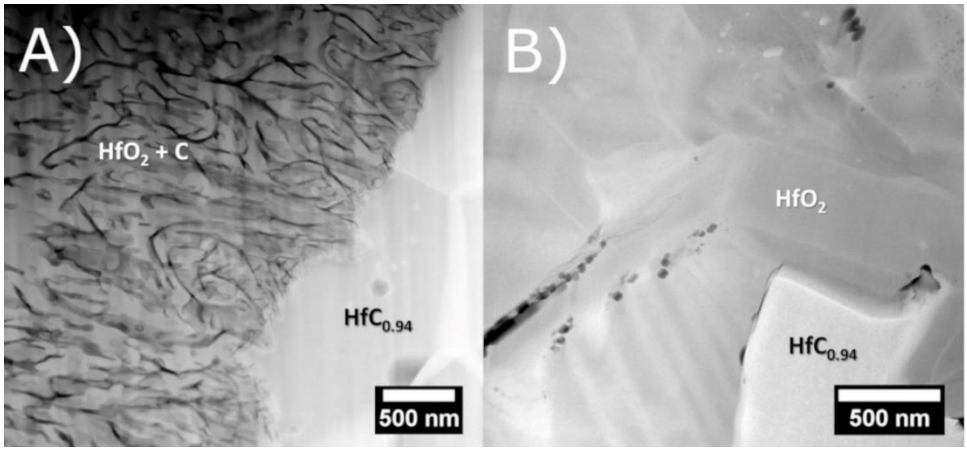

Figure 3: (A): STEM-HAADF image of the interface between the intermediate layer and the parent carbide material oxidized at 1668°C. (B): STEM-HAADF image of the interface between the oxide scale and parent carbide material oxidized at 1810°C. A stark difference in microstructure is observed, with much larger grains of HfO_2 forming upon the sample oxidized at higher temperatures.

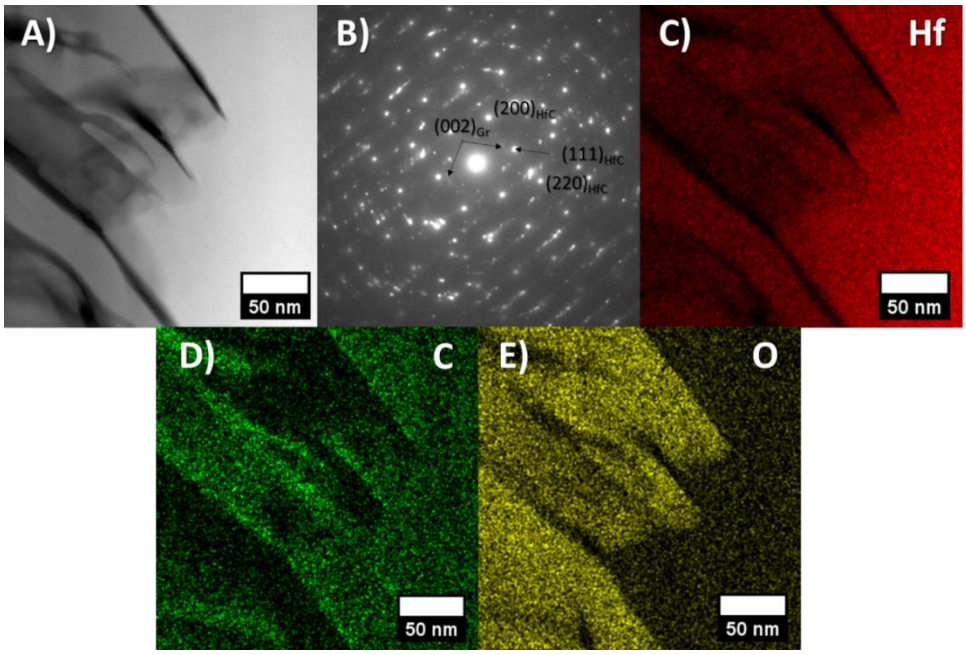

Figure 4: (A): STEM-HAADF image of the interface formed upon oxidation at 1668°C. Regular spacings and angles of the C domains are apparent and correspond to a near-epitaxy between the (111) HfC planes and the (002) graphite planes. Other near-epitaxial relationships can be observed between the HfC and HfO_2 diffraction spots. EDS maps showing the relative intensities and positions of Hf, C, and O atoms are shown in panels (C-E). Sharp interfaces are observed between all phases.

4. DISCUSSION

The stark differences in scale morphology observed on $HfC_{0.94}$ specimens oxidized above and below ca. 1800°C inform a mechanistic theory of the transition in kinetic regime from gaseous diffusion control through a nanometric pore network to solid-state diffusion control. Below ca. 1800°C, oxidation of parent carbide to form a carbon-containing interlayer comprising interspersed nanometric hafnia and carbon domains results in the formation of an interconnected nanometric pore network upon oxidative removal of carbon. Above ca. 1800°C, the direct oxidation of parent carbide to hafnia and gaseous products causes the absence of an interconnected pore network, leading to oxygen ingress by solid-state diffusion.

The regime transition can be rationalized based on phase equilibria considerations. A phase diagram useful to understanding $HfC_{0.94}$ oxidation can be constructed as a function of temperature and oxygen partial pressure, assuming a total pressure of 1 bar and using a ternary solution model for the oxygen-containing hafnium carbide phase HfC_xO_y.[16] For purposes of the present calculation, the maximum site occupancy for carbon on the anion sublattice (i.e., Hf(C,O,Va) where Va are vacancies) is limited to 0.94. The calculated phase diagram (Figure 5) reveals two important features. First, isopleths for oxygen in the HfC_xO_y phase stability regions (Figure 5A) illustrate how oxygen site occupancy increases with oxygen partial pressure. The solubility limit for oxygen in HfC_xO_y increases from ca. 5 at. % to 11 at. % as temperature increases from 1500°C to 2000°C. Second, there exists a maximum temperature above which carbon cannot co-exist with hafnia at any oxygen partial pressure (an invariant point at 1815°C and $\log_{10} pO_2 \approx -14.6$ for the carbon

stoichiometry corresponding to $HfC_{0.94}$). This calculated temperature is generally consistent with the observed regime transition. However, an invariant point is not conducive to the formation of a thick two-phase hafnia and carbon layer across which a gradient of oxygen potential might be expected to establish. Therefore, the maximum temperature at which carbon and hafnia co-existence is likely to be observable may be somewhat lower than the calculated invariant point. Arbitrarily taking a pO_2 window spanning one order of magnitude as an alternative metric for extended stability of a two-phase region arrives at a lower estimate of 1687°C for the onset of regime transition. Interestingly, the invariant point for regime transition increase as the maximum site occupancy for carbon in the HfC_xO_y decreases (Figure 6). Hafnium carbide may theoretically exhibit oxidation behavior consistent with the gaseous diffusion limited regime to temperatures as high as ca. 2070°C for fully substoichiometric compositions.

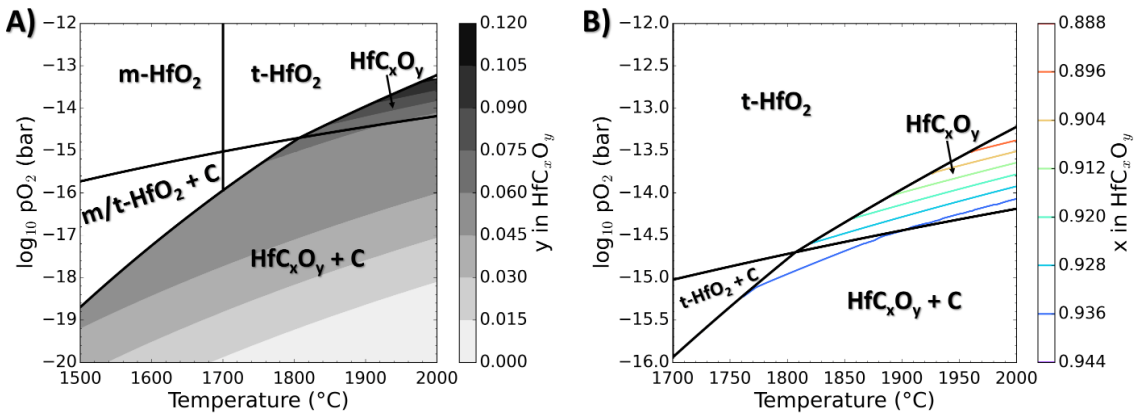

Figure 5: (A) $HfC_{0.94}$ phase diagram with oxygen isopleths in the HfC_xO_y phase stability regions shown as contour plot. (B) $HfC_{0.94}$ phase diagram with carbon isopleths in the HfC_xO_y phase stability regions shown as contour lines. Carbon site occupancy is saturated at 0.94 below the lowest contour line.

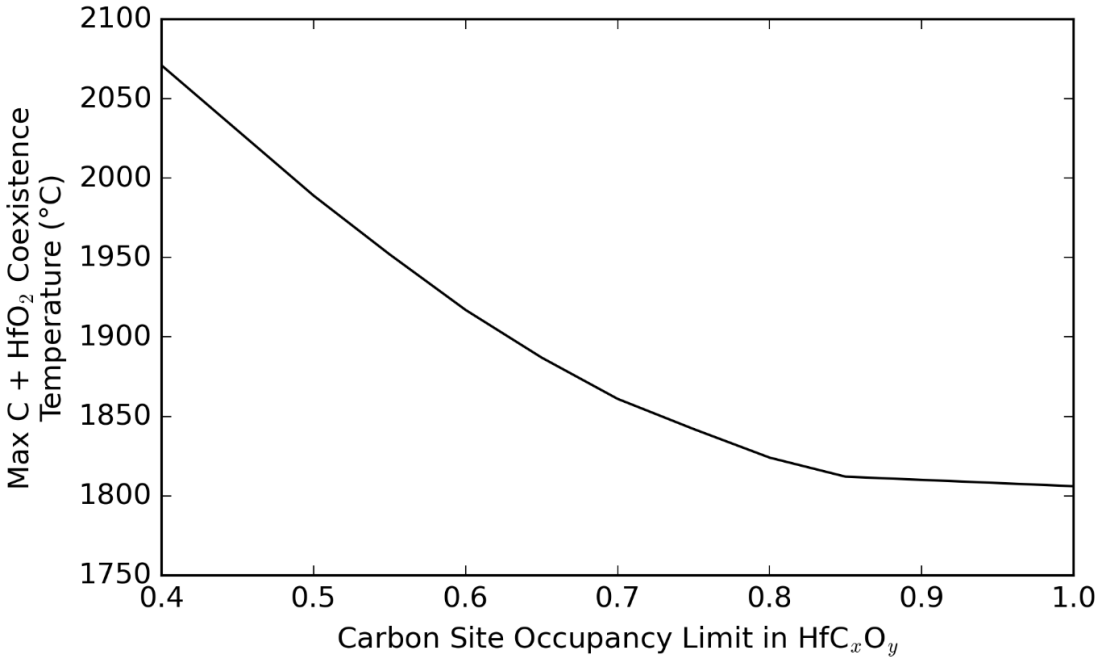

Figure 6: The effect of carbon stoichiometry in HfC_x on the calculated invariant temperature for carbon coexistence with hafnia. Lower temperature limit established by alternative metric corresponding to the temperature at which one order of magnitude pO_2 spans the two-phase hafnia and carbon stability field.

Literature data for oxidation of nominally stoichiometric hafnium carbide are shown in Figure 7, adapted from Courtright et al.[9] with superposed data and models augmented using currently available data.[8,17-19] The transition temperature estimates (i.e., the invariant temperature as upper limit and the order of magnitude pO_2 window for carbon and hafnia co-existence as alternative metric) for oxidation of $HfC_{0.94}$ are shown as vertical lines, which appear to be in reasonable agreement with observed regime transitions across multiple studies, supporting the mechanistic interpretations.

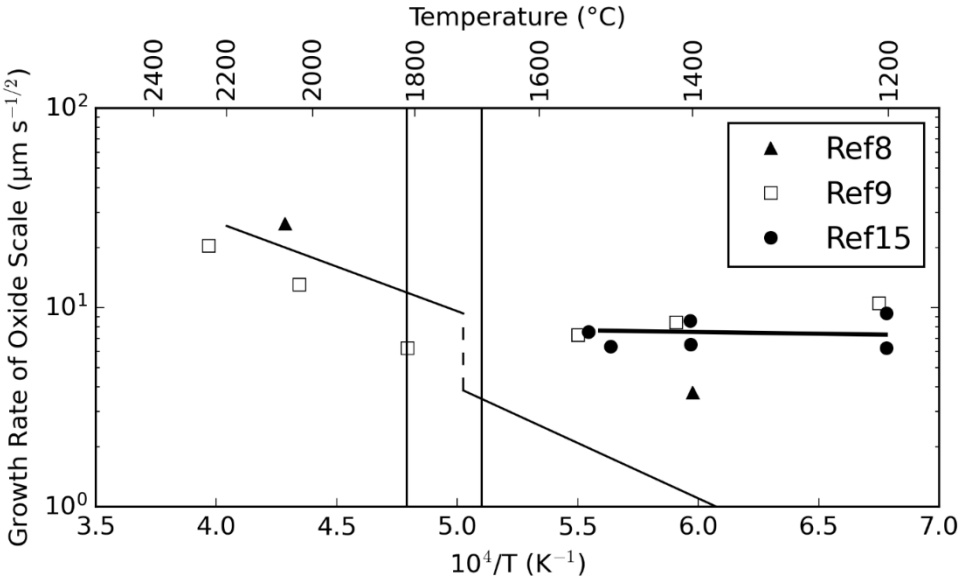

Figure 7: Summary of HfC oxidation data and models.[8,9,17-19] Vertical lines denote the maximum temperature for co-existence of carbon and hafnia assuming maximum carbon occupancy in HfC_x is limited to 0.94 and the temperature at which one order of magnitude pO_2 spans the co-existence domain, representing a range of temperatures over which regime transition is likely to be observable.

Literature reports of carbon-containing interlayers at experimental conditions exceeding the thermodynamic limit for coexistence of carbon with hafnia are inconsistent with current understanding of its formation.[10] A plausible and likely explanation is that experimental conditions reliant on surface temperature measurements may not accurately represent the temperature at the oxidation front. When the experimental heat balance establishes a significant through-thickness temperature gradient (e.g., due to the formation of a thermally insulative oxide scale and/or with significant backside heat removal), the temperature at the scale interface with the parent carbide may be sufficiently low to permit coexistence of hafnia and carbon, thereby enabling transition between oxidation regimes during testing despite surface temperatures exceeding theoretically predicted maximum transition temperatures.

5. CONCLUSIONS

Hafnium carbide ($HfC_{0.94}$) specimens were oxidized from 1668°C to 1810°C for 30 min. in 1% O_2 / 99% Argon flowing gas mixtures. Oxide scales formed below ca. 1800°C featured a carbon-containing interlayer comprising interspersed nanometric hafnia and carbon domains. Crystallite size and interlamellar spacing increased with temperature and with distance away from the parent carbide. Crystallographic orientation relationships indicate preferred growth directions relative to the orientation of parent carbide grains. Oxidation above ca. 1800°C resulted in oxide scales solely comprising porous hafnia absent carbon-containing interlayers. Thermodynamic analyses indicate the regime transition from gaseous to solid-state diffusion limited oxidation kinetics correlates with the maximum extent of the phase stability field with hafnia and carbon coexistence. Substoichiometric hafnium carbide exhibits an increased theoretical maximum temperature of carbon and hafnia co-existence up to 2070°C, providing a chemical mechanism by which the temperature-insensitive gaseous diffusion limited oxidation kinetic regime may be extended to higher service temperatures. However, maintaining the parent carbide interface at or below its oxidation regime transition temperature (e.g., by use of thermal barrier coatings and/or passive or active cooling technologies) may better prevent the onset of more rapid oxidation kinetics associated with direct transformation to hafnia and gaseous products, and may serve as a thermal design guideline for the use of hafnium carbide-containing structural materials in extreme environment applications.

ACKNOWLEDGEMENTS

This research is supported by, or in part by, the U.S. Office of Naval Research under award number N00014-17-1-2931 (Dr. Eric Marineau, program officer, and Dr. Eric Wuchina, technical advisor). The authors would like to acknowledge the assistance provided by the Missouri S&T Materials Research Center (MRC) and Advanced Materials Characterization Lab (AMCL) for use of facilities for Raman spectroscopy, and the University of Missouri Electron Microscopy Core for use of their electron microscopes. The authors would also like to acknowledge Nathaniel Inskip and Brian Bullock for their assistance with developing instrumentation and machining, as well as Brennan Long and Amelia Martinez for their assistance developing the optical furnace system.

REFERENCES

1. Cedillos-Barraza O, Manara D, Boboridis K, et al., "Investigating the highest melting temperature materials: A laser melting study of the TaC-HfC system," in *Sci. Rep.* **6**, pp. 1-11, 2016.
2. Bittermann H and Rogl P, "Critical assessment and thermodynamic calculation of the binary system hafnium-carbon (Hf-C)," in *J. Phase Equilib.* **18**, pp. 344-356, 1997.
3. Okamoto H, "The C-Hf (carbon-hafnium) system," in *Bull. Alloy Phase Diagrams* **11**, pp. 396-403, 1990.
4. Toth L, "Transition Metal Carbides and Nitrides," in *Refractory Materials Vol. 7*, Academic Press, 1971.
5. Wuchina EJ and Opeka M, "The Oxidation Behavior of HfC, HfN, and HfB_2," in *High Temperature Corrosion and Materials Chemistry III: Proc. Electrochem. Soc.*, pp. 136-143, 2001.

6. Shimada S, Yunazar F, Otani S, “Oxidation of hafnium carbide and titanium carbide single crystals with the formation of carbon at high temperatures and low oxygen pressures,” in *J. Am. Ceram. Soc.* **83**, pp.721-728, 2000.

7. Shimada S, Nakajima K, Inagaki M, “Oxidation of single crystals of hafnium carbide in a temperature range of 600° to 900°C,” in *J. Am. Ceram. Soc.* **80**, pp. 1749-1756, 1997.

8. Bargeron CB, Benson RC, Jette AN, et al., “Oxidation of hafnium carbide in the temperature range 1400 to 2060°C,” in *J. Am. Ceram. Soc.* **76**, pp.1040-1046, 1993.

9. Courtright EL, Prater JT, Holcomb GR, et al., “Oxidation of hafnium carbide and hafnium carbide with additions of tantalum and praseodymium,” in *Oxid. Met.* **36**, pp. 423-437, 1991.

10. Opeka MM, Talmy IG, Zaykoski JA, “Oxidation-based materials selection for 2000 C+ hypersonic aerosurfaces: Theoretical considerations and historical experience,” in *J. Mater. Sci.*, **39**, pp. 5887-5904, 2004.

11. Wang YL, Xiong X, Li GD, et al., “Ablation behavior of HfC protective coatings for carbon/carbon composites in an oxyacetylene combustion flame,” in *Corr. Sci.* **65**, pp. 549-555, 2012.

12. Kane KA, Pint BA, Mitchell D, et al., “Oxidation of ultrahigh temperature ceramics: kinetics, mechanisms, and applications,” in *J. Euro. Ceram. Soc.* **41**, pp. 6130-6150, 2021.

13. Wuchina EJ and Opeka M, “The group IV carbides and nitrides,” in *Ultra-High Temperature Ceramics: Materials for Extreme Environment Applications*, John Wiley & Sons, 2014.

14. Scott JA, He X, Lipke DW, “The role of microstructure on high-temperature oxidation behavior of hafnium carbide,” in *J. Am. Ceram. Soc.* **106**, pp. 3116-3126, 2023.

15. Holcomb GR and St. Pierre GR, “Application of a counter-current gaseous diffusion model to the oxidation of hafnium carbide at 1200 to 1530°C,” in *Oxid. Met.* **40**, pp. 109-118, 1993.

16. Réjasse F, Rapaud O, Trolliard G, et al., “Experimental investigation and thermodynamic evaluation of the C-Hf-O ternary system,” in *J. Am. Ceram. Soc.* **100**, pp. 3757-3770, 2017.

17. Pemsler JP, “Diffusion of Oxygen in Hafnium,” in *J. Electrochem. Soc.* **111**, pp. 1185-1186, 1964.

18. Carlson ON, Schmidt FA, Sever JC, “Electrotransport of Carbon, Nitrogen, and Oxygen in Hafnium Metal,” in *Metall. Trans.* **4**, pp. 2407-2411, 1973.

19. Kofstad P and Espevik S, “Kinetic study of high-temperature oxidation of hafnium,” *J. Less-Common Metals.* **12**, pp. 382-394, 1967.

III. ENTHALPIES OF FORMATION OF HAFNIUM CARBIDES AND NITRIDES BY COMBUSTION CALORIMETRY

In preparation for submission to Journal of Solid State Chemistry

Jonathan A. Scott, Amelia C. Martinez, David W. Lipke
Department of Materials Science and Engineering, Missouri University of Science and Technology, Rolla, MO, USA 65409

ABSTRACT

Oxygen bomb combustion calorimetry has been used to determine the standard enthalpy of combustion of hafnium carbide (HfC_{1-x}, x = 0.049 to 0.247) to be (-172.17x + 1291.9) kJ mol^{-1}. Combining with standard thermochemical data for the products of combustion yields estimates for the standard enthalpy of formation of hafnium carbide to be (261.45x – 257.95) kJ mol^{-1}. Combustion analysis of HfN_{1-y} yielded enthalpies of formation of -367 ± 17 (y = 0.0862) and -331 ± 13 (y = 0.146) kJ/mol, which agreed well with results from ab initio modelling.

1. INTRODUCTION

Extreme environment materials are needed to meet societal technological challenges for sustainable energy (e.g., more efficient turbines, nuclear reactors, etc.), national defense (e.g., hypersonic flight systems, high energy lasers), and space exploration applications[1-3]. Consequently, the discovery and design of functional materials that can withstand extreme temperatures, pressures, radiation fields and fluxes, and/or chemically reactive environments is a major field of research. High throughput computational methods are

increasingly being used to accelerate this process by generating *ab initio* databases and by using machine learning algorithms to help identify knowledge gaps to maximize utility of first principles calculations [4,5]. Despite these advances there remains a critical challenge pertaining to the integration of reliable experimental and computational data to create useful knowledge and make accurate predictions of previously unobserved materials behavior in extreme environments [6,7]. This problem is exacerbated by a longstanding dearth of experimental thermochemical data upon which databases for materials in extreme environments may be built.

For example, hafnium carbide (HfC_{1-x}) and hafnium nitride (HfN_{1-y}) are compounds with wide homogeneity ranges known to possess the highest melting points among binary carbides and nitrides, respectively [8]. Yet, while experimental thermochemical data is readily available for HfC_{1-x} [9-16], the same cannot be said for HfN_{1-y}. For example, direct calorimetric measurements to determine the standard enthalpy of formation of nominally stoichiometric HfN has only been reported in one work [17], while no experimental measurements have been reported for formation enthalpies of non-stoichiometric HfN_{1-y} that can verify *ab initio* predictions [18-21].

In this work, oxygen bomb combustion calorimetry is used to determine enthalpies of combustion for hafnium carbide (HfC_{1-x}, x = 0.049 to 0.247) and hafnium nitride (HfN_{1-y}, y = 0.086, 0.146). Standard thermochemical data for the products of combustion yields estimates for the standard enthalpy of formation by use of thermochemical cycles summarized in Table I.

Table 1: Thermochemical cycles for determination of enthalpies of formation from measured enthalpies of formation

Reaction	**Enthalpy values from [22]**
Enthalpy of formation from the elements at 25°C for HfC_{1-x}	
HfC_{1-x} (rocksalt, 25°C) + (2-x) O_2 (gas, 25°C) → HfO_2 (monoclinic, 25°C) + (1-x) CO_2 (gas, 25°C)	$\Delta H^0_{c,HfC_{1-x}}$ (combustion enthalpy)
Hf (solid, 25°C) + O_2 (gas, 25°C) → HfO_2 (monoclinic, 25°C)	$\Delta H_1 = -1144.77$ kJ/mol
C (graphite, 25°C) + O_2 (gas, 25°C) → CO_2 (gas, 25°C)	$\Delta H_2 = -393.50$ kJ/mol
Hf (solid, 25°C) + (1-x) C (graphite, 25°C) → HfC_{1-x} (rocksalt, 25°C)	$\Delta H^0_f = \Delta H_1 + (1-x)\Delta H_2 - \Delta H^0_{c,HfC_{1-x}}$
Enthalpy of formation from the elements at 25°C for HfN_{1-y}	
HfN_{1-y} (rocksalt, 25°C) + O_2 (gas, 25°C) → HfO_2 (monoclinic, 25°C) + (1-y)/2 N_2 (gas, 25°C)	$\Delta H^0_{c,HfN_{1-y}}$ (combustion enthalpy corrected for impurities)
Hf (solid, 25°C) + O_2 (gas, 25°C) → HfO_2 (monoclinic, 25°C)	$\Delta H_1 = -1144.77$ kJ/mol
Hf (solid, 25°C) + (1-y)/2 N_2 (gas, 25°C) → HfN_{1-y} (rocksalt, 25°C)	$\Delta H^0_f = \Delta H_1 - \Delta H^0_{c,HfN_{1-y}}$

2. MATERIALS AND METHODS

2.1. HAFNIUM CARBIDE SYNTHESIS

Hafnium carbide (HfC_{1-x}, x = 0.049 to 0.247) with varying stoichiometries were batched by ball milling $HfC_{0.94}$ (>99.9%, -325 mesh, H.C. Starck, Newton, MA) and HfH_2 (min. 95%,, max. d_{50} = 6.0 µm, Albemarle, Langelsheim, Germany) powders in acetone for four hours using yttria-stabilized zirconia milling media. Milled powders were dried on a rotary evaporator and passed through a 50-mesh sieve. Batched powders were loaded into a graphite die lined with boron nitride-coated graphite foil. The prepared die was placed

into a spark plasma sintering machine (SPS) (DCS10, Thermal Technology, Minden, NV), heated at 25°C/min to 900°C, and held for 15 minutes under vacuum to remove hydrogen generated by thermal decomposition of HfH_2. Then, the die was heated to 1750°C at 100°C/min whereupon the atmosphere was switched to flowing argon. After a 15 min. hold, a pressure of 32 MPa was applied and the die was held for 5 min. at 2100°C (x = 0.67, 0.84) or 2200°C (x = 0.94). After cooling and recovery from the die, graphite foil and powder flashing were removed manually and surface reaction layers were removed on a diamond surface grinder. Resultant billets were hammer milled until crushed powders could pass through a 200-mesh sieve. Magnetic iron impurities acquired through the milling process were removed using a neodymium magnet.

Powders were characterized using x-ray diffraction (XRD) with Cu-Kα radiation in a Bragg-Brentano geometry to identify crystalline phases. Rietveld refinement was used to determine lattice parameters and phase compositions. Elemental analysis was performed to determine the amount of C, N and O in the starting materials, as well as the final sintered materials using a LECO CS600 and LECO TN500 (LECO Corporation, St. Joseph, MI).

2.2. HAFNIUM NITRIDE SYNTHESIS

Hafnium nitride (HfN_{1-y}, y = 0.043 to 0.244) powders were generally prepared following the same procedures described for hafnium carbide powders, substituting HfN powder (99.5%, -325 mesh, 1.5 wt% Zr, Stanford Advanced Materials, Lake Forest, CA) for HfC powder. The composition with the highest nitrogen content (i.e. y = 0.043) was SPS consolidated at a peak temperature of 2200°C and 32 MPa applied pressure for 5

minutes whereas all other compositions were consolidated at a peak temperature of 2100°C.

The starting "HfN" powder contained two impurity phases: HfO_2 and an oxynitride phase indexed as $Hf_7O_8N_4$. Rietveld refinement indicated the phase composition of the starting "HfN" powder comprised 90.3 wt. % HfN_{1-y}, 7.9 wt. % HfO_2, and 1.8 wt. % $Hf_7O_8N_4$. Elemental analysis was performed on starting and SPS consolidated powders to measure C, N and O contents. The composition of HfN_{1-y} in the starting "HfN" powder was determined by the balance of nitrogen given by the difference of that measured by elemental analysis and the calculated proportion of nitrogen in $Hf_7O_8N_4$ phase as calculated by Rietveld refinement.

2.3. OXYGEN BOMB COMBUSTION CALORIMETRY

Oxygen bomb combustion calorimetry was performed on synthesized HfC_{1-x} and HfN_{1-y} powders in isoperibolic mode (C 200, IKA-Werke GmbH & Co. KG, Staufen, Germany). Gelatin capsules were used to hold 1 g of synthesized powders to control their combustion, and paraffin oil (LECO Certified Reference Material 502-901, Lot #1002) was added in varying amounts so as to obtain total heats of combustion matching benzoic acid calibration tablets. The prepared gelatin capsules were placed in stainless steel crucibles which were then loaded into a stainless steel bomb vessel after carefully ensuring that the capsule was secured atop a cotton ignition thread. Combustions were then performed following pressurization to 30 bar oxygen.

Extents of reaction were determined by comparing weight changes in combustion products to theoretical mass changes based on the phase compositions of starting materials,

and further verified by ensuring no additional mass changes upon subsequent oxidation heat treatments by thermogravimetric analysis. The following reaction was assumed to be occurring for HfC_{1-x} powders:

$$HfC_{1-x} + (1-x)\,O_2 \rightarrow HfO_2 + (1-x)\,CO_2 \quad (1)$$

while the following reactions were assumed to be occurring for HfN_{1-y} powders:

$$HfN_{1-y} + O_2 \rightarrow HfO_2 + \frac{1-y}{2} N_2 \quad (2)$$

$$Hf_7O_8N_4 + 3O_2 \rightarrow 7HfO_2 + 2N_2 \quad (3)$$

For both types of powders, the effect of dissolved impurities (i.e., [O], [N], [S]) were neglected in the calculation of formation enthalpies. It was further assumed that the overall sulfur content was sufficiently low that the contribution of SO_x formation could be ignored. For HfN_{1-y} powders, it was also assumed that heats associated with formation of HNO_2 and HNO_3 species could be neglected, as Humphrey in [17] showed for combustion of 5g HfN powder that their contribution accounted for only ~1.4 J/mol HfN, and the tested amounts in this work were all less than 1g. Corrections to the data for the impurity of $Hf_7O_8N_4$ phase were performed using predicted enthalpy of formation values [23], and corrections for conversion to a constant pressure process and to unit fugacity of gas species were manually calculated (see Supplemental Materials for more information on data reduction procedures).

3. RESULTS AND DISCUSSION

X-ray diffraction (XRD) of synthesized HfC_{1-x} powders indicated a single phase material with FCC rocksalt structure (Figure). Measured lattice parameters decreased linearly with carbon content from 4.639Å at x = 0.049 to 4.617Å at x = 0.247. XRD of synthesized HfN_{1-y} powders shows the major peaks in each pattern were all attributed to an FCC rocksalt-type structure (Figure 2). Minor peaks attributed to impurity phases HfO_2 and Hf_2ON_2 were also observed. Rietveld refinement of each powder diffraction scan resulted in phase compositions summarized in Table 2. No clear trend in lattice parameter versus anion site occupancy in synthesized hafnium nitride powders was observed.

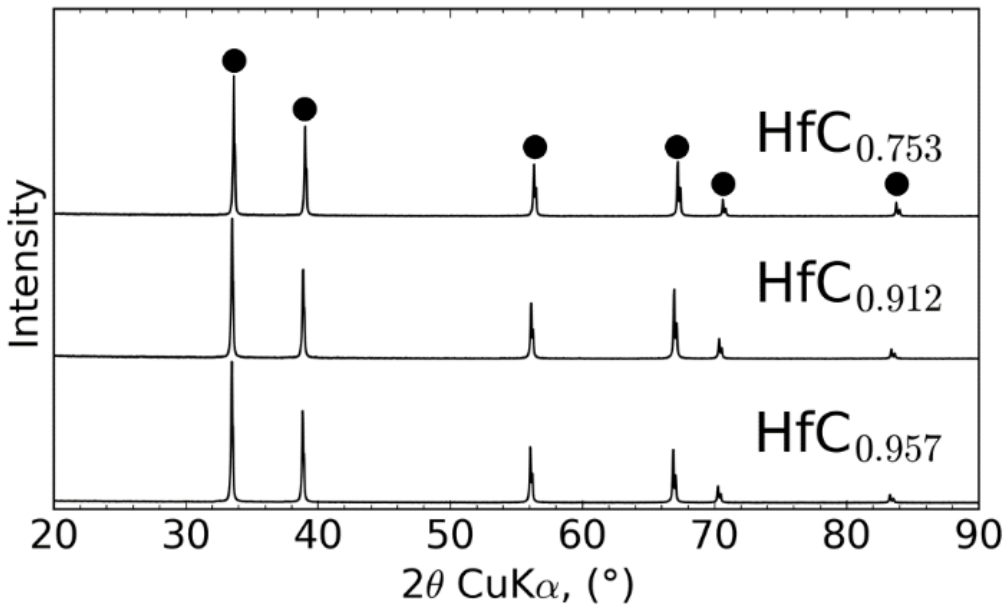

Figure 1: XRD of synthesized HfC_{1-x} powders. No secondary phases were detected. Black circles indicate rocksalt cubic HfC_{1-x}.

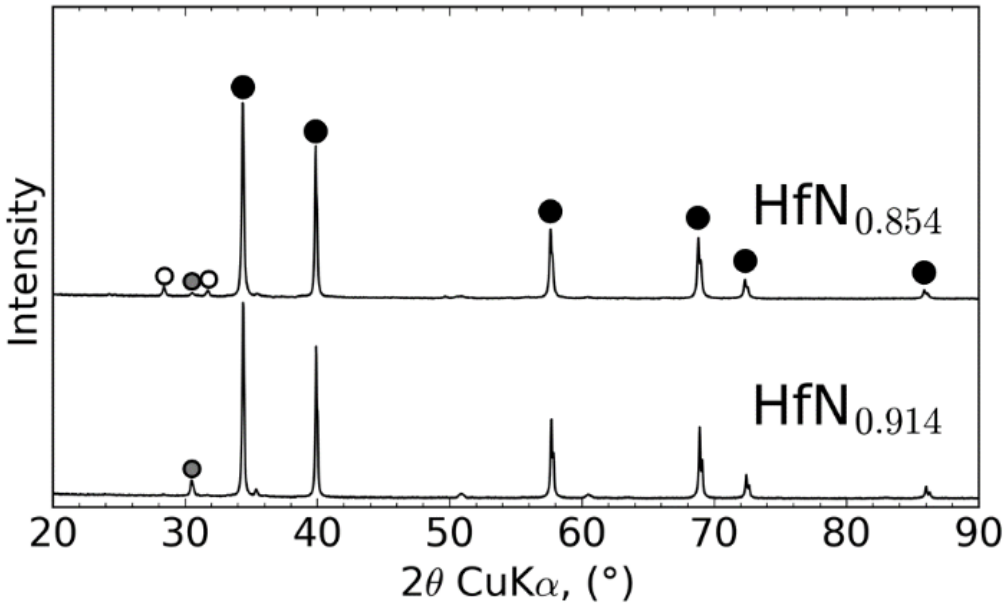

Figure 2: XRD patterns of synthesized HfN_{1-y} powders. Black circles indicate HfN_{1-y}, white circles indicate m-HfO_2 and grey circles indicate $Hf_7O_8N_4$.

Table 2: Phase composition of synthesized HfN_{1-y} powders.

Powder	**HfN_{1-y} (wt%)**	**$Hf_7O_8N_4$ (wt%)**	**HfO_2 (wt%)**	**Total O (wt%)**	**Lattice Parameter a_0 (Å)**
$HfN_{0.914}$	88.7	11.3	0	1.56	4.518
$HfN_{0.854}$	83.9	13	3.1	2.01	4.524

3.1. COMBUSTION CALORIMETRY OF HAFNIUM CARBIDES

Table 3 summarizes combustion data for hafnium carbides of varying composition. Enthalpies of formation calculated from corrected enthalpies of combustion are plotted in Figure 3 in comparison to values reported in literature. Enthalpies of formation for the same

reported carbon content vary by as much as 40 kJ/mol. Such differences are likely attributable to varying elemental and phase compositional purities of the starting materials. The $HfC_{0.951}$ powder showed good agreement with reported values for HfC in thermochemical tables (-245.46 vs. -251.04 kJ/mol for HfC [22]). The observed trend with composition is in close agreement with the results of Fesenko et al [13]. A trendline fit provides the following estimated enthalpy of formation as a function of composition: $\Delta H^0_{f,HfC_{1-x}} = Ax + B$ [261.45x – 257.95].

Major sources of error in combustion enthalpies of the HfC_{1-x} samples are due to variability in measured enthalpies of combustion. The measured ΔE_c values for these compositions possessed a standard deviation of 64 J/g. This error accounts for roughly 75% of the overall error in the measurements. Minor sources of error in combustion enthalpies are attributable to variations in overall composition and dissolved impurity atoms (O/N/S). For example, $HfC_{0.75}$ samples in this study exhibited N contents ranging from 0.152-0.471 wt. % despite having narrow compositional ranges for C and O (i.e., $HfC_{0.75}O_{0.06}N_{0.02\text{-}0.06}$). Small differences in compositional homogeneity (any anion) between test samples can manifest as modest changes in the measured heats of combustion (>2 kJ) as a result of differences in the critical solubility of oxygen required to initiate formation of HfO_2 during the combustion process [24-26].

Table 3: Summary of experimental results for combustion calorimetry of HfC_x powders.

x in HfC_{1-x}	m_0 (g)	m_f (g)	Q_{Ext} total (kJ)	ΔE_c (J/g)	Δm (%)	α	ΔH_c (J/g)	ΔH_c^0 (kJ/mol)	ΔH_f^0 (kJ/mol)	EoR corr. (kJ/mol)	Error (kJ/mol)
0.043	1.032	1.138	24.507	6780	10.27	0.95	6712	1290	-233	-245	4
0.043	1.017	1.124	23.507	6743	10.52	0.97	6676	1280	-240	-246	4
0.043	1.033	1.139	23.323	6776	10.26	0.95	6708	1290	-233	-246	4
0.088	1.019	1.127	23.825	6685	10.60	0.95	6621	1270	-237	-248	5
0.088	1.010	1.12	24.438	6815	10.89	0.98	6750	1290	-212	-216	4
0.088	1.009	1.119	24.507	6761	10.90	0.98	6697	1280	-222	-227	4
0.088	1.009	1.115	23.507	6634	10.51	0.95	6571	1260	-246	-261	5
0.088	1.007	1.119	23.323	6678	11.12	1.00	6614	1270	-238	-239	4
0.247	1.006	1.132	29.616	6756	12.52	1.02	6702	1270	-174	-170	4
0.247	1.001	1.121	30.408	6618	11.99	0.98	6565	1240	-200	-204	5
0.247	1.001	1.121	30.492	6706	11.99	0.98	6653	1260	-183	-187	5
0.247	0.997	1.12	30.76	6725	12.34	1.01	6671	1260	-180	-178	4
0.247	1.004	1.126	30.012	6487	12.15	0.99	6435	1220	-224	-226	5

(m_0: total mass of powder before combustion
m_f: final mass of combusted material
Q_{Ext} total: total energy contributed by combustion aids
ΔE_c: Heat of combustion of HfC_{1-x}
Δm: Change in mass of the overall reaction
α: Extent of reaction
ΔH_c: Enthalpy of combustion of the powder
ΔH_c^0: Standard state enthalpy of combustion of the powder
ΔH_f^0: Standard state enthalpy of formation of the powder
EoR Corr: Standard state enthalpy of formation of the powder corrected to the extent of reaction
Error: Error in the analysis propagated from systematic analysis of sources of error.)

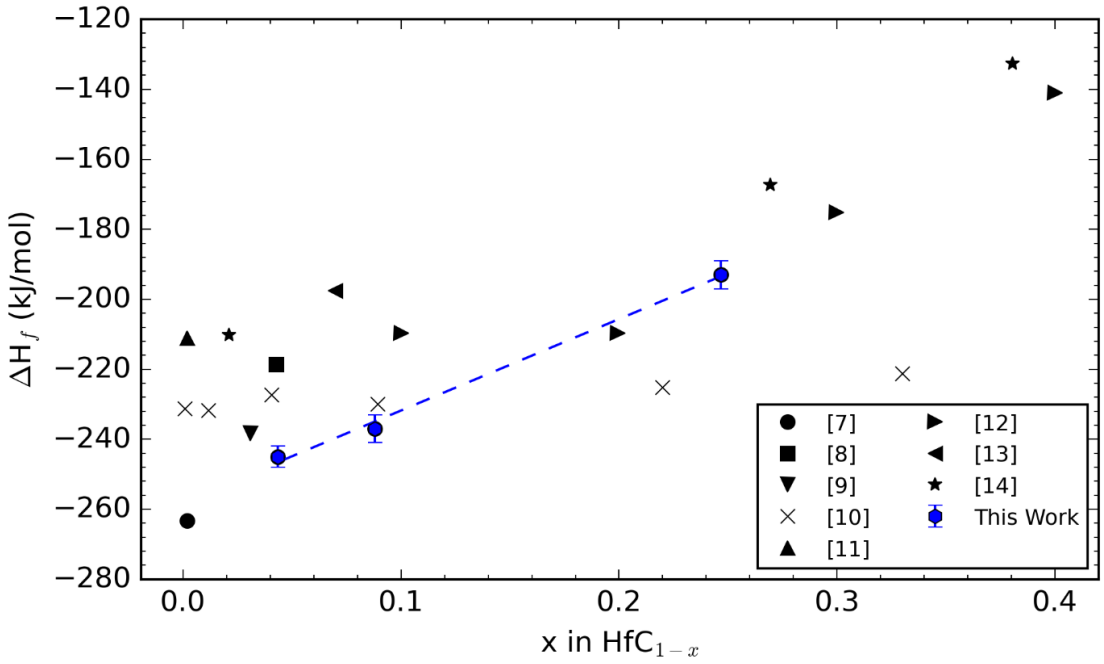

Figure 3: Enthalpies of formation for hafnium carbide as a function of carbon content compared to selected experimental values reported in literature.

3.2. COMBUSTION CALORIMETRY OF HAFNIUM NITRIDES

Table 4 summarizes combustion data for hafnium nitrides of varying composition. Enthalpies of formation calculated from corrected enthalpies of combustion are plotted in Figure 4 in comparison to theoretical predictions reported in literature. Enthalpies of formation were calculated as -367 ± 17 (y = 0.0862) and -331 ± 13 (y = 0.146) for HfN_{1-y}. Generally good agreement is shown between theoretical *ab initio* predictions and the experimental data presented. Discrepancies between the models and experimental values could be due to standard state corrections, as the enthalpies presented in this work are corrected to 298.15K, 1 bar, while the reported theoretical enthalpies of formation are calculated at 0K.

Major sources of error in combustion enthalpies for hafnium nitrides are attributable to uncertainties in the amounts of impurity phases, and uncertainties in the enthalpies of formation of the impurity phases. A major impurity in both the starting powder and sintered compositions is $Hf_7O_8N_4$, which has no reported experimental enthalpies of formation in the literature, only density functional theory calculations for the material at 0K [23]. Estimates for the uncertainty in the heat of combustion of this impurity, alongside uncertainty in the composition of the test material dominates the error in the measurement. The second major source of error in the measurement is from the variability in the heat of combustion, controlled primarily by the uncertainty in heat equivalents of the bomb calorimeter.

A source of possible systematic error not explicitly accounted for in the present analyses comes from neglecting the contribution of surface energy of nanocrystalline HfO_2 that may be present in combustion products. An estimate for this surface energy of 3.7 J/m^2 could affect the measured heat content by as much as -20 kJ/mol [7,18]. Consequently, the accuracy of reported formation enthalpies in this work and in other experimental works should not be overestimated, and discrepancies with *ab initio* predictions on this order of magnitude can be expected.

Table 4: Summary of experimental results for combustion calorimetry of HfN_{1-y} powders.

y in HfN_{1-y}	m_0 (g)	m_f (g)	Q_{Ext} total	ΔE_c (J/g)	Δm (%)	α	ΔH_c (J/g)	ΔH_c^0 (kJ/mol)	ΔH_f^0 (kJ/mol)	EoR corr. (kJ/mol)	Error (kJ/mol)
0.086	1.001	1.081	26.099	3975	8.65	0.939	4352	835	-310	-346	17
0.086	1.005	1.087	25.583	3829	8.84	0.959	4189	804	-341	-372	18
0.086	1.004	1.085	26.181	3838	8.74	0.948	4200	806	-339	-375	18
0.086	1.001	1.084	25.453	3948	8.99	0.976	4322	829	-316	-339	16
0.086	1.000	1.085	26.153	3864	9.23	1.001	4230	811	-333	-349	18
0.1455	1.010	1.096	26.958	3838	9.72	1.031	4212	802	-343	-286	13
0.1455	1.005	1.094	25.923	3767	10.12	1.074	4130	787	-358	-290	13
0.1455	1.005	1.09	26.422	3864	9.65	1.024	4245	809	-336	-282	13

See Table 3 for abbreviations.

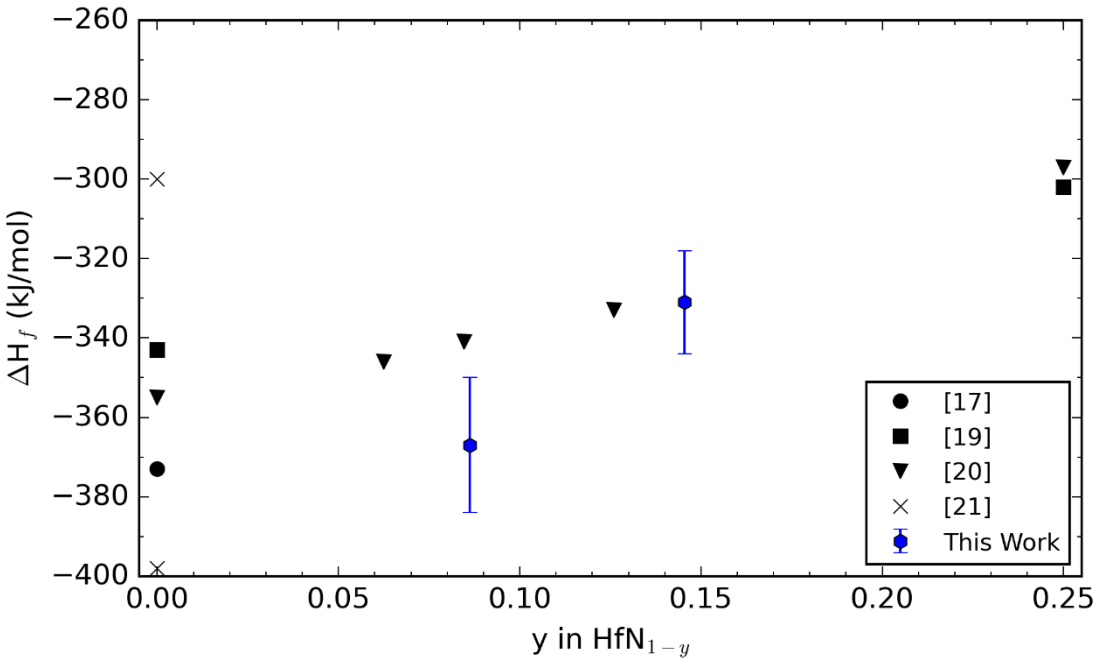

Figure 4: Enthalpies of formation for hafnium nitride as a function of nitrogen content compared to selected and experimental values reported in literature.

4. CONCLUSIONS

Substoichoimetric hafnium carbides and hafnium nitrides were synthesized via spark-plasma sintering of mixtures of hafnium hydride with nominally stoichiometric hafnium carbide and hafnium nitride powders, respectively. While synthesized carbides were determined to be phase pure, synthesized nitrides contained impurity phases originating from the starting hafnium nitride powder. Some decomposition of the impurity oxide and oxynitride phases were observed during sintering, though they remained in the final product. Enthalpies of combustion were determined by oxygen bomb calorimetry. After correcting for impurities, the use of standard thermochemical data for combustion products enabled determination of enthalpies of formation. Measured enthalpies of formation for hafnium carbide (HfC_{1-x}, x = 0.049 to 0.247) were in reasonable agreement with prior experimental values, with a compositional dependence given by (261.45x – 257.95) kJ mol^{-1}. This work presents the first reported determination of formation enthalpies for substoichiometric hafnium nitrides; therefore, comparisons can only be made to computational predictions. Calculated enthalpies of formation -367 ± 17 (y = 0.0862) and -331 ± 13 (y = 0.146) kJ/mol for HfN_{1-y} agreed well with *ab initio* predictions. Assessment of experimental errors indicates that major contributions include uncertainties in the amounts of impurity phases, and error from the heat equivalent of the calorimeter. More accurate determinations will require specialized preparation of high purity samples, and a more complete accounting of sources of systematic error neglected in this treatment. The authors hope these experimentally determined formation enthalpies for hafnium nitrides will be of use to researchers interested in the behavior of Hf-N based systems.

ACKNOWLEDGEMENTS

This material is based upon research supported by, or in part by, the U. S. Office of Naval Research under award number N00014-17-1-2931 (Dr. Eric Marineau, program officer, and Dr. Eric Wuchina, technical advisor). The authors gratefully acknowledge the Missouri S&T Materials Research Center (MRC) and Advanced Materials Characterization Lab (AMCL) for use of facilities, Erica Pizzo for assistance with HfN_{1-y} sample preparation and Dr. Eric Bohannon for assistance with Rietveld refinement of XRD patterns.

REFERENCES

1. Eswarappa Prameela S, Pollock TM, et al., “Materials for extreme environments,” in *Nature Reviews Materials* **8**, pp. 81-88, 2023.

2. Wyatt BC, Nemani SK, Hilmas GE, et al., “Ultra-high temperature ceramics for extreme environments,” in *Nature Reviews* Materials, pp. 1-7, 2023.

3. Hemley RJ, Crabtree GW, Buchanan MV, “Materials in extreme environments,” in *Physics today* **62**, pp. 32-37, 2009.

4. de Pablo JJ, Jackson NE, Webb MA, et al., “New frontiers for the materials genome initiative,” in *npj Computational Materials*. **5**, pp. 1-23, 2019.

5. Maruyama B, Hattrick-Simpers J, Musinski W, et al., “Artificial intelligence for materials research at extremes,” *MRS Bulletin.* **47**, pp. 1154-1164, 2022.

6. Ågren J, “CALPHAD and the materials genome. A 10 year anniversary,” in *Calphad.* **80**, pp. 1-6, 2023.

7. Ushakov SV and Navrotsky A, “Experimental approaches to the thermodynamics of ceramics above 1500°C,” in *J. Am. Ceram. Soc*. **95**, pp. 1463-1482, 2012.

8. Fleischer RL, “High-temperature, high-strength materials—an overview,” in *JOM.* **37**, pp. 16-20, 1985.

9. Coffman, JA, Kibler, GM, Lyon, TF, et al., “Carbonization of Plastics and Refractories Materials Research,” in *Technical Report WADD-TR-60-646, Part II*, Air Force Materials Laboratory, 1963.

10. Mah AD, “Heats of formation of zirconium carbide and hafnium carbide,” in *U.S. Bureau of Mines Report 6518*, 1964.

11. McClaine LA and Little AD, “Thermodynamic and Kinetic Studies for a Refractory Materials Program,” in *Technical Report ASD-TDR-62-204 Part III.*, Air Force Materials Laboratory, 1964

12. Zehlankin VI and Kutsev VS, “Variation of the Heat of Formation of Hafnium Carbides with Composition,” in *Russ. J. Phys. Chem.* **38**, pp. 302-303, 1964.

13. Fesenko VV, Bolgar AS, Gordienko SP, “Vaporization rate, vapor pressure, composition discontinuity, and some thermodynamic properties of refractory compounds at temperatures up to 3000°C,” in *Rev Hautes Tempér Réfract.* **3**, pp. 261-271, 1966.

14. Kornilov AN, “Enthalpies of Formation of Hafnium Carbides,” in *J. Chem. Thermodyn.* **9**, pp. 629-642, 1977.

15. Maslov VM, Neganov AS, Borvinskaya IP, et al., “Self-propagating high-temperature synthesis as a method for determination of the heat of formation of refractory compounds,” in *Fiz, Goreniya Vzryva.* **14**, pp. 73-82, 1978.

16. Berkane R, “Thermodynamic study of chromium, titanium, zirconium and hafnium carbides by high temperature calorimetry numerical modeling of the phase diagram,” Thesis, Université de Nancy I, 1989.

17. Humphrey GL, “Heats of Formation of Hafnium Oxide and Hafnium Nitride,” in *J Am Chem Soc*. **75**, pp. 2806-2807, 1953.

18. Ushakov SV, Navrotsky A, Hong QJ, et al., “Carbides and nitrides of zirconium and hafnium,” in *Materials.* **12**, pp. 1-23, 2019.

19. Weinberger CR, Yu XX, Yu H, et al., “Ab initio investigations of the phase stability in group IVB and VB transition metal nitrides,” in *Computational Materials Science.* **138**, pp. 333-345, 2017.

20. Ashley NJ, Parfitt D, Chroneos A, et al., “Mechanisms of nonstoichiometry in HfN_{1-x},” in *Journal of Applied Physics.* **106**, pp. 1-4, 2009.

21. Zhao E and Wu Z, “Electronic and mechanical properties of 5d transition metal mononitrides via first principles,” in *Journal of Solid State Chemistry*. **181**, pp. 2814-2827, 2008.

22. I. Barin, “Thermochemical Data of Pure Substances,” VCH Verlagsgesellschaft, 1999.

23. Bharat T, Patterson RJ, Conibeer G, et al., “Investigating electronic, optical, and phononic properties of bulk γ-M2ON2 and β-M7O8N4 (M = Hf and Zr) insulators using density functional theory,” in *Am. Chem. Soc. Omega.* 7, pp. 9196-9205, 2022.

24. Réjasse F, Rapaud O, Trolliard G, et al., “Experimental investigation and thermodynamic evaluation of the C–Hf–O ternary system,” in *J. Am. Ceram. Soc.* **100**, pp. 3757-3770, 2017.

25. Réjasse F, Trolliard G, Rapaud O, et al., “TEM study of the reaction mechanisms involved in the carbothermal reduction of hafnia,” in *RSC Adv.* **5**, pp. 45341-45350, 2015.

26. Constant K, Kieffer R, Ettmayer P, “Über das pseudoternäre System “HfO”-HfN-HfC,” in *Monatshefte für Chemie.* **106**, pp. 973-981, 1975.

APPENDIX

EXPLANATION OF ERROR ANALYSIS

Uncertainty analysis was performed on the measured enthalpies of combustion to assess reasonable estimates of formation enthalpies of hafnium carbides and nitrides. The uncertainty estimates for mass measurements were based on the precision of the instrument, alongside ESD's determined via Rietveld refinement. For uncertainty in m_0, the estimated uncertainty also included correction for the actual mass of HfN_x powder versus the non-reacting HfO_2 present in the powder. Estimates of uncertainty for the heat determination of the calorimeter itself was determined by assessing the precision of the temperature measurement, the combined uncertainty of all of the combustion aids used, and the standard deviation of the energy equivalents of the calorimeter vessel (C), determined via calibration. The measured powder heat was corrected by removing the heat contributed by the combustion of a side product, Hf_2ON_2, which was present in the powder. The uncertainty in the enthalpy of formation of Hf_2ON_2 was estimated as 10 kJ/mol, as the enthalpy of formation used for the calculations was the enthalpy of formation as determined by density functional theory (DFT) at 0K. This was thought to capture the extrapolation of the heat of formation to standard state temperatures. In order to calculate a close approximation of the amounts of gaseous species present during the test, the amount of oxygen consumed was calculated, taking fugacity corrections into account, according to the complete reaction of all materials present in the trial. The final assessed amounts of gaseous species present were used to determine the heat content contributed by the

compressibility of each of the gases present. Water vapor was not included within the assessment. The heat calculated at this stage was then converted to an enthalpy of reaction using Hess' Law, which was used with the tabulated value of the enthalpy of formation of HfO_2 to determine the enthalpy of formation of HfN_x (or HfC_x). This was corrected to the extent of reaction of the powder, assuming a nominal stoichiometry of the powder sample consistent with that of the bulk material (i.e., no dramatic differences between powder samples within the same material batch). Error analysis for the HfC_x materials followed the same process; however, since there was no impurity phase detected within the starting materials, the analysis did not include compensation for heat additions of impurities. No analysis of the metals content was performed, thus, no correction to the heat content was made to account for the presence of zirconium. For the HfN_x series of materials, the primary error was associated with the uncertainty in the heat of formation of the Hf_2ON_2 impurity material, as this contributed approximately 4% total error to the measurement. For the HfC_x measurements, the primary error was associated with the variance in measurements, which contributed approximately 1% total error to the measurement.

2. INDIVIDUAL EQUATIONS FOR ERROR PROPAGATION

$$\Delta E_{C,HfN_{1-y}} = \Delta E_{C,raw}(m_o) - \Delta E_{C,Hf_7O_8N_4}\left(m_{Hf_7O_8N_4}\right) - (\Delta nRT)|_{Hf_7O_8N_4} \quad (1)$$

$$\delta\Delta E_{c,raw} = \sqrt{\left(\frac{\partial m_0}{m_0}\right)^2 + \left(\frac{\partial C}{C}\right)^2 + \left(\frac{\partial \Delta T}{\Delta T}\right)^2 + \left(\frac{\partial (CI)}{CI}\right)^2} \quad (2)$$

$$\delta\Delta E_{c,HfN_{1-y}} =$$

$$\sqrt{\left(\frac{\delta\Delta E_{c,raw}}{\Delta E_{c,raw}}\right)^2 + \left(\frac{\delta m_0}{m_0}\right)^2 + \left(\frac{\delta\Delta E_{c,Hf_7O_8N_4}}{\Delta E_{c,Hf_7O_8N_4}}\right)^2 + \left(\frac{\delta m_{Hf_7O_8N_4}}{m_{Hf_7O_8N_4}}\right)^2 + \left(\frac{\delta\Delta n_{Hf_7O_8N_4}}{\Delta n_{Hf_7O_8N_4}}\right)^2 + \left(\frac{\delta R}{R}\right)^2 + \left(\frac{\delta T}{T}\right)^2}$$

(3)

$$\Delta H^o_{C,HfN_{1-y}} = \Delta E_{C,HfN_{1-y}} + \Delta nRT + \sum_{i=1}^{k} n_i \frac{\delta U}{\delta P}|_i \Delta P \quad (4)$$

$$\delta\Delta H^o_{c,HfN_{1-y}} =$$

$$\sqrt{\begin{aligned}&\delta\Delta E_{c,HfN_{1-y}}{}^2 + \left(\frac{\delta\Delta n}{\Delta n}\right)^2 + \left(\frac{\delta R}{R}\right)^2 + \left(\frac{\delta T}{T}\right)^2 + \left(\frac{\delta n_{N_2}}{n_{N_2}}\right)^2 + \left(\frac{\delta\left(\frac{\delta U}{\delta P_{N_2}}\right)}{\frac{\delta U}{\delta P_{N_2}}}\right)^2 + \left(\frac{\delta\Delta P}{\Delta P}\right)^2 \\ &+ \left(\frac{\delta n_{O_2}}{n_{O_2}}\right)^2 + \left(\frac{\delta\left(\frac{\delta U}{\delta P_{O_2}}\right)}{\frac{\delta U}{\delta P_{O_2}}}\right)^2 + \left(\frac{\delta\Delta P}{\Delta P}\right)^2 \\ &+ \left(\frac{\delta n_{CO_2}}{n_{CO_2}}\right)^2 + \left(\frac{\delta\left(\frac{\delta U}{\delta P_{CO_2}}\right)}{\frac{\delta U}{\delta P_{CO_2}}}\right)^2 + \left(\frac{\delta\Delta P}{\Delta P}\right)^2\end{aligned}} \quad (5)$$

$$\Delta H^o_{f,HfN_{1-y}} = \frac{1}{\alpha}\left(\Delta H^o_{C,HfN_{1-y}} - \Delta H^o_{f,HfO_2}\right) \quad (6)$$

$$\delta\left(\Delta H^o_{C,HfN_{1-y}} - \Delta H^o_{f,HfO_2}\right) = \sqrt{\left(\frac{\delta\Delta H^o_{c,HfN_x}}{\Delta H^o_{c,HfN_x}}\right)^2 + \left(\frac{\delta\Delta H^o_{f,HfO_2}}{\Delta H^o_{f,HfO_2}}\right)^2} \quad (7)$$

$$\delta\Delta H^o_{f,HfN_{1-y}} = \frac{1}{\alpha}\left(\Delta H^o_{C,HfN_{1-y}} - \Delta H^o_{f,HfO_2}\right)\sqrt{\left(\frac{\delta\alpha}{\alpha}\right)^2 + \left(\frac{\delta\left(\Delta H^o_{C,HfN_{1-y}} - \Delta H^o_{f,HfO_2}\right)}{\Delta H^o_{C,HfN_{1-y}} - \Delta H^o_{f,HfO_2}}\right)^2} \quad (8)$$

"δ" at the beginning of a term indicates error with respect to that quantity

$\Delta E_{c,HfN1-y}$ = Combustion reaction energy for HfN_{1-y}
$\Delta E_{c,raw}$ = Combustion energy output by isoperibol bomb calorimeter
m_0 = mass of starting powder
C = energy equivalent of the calorimeter system, J/K
ΔT = Temperature rise of the calorimeter
CI = Calculated 95% confidence interval of measured heats of combustion
$m_{Hf7O8N4}$ = mass of $Hf_7O_8N_4$ in initial powder as determined via Rietveld Refinement
$\Delta E_{c,\ Hf7O8N4}$= Combustion energy for $Hf_7O_8N_4$
Δn = change in moles of gaseous species for given reaction
R = 8.314 J/molK, universal gas constant
T = 298.15K, standard state temperature
$\Delta H^o_{C,HfN_{1-y}}$= Enthalpy of combustion of HfN_{1-y} at standard state
n_i = number of moles of gaseous species, i, present post reaction (calculated quantity based off of theoretical reaction and combustion aid side reactions)
$\frac{\delta U}{\delta P}|_i$= Tabulated isothermal compressibility constants for a given gaseous species
ΔP = Pressure difference between test pressure and standard state
$\Delta H^o_{f,HfN_{1-y}}$= Enthalpy of formation of HfN_{1-y} at standard state
α = extent of reaction (calculated percent mass change over theoretical percent mass change)
$\Delta H^o_{f,HfO_2}$= Enthalpy of formation of HfO_2 at standard state

$$\Delta H^o_{f,HfN_{1-y}} = \frac{1}{\alpha}\left[\begin{array}{c}\frac{m_0 C \Delta T}{m_0} - \Delta E_{c,Hf_7O_8N_4} m_{Hf_7O_8N_4} - \Delta nRT|_{Hf_7O_8N_4} + \Delta nRT|_{HfN_{1-y}} \\ +n_{N_2}\frac{\delta U}{\delta P}|_{N_2}\Delta P + n_{O_2}\frac{\delta U}{\delta P}|_{O_2}\Delta P + n_{CO_2}\frac{\delta U}{\delta P}|_{CO_2}\Delta P + n_{H_2O}\frac{\delta U}{\delta P}|_{H_2O}\Delta P\end{array}\right] \quad (9)$$

3. ASSUMPTIONS

1. Measured-mass errors are equal to the precision of the instrument.

2. Universal constants and conversions to standard state have zero error.

3. Tabulated isothermal compressibility data values have no error reported, and thus error is in the last digit.

4. Uncertainty in pressure is small, so uncertainty in ΔP is negligible (can be assumed to be a constant value)

5. Uncertainties for calibration values and instrumental parameters are equal to the calibration value dataset 95% confidence interval added in quadrature with the precision of the instrument's measurement (e.g., temperature rise uncertainty is equal to the last digit of precision) (uncertainty in energy equivalent is equal to σ_C)

SECTION

3. SUMMARY AND CONCLUSIONS

3.1. SUMMARY

The first paper in this dissertation sought to elucidate the effect of oxide scale micro-/nanostructure on the oxidation behavior reported in the literature through observations of the oxide scale using electron microscopy and Raman spectroscopy. To accomplish this, HfC_x (x = 0.67, 0.84, 0.94) specimens were oxidized at 1300°C for 4 hours under 0.8 mbar O_2. On oxidized $HfC_{0.94}$ samples, it was observed that the formation of an initially amorphous "HfO_2C_x" material immediately adjacent to grains of parent carbide subsequently decomposed into a two-phase mixture of nanocrystalline HfO_2 + disordered C. Moving away from the oxide scale/carbide interface, the two-phase mixture coarsened in size until oxidation of the C present in the two-phase mixture occurred. This revealed the oxidation process as follows:

1. Initial rapid oxidation of both Hf and C within the carbide, resulting in an initially porous oxide scale, reflecting the time-dependent generation of gases during the oxidation process.
2. Thickening of the oxide scale, resulting in diffusional resistance that lowers the interfacial oxygen partial pressure until selective oxidation can occur.
3. Selective oxidation of Hf over C in the system, resulting in O saturation in $HfC_{0.94}$, leading to the formation of a thin, initially amorphous "HfO_2C".
4. Decomposition of the "HfO_2C_x" to HfO_2 + C; the polymorph of HfO_2 present is size-dependent.

5. Coarsening of the HfO_2 + C until oxidation of the C occurs at outer boundary of the interlayer. Porosity in the outer layer of the oxide scale appeared to reflect the volume fraction of carbon present immediately before oxidative removal from the interlayer.

The second paper in this dissertation explored the effect of temperature on the oxidation mechanisms of HfC by oxidizing specimens of $HfC_{0.94}$ from 1668 to 1810°C for 30 minutes under flow of a 1% O_2 / 99% Ar gas mixture in a custom optical furnace. This system comprised four xenon short-arc lamps, focused on the sample located in an atmosphere-controlled chamber. Below ~1800°C, the oxide scale was found to be multi-layered, possessing an HfO_2 outer layer and an HfO_2 + C interlayer. Raman spectroscopy of the interlayer indicated an increase in the order of the graphitic C with increasing distance away from the parent carbide. The crystallite size and interlamellar spacing in the interlayer increased with temperature and distance away from the parent carbide-interlayer distance. Above 1800°C, the oxidation of HfC resulted in HfO_2 without a carbon-containing interlayer. Some porosity was entrained in the scale; however, at the outer surface of the oxide scale, the oxide scale was dense as a result of enhanced densification from a high surface temperature. Thermodynamic analysis of the maximum extent of the "HfO_2 + C" phase stability field in the Hf-C-O system correlates with the observed shift in oxidation regime from gas-phase limited to solid-state limited diffusion studied under these conditions. An increase in the HfO_2/C/HfC_xO_y triple point was calculated versus carbon content, and substoichiometric HfC_x was found to increase the triple point temperature up to 2070°C at x = 0.4. A lower temperature limit was also established on the basis of kinetics of intermediate layer formation, as the formation of a thick two phase scale was not

expected to be realistically described purely using the triple-point because of the expected oxygen potential gradient. For $HfC_{0.94}$, the combination of these two metrics resulted in the predicted range of temperatures where the oxidation mechanism could change as 1687-1815°C.

The third and final chapter of this dissertation sought to determine the enthalpies of formation of HfC_{1-x} and HfN_{1-y} as a function of composition, with the goal of providing reliable assessments of these thermodynamic properties to aid in predictions of material responses under extreme conditions. This was performed by the combustion of spark-plasma sintered HfC_{1-x} (x = 0.049 to 0.247) and HfN_{1-y} (materials in an isoperibol oxygen bomb calorimeter. Enthalpies of formation for HfC_{1-x} materials were found to vary according to the following expression: 261.45x – 257.95 kJ/mol. For HfN_{1-y}, enthalpies of formation were calculated as 367 ± 17 (y = 0.0862) and -331 ± 13 (0.1455) kJ/mol.

3.2. CONCLUSIONS

The following questions were presented in the Introduction section, and will be revisited:

1. What thermodynamic or kinetic driving forces are responsible for the observed oxidation phenomena in HfC?

A combination of thermodynamic and kinetic driving forces is responsible for the observed oxidation phenomena in HfC. Selective oxidation, the thermodynamic result of kinetic limitations of gas diffusion through the pore network of the oxide scale to the carbide-oxide interface, is observed to occur in this system and describes the oxidation behavior of HfC below a composition-dependent temperature. The selective oxidation

behavior is directly responsible for the formation of the intermediate layer during oxidation of HfC.

2. What is the effect of nano-/microstructure on the oxidation behavior of HfC?

The intermediate layer formed upon HfC as a result of selective oxidation contains HfO_2 + C, which forms via the decomposition of a thin, amorphous "HfO_2C_x" band of material surrounding grains of HfC_x. The nanostructure of the HfO_2 + C, and the subsequent pore network in the immediately adjacent outer oxide scale is inherited from this phase decomposition and is generally consistent with porosities used in the gas phase diffusion models in literature.

3. How does temperature affect the mechanisms by which HfC oxidizes?

The oxidation of HfC occurs by two different mechanisms: below ~1800°C, HfC oxidation is controlled by the formation of a carbon-containing interlayer as described above, resulting in gas phase diffusion-limited oxidation kinetics. Above 1800°C, the oxidation of HfC is controlled by solid-state diffusion, as the HfC is directly converted to HfO_2 and gaseous products. The temperature at which this transition occurs appears to be related to the carbon content of the carbide and is calculated to extend as high as 2070°C for highly substoichiometric HfC_xO_y, considering the effect of the anion site occupancy on the triple-point temperature. Considering an alternative metric for scale formation as an arbitrary pO_2 range of one order of magnitude provides a range of temperatures where HfC_x may experience and shift in oxidation regime transition.

The combination of these results synthesizes microstructural observations of the oxide scales to both low- and high-temperature oxidation mechanisms of hafnium carbide and serves to inform design criterions for the use of HfC_x in hypersonic applications; keeping

the interface of the parent carbide and the oxide scale at lower temperatures via cooling or barriers can help circumvent rapid oxidation associated with solid-state diffusion kinetics at higher temperatures, which result in the formation of HfO_2 and gas. Using substoichiometric HfC_x can help to extend the range of service temperatures.

4. FUTURE WORK

Live temperature monitoring would be an extremely beneficial boon for the oxidation process. This currently cannot be done, as a shutter system is required to block out the light of the xenon arc lamps that effectively "poisons" the radiated spectrum of light from the sample. In order to accomplish this, a high-power laser, such as a CO_2 laser, could be used to provide a monochromatic source of energy for heating the sample. This solves a few issues present within the system:

1. It enables real-time temperature measurement using the spectral pyrometer; only one narrow waveband will spike in intensity to the pyrometer, which would be excluded from the calculation of the temperature through the spectral pyrometer's temperature calculation algorithm.
    a. Real-time temperature measurement would also enable the ability for feedback loop controls to be developed for this system, so that precise heating profiles can be implemented for future tests.
2. It protects the lifetime of electronics nearby; currently, the large voltage required to strike the arc for the lamps generates a sufficient magnetic field to generate electromagnetic interference, which has currently manifested as shutting off monitors and stopping the motor controls. This leads to an inability to shutter the

system until a reboot is performed. In addition, the ambient temperature of the room will become lower, as there are no longer 4 xenon arc lamps that need to be cooled by fans.

3. Allows for a more effective optics system through the removal of the shutter plane, which extends the available geometrical configurations for various optics in the system, such as the pyrometer, and also eliminates the need for an off-axis parabolic mirror to view the sample, which obfuscates temperature findings.
4. Allows for higher local heat fluxes, as the laser can be focused to a smaller spot than the lamps.
5. Eliminates the need for complicated electronics and cabling.

In addition to changes in the heating system, there are many potential changes to the sample chamber and holder that could prove a boon to the operation and effectiveness of the instrument. The sample is currently “held” by a simply supported piece of refractory. This is useful for ensuring that the sample is insulated and loses less heat throughout the trial; however, it provides a key failure point during sample testing by preventing consistent, repeatable sample positioning, as well as the potential to crack during heating and coolings. Better insultation of the fiberboard will prevent it from failing as frequently by minimizing the thermal gradient across the piece. A pedestal-based system could also be developed, where the sample is placed on a standoff inside of the sample holder and is fully surrounded by zirconia felt insulation. This provides an insulating environment for the sample while still keeping the insulation itself cool, preventing potential overheating from occurring. There is also potential to explore containerless processing methods for supporting samples.

A proof of concept of containerless processing of the samples was created by machining a 1” stock of 1” diameter aluminum rod to have a cylindrical, 1 mm deep recess. The back end of the rod was bored to create a blind hole that terminated to leave a roughly 1 mm thick region of aluminum between both ends of the piece. Seven 1/16” diameter holes were then drilled into the top of the recessed region to act as small orifices for higher pressure air to escape in a controlled manner, resembling a “pepper shaker”. The back end of the piece was tapped and connected to a low pressure gas regulator. A 4 cm thick, 20 cm diameter billet of HfC was placed on top of the recess, and air was turned to roughly 5 psig, which created a low friction “levitating” effect, similar to a puck on an air-hockey table. Further engineering design would be needed to develop a cooling system for this type of nozzle, as well as further design work on sample geometries that would lead to stable, unmoving samples to create a uniform hot spot on the sample. Aerodynamic levitation could also be employed using a converging-diverging nozzle. The delivery of oxidant gas in this design would be through the high velocity gas used for levitation, and a laser source would be employed to heat the sample in this case. Sample geometries in this instance would be limited to small spheres.

APPENDIX

DEVELOPMENT OF AN OPTICAL FURNACE HEATING APPARATUS FOR USE IN CONTROLLED OXIDATION TRIALS

Essential to the work detailed in this dissertation was the development and operation of an optical furnace capable of heating samples to temperatures in excess of 1700°C in a controlled atmosphere. Atmospheric control is necessary to control the predominant phases during oxidation. To effectively study the oxidation of hafnium carbide, numerous experimental aspects must be accounted for, such as:

1. How to control the atmosphere of a chamber isolated from the heating elements for controlled oxidations.
2. How to effectively heat the sample in an isolated chamber
3. How to measure sample temperature while heating it with focused optical radiation from a xenon short-arc lamp
4. How to cool the heated region of the chamber with the sample effectively

Each experimental aspect required unique design choices to create a reliable, functioning piece of equipment.

This furnace (Supplemental Figure 1) utilized four 6.5 kW xenon short-arc lamps (OSRAM XBO) housed in ellipsoidal mirrors with a focal length of 944.1 mm, oriented at an 18° angle with respect to the vertical axis. The angle can be adjusted using handle wheels connected to ACME thread rods. Each lamp is controlled from a power cabinet, with four power supply units (480V/3 phase) controlled by a touchscreen-enabled programmable logic controller. Each power supply unit contains step-up transformers that generate an

extremely high voltage pulse (>45 kV) to initiate arc formation on each lamp. The high voltage pulse continues to occur multiple times a second until the arc has been struck, after which the voltage dissipates to a lower value to create a stable arc. Each lamp is controlled using a touchscreen interface that displays the active current (I), the active voltage (V), the active power consumption (P, equal to I*V) and the amount of time that the lamp has been in service (T).

The vacuum cube assembly was specifically designed and chosen to decouple the heating of the sample from the sample chamber, when compared to traditional furnace designs. This is necessary to be able to control the oxidation/nature of carbon in the system. Typical gas flow paths in resistively heated furnaces (i.e., graphite furnaces, W furnaces) result in gas-phase equilibration with the heating elements. In the case of many graphite furnaces, which have temperature ranges of interest to the oxidation study, this means that oxygen in the system will be consumed by hot graphite before it can react with the hot sample, reducing the propensity for oxidation of HfC, and potentially leading to a local solid-gas equilibrium between graphitic carbon, CO and CO_2. As a consequence of this, the partial pressure of oxygen in the system can never reach a suitable equilibrium with the HfC, preventing selective oxidation from occurring. In addition, this pins the thermodynamic activity of carbon at 1, preventing investigations into the role of carbon activity on the stabilization of the selective oxidation regime. In the case of W furnaces, the presence of oxygen in the system leads to consumption of the heating elements, similar to graphite furnaces, and the presence of carbon in the system leads to embrittlement of the furnace interior, leading to degradation of the equipment. Thus, it is necessary to isolate the sample from the heating system.

Developing the system required qualifications on each main control system. Qualifying the lamp power density and spot size was performed using a handheld power meter (FLASH-10K-55, Gentec Electro-Optics, Quebec City, Quebec, Canada), in conjunction with 1/8" thick, machined anodized aluminum pinhole apertures of varying diameters that could be placed inside an anodized aluminum aperture holder. Tests were performed with one lamp at a 0° incline at minimum power. The lamp was turned on with the aperture holder placed over the top of the power meter with no apertures, followed by the addition of the largest diameter aperture, working sequentially until the smallest diameter aperture had been inserted. After inserting each plate, the power reading was recorded. This resulted in the data shown in Supplemental Figure 2. The region of uniform power is closest to the center of the spot, and is roughly 0.5 cm in diameter, meaning that **sample surfaces less than 5 mm in size should be uniformly heated**, so long as the optics system is focused and aligned properly. It is important to note that this does not necessarily imply that the sample temperature on the surface will be uniform. For a 4 mm cube shaped sample, assuming that heat transfer of the sample is controlled only by radiative heat transfer, the Stefan-Boltzmann Law can be used to calculate the temperature of the sample:

$$P = \varepsilon \sigma A T^4 \quad (1)$$

Where P is the radiated power (watts), ε is the emissivity of the material surface, σ is the Stefan-Boltzmann Constant (5.67×10^{-8} W/m^2K^4), A is the surface area (m^2), and T is the absolute temperature of the surface at equilibrium (Kelvin). Assuming an emissivity of 0.81 (rough estimate of emissivity of hafnia), for a 4 mm cube face, the top surface equilibrium temperature should be roughly 1325°C at 20% power. Assuming the

convective heat transfer coefficient of argon to be 50 W/m^2K, the effective combined heat transfer coefficient (radiative + convective) is reduced by 17% at this estimated surface temperature. Conductive heat losses are assumed to be negligible due to the small thermal conductivity of the FBD setter plate (0.28 W/mK) and the small contact area with the water-cooled copper (4 corner point contacts).

In addition to the aperture power density tests, another set of experiments was performed using the same lamp, without any apertures, to observe the output power density versus applied lamp power. The results of this experiment are shown in Supplemental Figure 3 for lamp powers ranging from 20% to 60% (reasonable testing ranges for maximizing longevity of the instrument). The maximum output power density from one lamp was 45 W/cm^2. For four lamps operating at 60% power, the maximum output power density of the system is 180 W/cm^2. Using Equation 1 above, for a 4 mm cube the expected surface temperature at 60% applied power on four lamps should be 2230°C. In practice, the surface temperatures that are recorded are lower than the expected temperatures for a variety of reasons:

1. Reflective/transmissive power losses through all of the fused silica windows in the system result in intensity loss (4% per interface).
2. Imperfections in the alignment of the system result in under- or over-focusing for each of the four lamps/reduced overlap between spots of lamps. (major)
3. Uncertainty in the emissivity value of the surface. (major)
4. Reflectance of the gold parabolic mirror can shift the spectrum recorded by the spectral pyrometer, skewing the results of the data. (minor)
5. Convective heat loss as a result of gas flow into the chamber. (major)

The chamber used to hold the sample for controlled oxidation studies is a 1’x1’x1’ square chamber, with an aluminum frame and aluminum face panels. Each face is secured in place with ¼"-20 machine screws and has an O-ring in place for vacuum control. The front and top face plates of the sample chamber have a fused silica window in place of the normal aluminum wall to allow light to transmit through for the incident and the emitted light beams. The back plate and right plate both contain feedthrough ports; KF fittings on the back plate for vacuum connections and CF fittings on the right plate for water and gas feedthroughs. A KF 40 connection on the back plate is used for connecting the exhaust of the chamber to the vacuum control system. A 2.75” CF feedthrough is used for each of the water and gas feedthroughs.

The sample holder comprises a water-cooled copper “hearth”, which is a retrofitted e-beam evaporation target holder (ULVAC EGL-35), that is secured to an aluminum plate. The aluminum plate is screwed onto 4x 4” tall mounting posts for setting the height. The water connections of the hearth are plumbed to the external chilled water supply loop, which supplies ~2.5-5 gallons per minute (gpm) of chilled water through the system, split between the hearth and the pyrometer mirror holder. No water is supplied to the vacuum cube walls, as the test duration is sufficiently short so that the chamber walls do not heat appreciably. Testing for longer durations (overall test time greater than 2 hours) may necessitate cooling of the chamber walls.

The sample is held within the hearth by placing it upon a YSZ setter plate that is simply supported on the four corners by the conical wall of the hearth.

The current method of water-cooled gas delivery is shown in Supplemental Figure 4. The copper plate used for cooling the gas delivery tube has three blind holes drilled into

the plate act as a cooling channel, and also has a clearance thru hole for ¼" tubing drilled through the side. The copper gas delivery tube is inserted into this thru hole. Subsequent tests using this plate were successful in preventing oxidative degradation of the copper plate and tubing.

Because of the geometry of the experimental set-up, i.e., shutter plane is low enough to prevent a pyrometer from directly viewing the sample during light shuttering, a mirror is required to view the sample. A gold-plated off-axis parabolic mirror was chosen, whose focal length was long enough to prevent major occlusion of the light from any lamps, with an angle of 45°. A parabolic mirror was chosen so that collimated rays could be sent to the pyrometer module. The optical configuration, including the mirror and windows were emulated in the calibration of the pyrometer, which used a blackbody furnace at 1000.0°C. Initial experiments in the optical furnace implemented a commercially available uncooled mirror holder, shown in Supplemental Figure 5. Tests implementing this mirror holder failed as a result of excessive heating of the mirror during the trial (Supplemental Figure 6), caused by the mirror slightly occluding the light cone from one of the lamps during the trial. This was ultimately caused by the lack of space in the chamber from size restrictions, in combination with the mirror holder causing the mirror to protrude slightly. The reflective face of the mirror changed color from a golden hue to a purple color. This purple color was likely caused by the formation of a gold-aluminum intermetallic, $AuAl_2$, which tends to appear purple.[39]

A new mirror holder design was created and is shown in Supplemental Figure 7. The new mirror design possessed a u-shaped cooling channel to enable water cooling of the mirror. A 45° flat dummy mirror was installed with thermal paste into the new mirror

holder and heating trials with all four lamps were performed up to 60% applied power. The mirror, even though it partially occluded light from one of the lamps, was intact after the test, proving that the new mirror design was sufficient for keeping the gold off-axis parabolic mirror cool enough for use in trials.

The use of a mirror into the system means only a virtual image of the sample is ever viewed. Reflectivity of the gold surface, as well as absorption/emissivity by the mirror can change as a function of "viewing angle" and temperature, meaning that slight misalignments in the pyrometer and mirror can lead to error in the measured temperature, especially since the focused spot size is close to the size of the sample face. In addition, the calibration of the optical configuration assumes that the mirror exhibits graybody behavior, such that its emissivity does not change as a function of wavelength. For gold, this is a reasonable assumption at the temperature and wavelength ranges of interest; however, this may not hold true for the glass windows used on the sample chamber.

In addition to the experiments performed above, additional experiments were performed to investigate the high temperature oxidation behavior of $HfC_{0.6}N_{0.36}$m as a composition very near to it, $HfC_{0.51}N_{0.38}$, has been predicted to have the highest known melting point of any compound.[40] This material composition was off stoichiometry as a result of carbon pick-up during material synthesis. Scanning electron micrographs of the oxidized specimen are shown in Supplemental Figure 8-9. The $HfC_{0.6}N_{0.36}$ material tended to form a dense oxide scale very near the intserface, with a more porous oxide scale as you proceeded near the outer edge of the scale. Intergranular porosity is also present, which is likely due to the mixed oxidation of C to produce CO/CO_2 gases, alongside the simultaneous liberation of N_2 from the bulk of the material. Raman spectroscopy very near

the interface between the parent material and the oxide scale only indicated the presence of HfO_2, corroborated by XRD only detecting m-HfO_2. Control of the stoichiometry of the material to minimize the amount of off-gassing, alongside a more effective sintering profile to minimize grain growth and to alleviate any residual thermal stresses that may be present could lead to a unique candidate material for extreme environments.

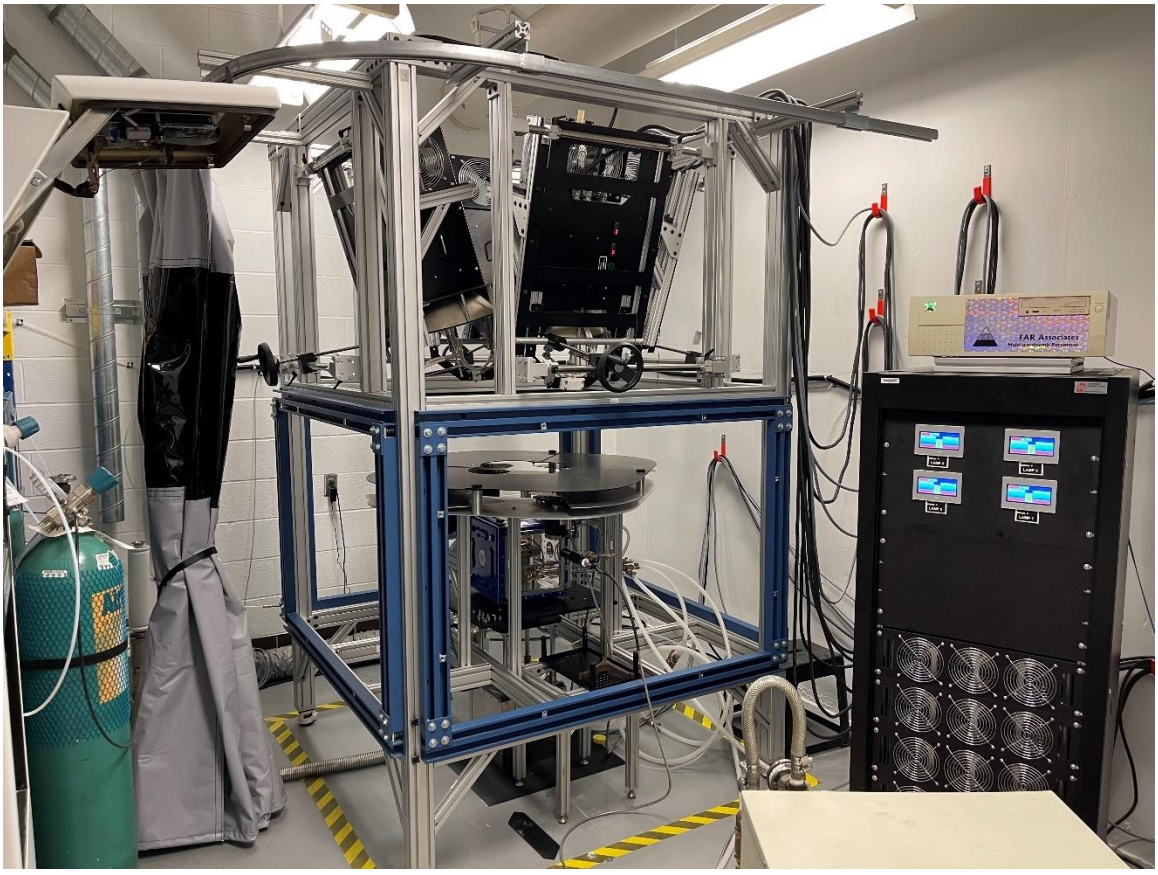

Supplemental Figure 1: Image of the full optical furnace assembly. The power supply cabinet is shown on the right side of the image. In the middle of the image is the actual optical furnace, with the lamps in their housings shown above and the shutter plane and sample chamber shown below.

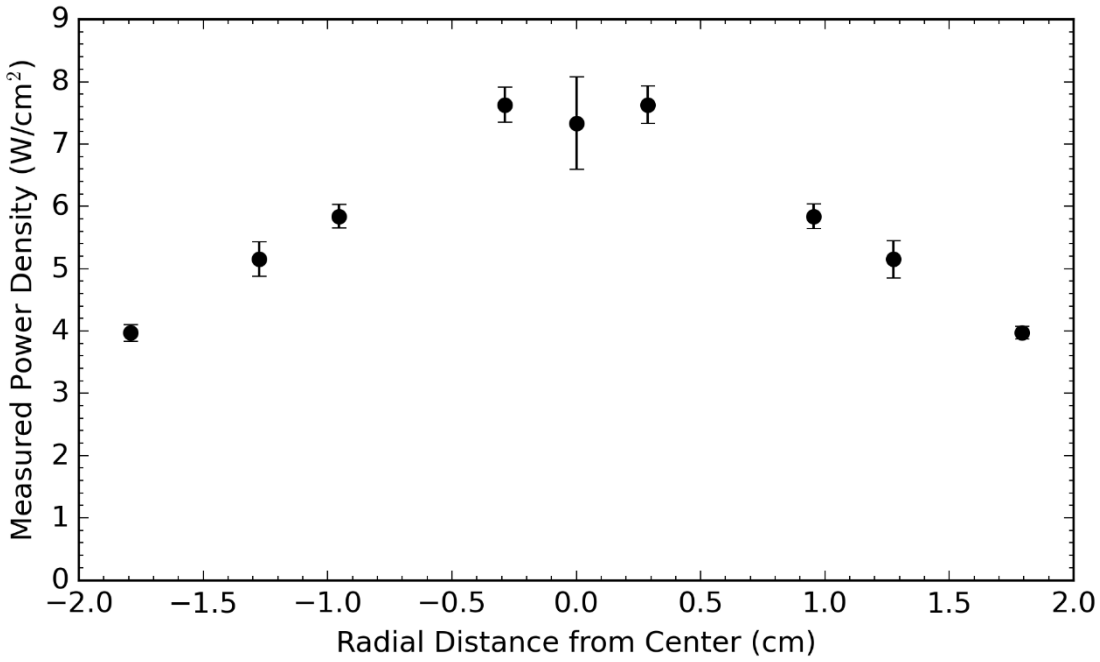

Supplemental Figure 2: Power density versus distance from the center of the spot, determined by the radius of the apertures used. The region of uniform intensity is roughly 0.5 cm in diameter.

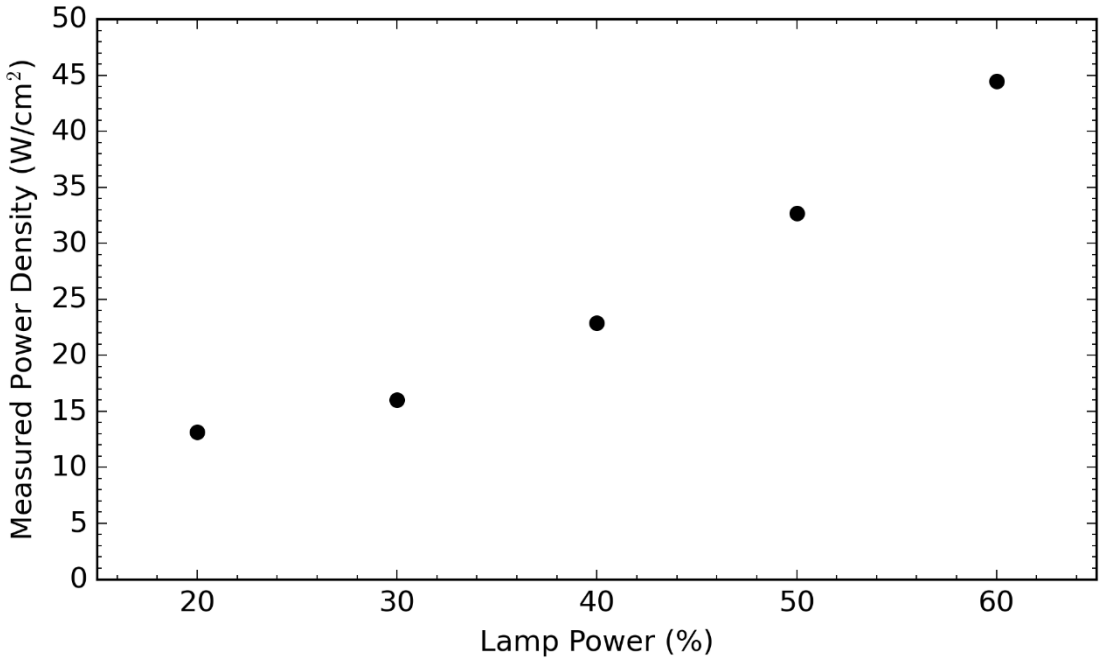

Supplemental Figure 3: Power Density versus % applied power to one lamp.

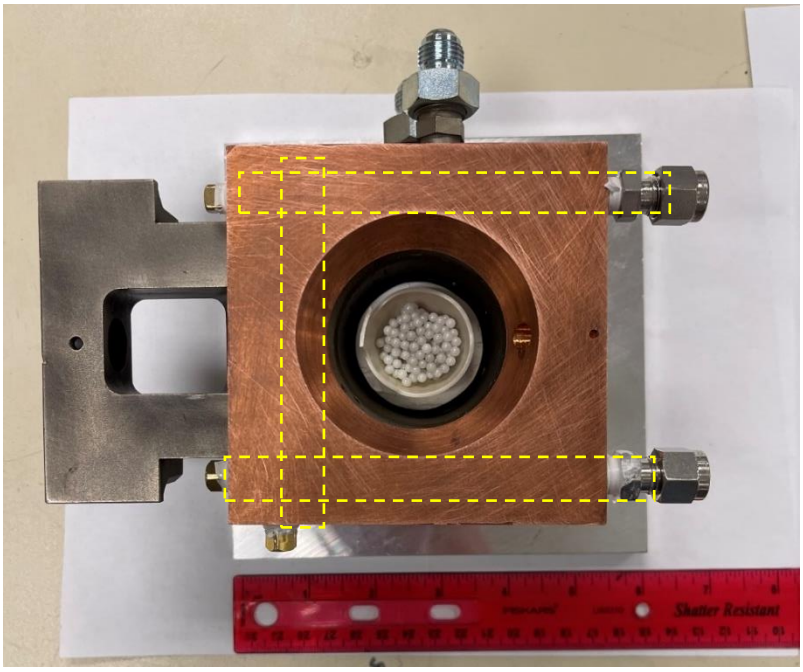

Supplemental Figure 4: Current gas delivery system implementing a u-shaped water cooling path, indicated by the dashed yellow rectangles. The gas delivery tube is inserted into the hole on the right of the copper plate, which sufficiently blocks stray light from reaching the outer wall of the gas delivery tube.

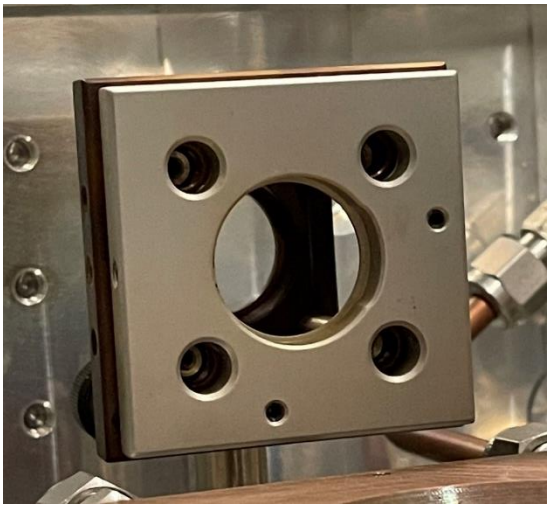

Supplemental Figure 5: Original uncooled mirror holder used in the sample chamber to view the heated sample.

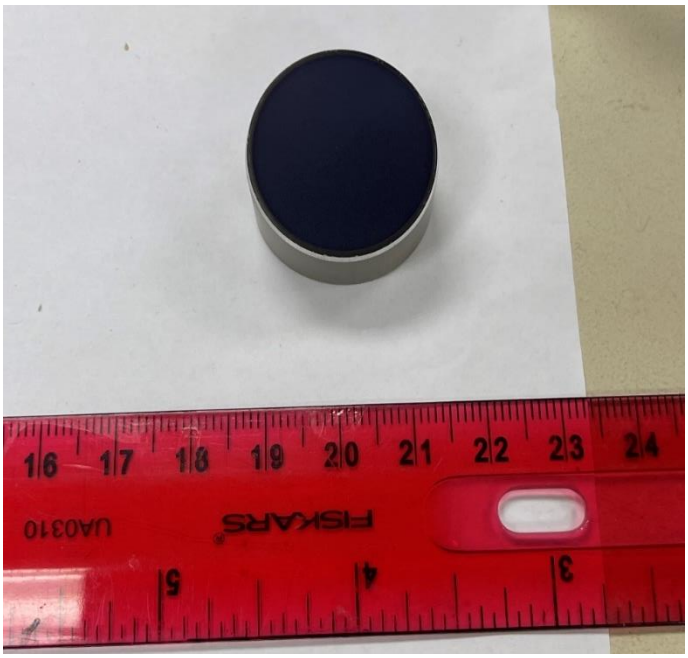

Supplemental Figure 6: Mirror post-trial in uncooled mirror holder. The color of the mirror changed substantially and did not produce reliable temperature data.

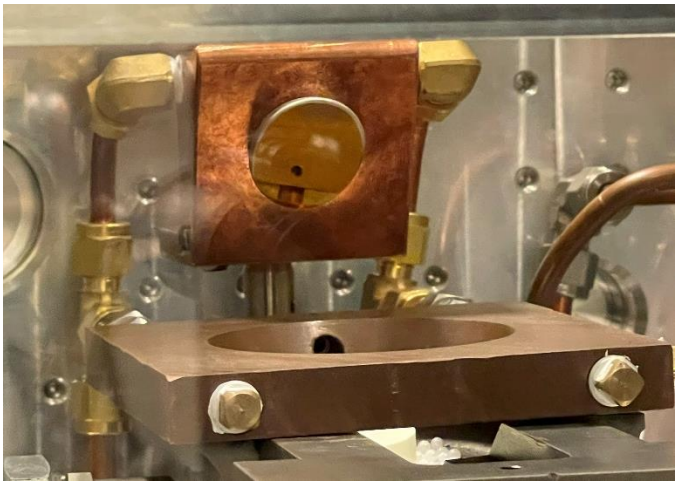

Supplemental Figure 7: New water-cooled mirror holder with a flat mirror installed. Even with the flat mirror partially occluding the light source, the water cooling was sufficient to keep the mirror cool and intact.

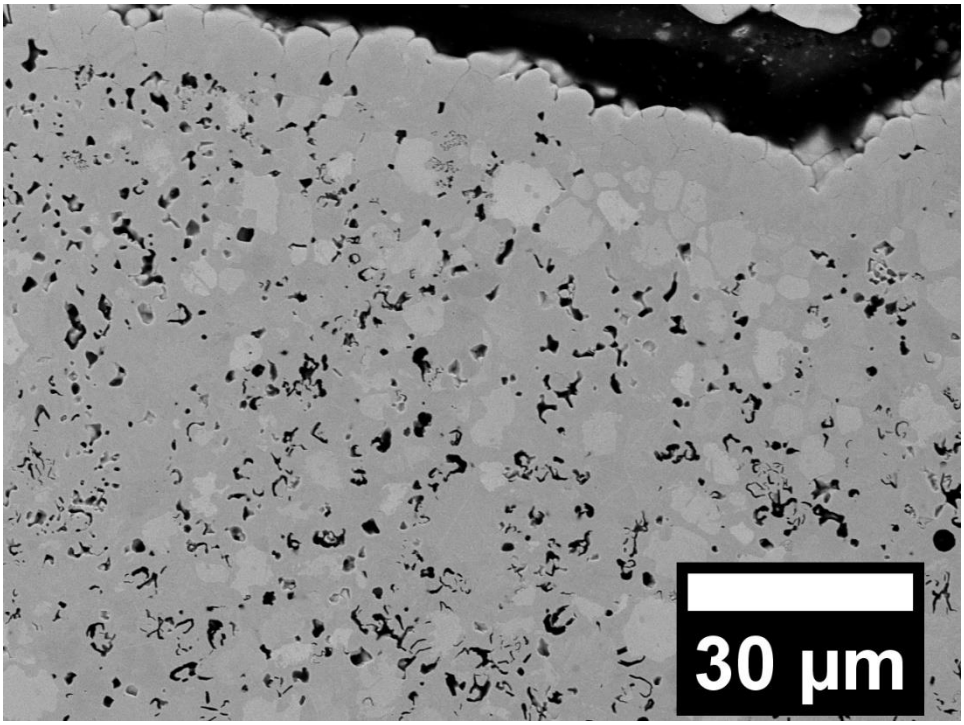

Supplemental Figure 8: $HfC_{0.6}N_{0.36}$ oxidized at 1780°C for 30 minutes. Intergranular porosity with a unique shape is observed, which likely formed as a result of the simultaneous off-gassing of N_2 from the bulk, and transient oxidation of any remnant graphite that may have formed during cooling.

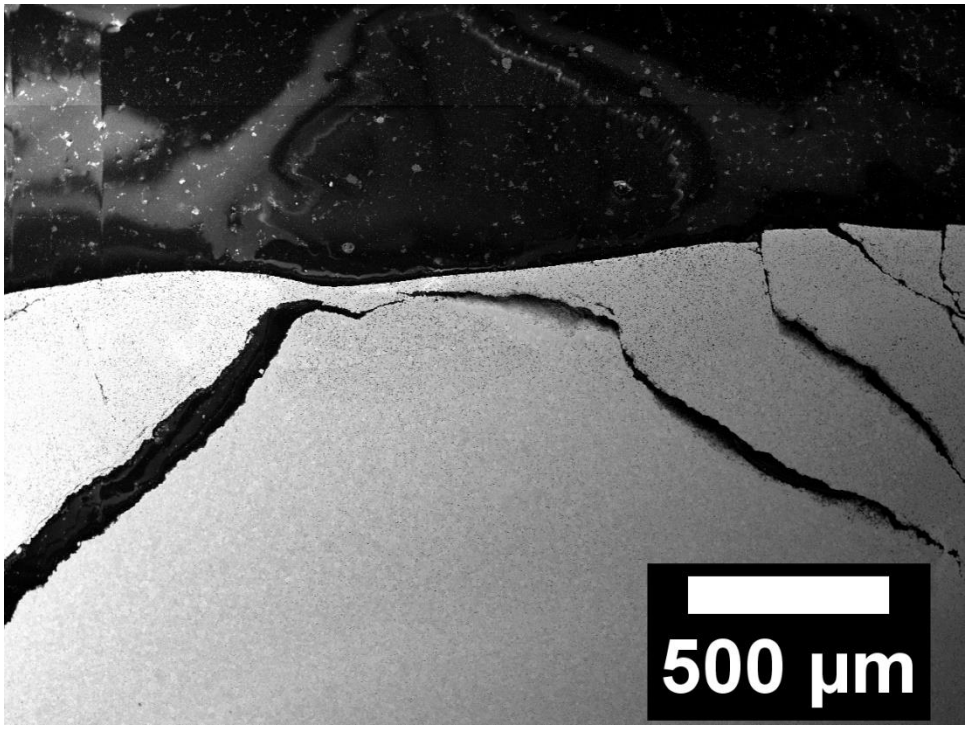

Supplemental Figure 9: Low magnification scanning electron micrograph of $HfC_{0.6}N_{0.36}$ after oxidation at 1780°C for 30 minutes. Extreme damage to the bulk material was observed during oxidation, likely as a result of thermal shock of the material, aided by residual thermal stresses from sintering.

BIBLIOGRAPHY

1. Gusev AI and Zyryanova AN, "Ordering and Magnetic Susceptibility of Hafnium Carbide," in *Phys. Stat. sol. (a)* **177**, pp. 419-437, 2000.

2. Opeka MM, Talmy IG, Wuchina EJ, et al., "Mechanical, Thermal, and Oxidation Properties of Refractory Hafnium and Zirconium Compounds," in *J. Eur. Ceram. Soc.* **19**, pp. 2405–2414, 1999.

3. Okamoto H, "The C-Hf (carbon-hafnium) system," in *Bull. Alloy Phase Diagrams*. **11**, pp. 396–403, 1990.

4. Courtright EL, "A review of fundamental coating issues for high temperature composites," in *Surface and Coatings Technology* **68**, pp. 116-125,1994.

5. Binner J, Porter M, Baker B, et al., "Selection, processing, properties and applications of ultra-high temperature ceramic matrix composites, UHTCMCs–a review," in *Int. Mater. Rev.* **65**, pp. 389–444, 2020.

6. Paul A, Binner J, Vaidhyanathan B, "Ch. 7: UHTC Composites for Hypersonic Applications," in *Ultra-High Temperature Ceramics: Materials for Extreme Environment Applications*, John Wiley & Sons, pp. 144–166, 2014.

7. Harder B, Jacobson N, Myers D, "Oxidation transitions for SiC part II. Passive-to-active transitions," in *J. Am. Ceram. Soc.* **96**, pp. 606–612, 2013.

8. Parthasarathy TA, Cinibulk MK, Opeka M, "Ch. 11: Modeling and Evaluating the Environmental Degradation of UHTCs under Hypersonic Flow," in *Ultra-High Temperature Ceramics Materials for Extreme Environment Applications*, John Wiley & Sons, pp. 267-290, 2014.

9. Okamoto H, "Hf-O (Hafnium-Oxygen)," in *J. Phase Equilibria Diffus.* **29,** pp. 124–124, 2008.

10. Luo X, Zhou W, Ushakov S V., et al., "Monoclinic to tetragonal transformations in hafnia and zirconia: A combined calorimetric and density functional study," in *Phys. Rev. B* **80**, pp. 1–13, 2009.

11. Marnoch K, "High-temperature oxidation-resistant hafnium-tantalum alloys," in *JOM* **17**, pp. 1225–1231, 1965.

12. Shimada S and Yunazar F, "Oxidation of Hafnium Carbide and Titanium Carbide Single Crystals with the Formation of Carbon at High Temperatures and Low Oxygen Pressures," in *J. Am. Ceram. Soc.* **83**, pp. 721–728, 2000.

13. Berkowitz-Mattuck JB, “High-Temperature Oxidation IV. Zirconium and Hafnium Carbides,” in *J. Electrochem. Sci.* **114**, pp. 1030–1033, 1967.

14. Wuchina, EJ and Opeka M, “The Oxidation Behavior of HfC, HfN, and HfB2," in *High Temp. Corros. Mater. Chem. III*. **3**, pp. 136–143, 2001.

15. Bargeron CB, Benson RC, “X-ray microanalysis of a hafnium carbide film oxidized at high temperature*,” in *Surf Coatings Technol.* **36**, pp. 111–115, 1988.

16. Bargeron CB, Benson RC, Newman RW, et al., “Oxidation mechanisms of hafnium carbide and hafnium diboride in the temperature range 1400 to 2100°C,” in *Johns Hopkins APL Tech Dig (Applied Phys Lab.)* **14**, pp. 29–36, 1993.

17. Courtright EL, Prater JT, Holcomb GR, et al., “Oxidation of hafnium carbide and hafnium carbide with additions of tantalum and praseodymium,” in *Oxid Met.* **36**, pp. 423–437, 1991.

18. Holcomb GR and Pierre GRS, “Application of a counter-current gaseous diffusion model to the oxidation of hafnium carbide at 1200 to 1530°C,” in *Oxid Met.* **40**, pp. 109–118, 1993.

19. Voitovich RF and Pugach EA, “High-temperature oxidation of ZrC and HfC,” in *Sov. Powd. Met. and Met. Cer.* **12**, pp. 916-921, 1973.

20. Fischer D and Kersch A, “Stabilization of the high-k tetragonal phase in HfO2: The influence of dopants and temperature from ab initio simulations.,” in *J. Appl. Phys.* **104**, pp. 1-6, 2008.

21. Metcalfe AG, “Gas Evolution During Oxidation of Refractory Borides and Carbides at 1500°C to 2700°C,” in *ECS Trans*. **3**, pp. 131–142, 2007.

22. Scott JA, He X, Lipke DW, “The role of microstructure on high-temperature oxidation behavior of hafnium carbide” in *J. Am. Ceram. Soc.* **106**, pp. 3116–3126, 2023.

23. Skoog DA, Holler FJ, Crouch SR, “Principles of Instrumental Analysis,” College Publisher, 2017.

24. Ferrari AC and Basko DM, “Raman spectroscopy as a versatile tool for studying the properties of graphene,” in *Nat Nanotechnol.* **8**, pp. 235–246, 2013.

25. Ferrari A and Robertson J, “Interpretation of Raman spectra of disordered and amorphous carbon,” in *Phys Rev B.* **61**, pp. 14095-14107, 2000.

26. Ferrari AC, “Raman spectroscopy of graphene and graphite: Disorder, electron-phonon coupling, doping and nonadiabatic effects” in *Solid State Commun.* **143**, pp. 47–57, 2007.

27. Pócsik I, Hundhausen M, Koós M, Ley L, “Origin of the D peak in the Raman spectrum of microcrystalline graphite,” in *J. Non Cryst. Solids.* **227**, pp. 1083–1086, 1998.

28. Cullity BD. “Elements of X-Ray Diffraction,” Addison-Wesley, 1978.

29. Sharma G, Ushakov S V., Navrotsky A, “Size driven thermodynamic crossovers in phase stability in zirconia and hafnia,” in *J. Am. Ceram. Soc.* **101**, pp. 31–35, 2017.

30. Dutta Majumdar J, Manna I, “Laser material processing,” in *Int. Mater. Rev.* **56**, pp. 341–388, 2011.

31. Hennet L, Cristiglio V, Kozaily J, et al., “Aerodynamic levitation and laser heating: Applications at synchrotron and neutron sources,” in *Eur. Phys. J. Spec. Top.* **196**, pp. 151–165, 2011.

32. Riveros-Rosas D, Herrera-Vázquez J, Pérez-Rábago CA, et al., “Optical design of a high radiative flux solar furnace for Mexico,” in *Sol Energy* **84**, pp. 792–800 2010.

33. Sarin P, Yoon W, Jurkschat K, et al., “Quadrupole lamp furnace for high temperature (up to 2050 K) synchrotron powder x-ray diffraction studies in air in reflection geometry,” in *Rev. Sci. Instrum.* 77, pp. 1-9, 2006.

34. Yoon W, Sarin P, Kriven WM, “Growth of textured mullite fibers using a quadrupole lamp furnace,” in *J. Eur. Ceram. Soc.* **28**, pp. 455–463, 2008.

35. Codd DS, Carlson A, Rees J, Slocum AH, “A low cost high flux solar simulator,” in *Sol Energy* **84**, pp. 2202–2212, 2010.

36. Finlayson-Pitts BJ and Pitts JN, “Ch. 16: Applications of Atmospheric Chemistry,” in *Chemistry of the Upper and Lower Atmosphere*: *Theory, Experiments, and Applications,* Academic Press, 2000.

37. Speyer RF, “Thermal Analysis of Materials,” Marcel Dekker, 1994.

38. Araujo A, “Multi-spectral pyrometry - A review,” in *Meas. Sci. Technol.* **28**, 2017.

39. Blish RC, Li S, Kinoshita H, et al., “Gold - Aluminum intermetallic formation kinetics,” in *IEEE Trans. Device Mater. Reliab.* **7**, pp. 51–63, 2007.

40. Hong Q, van de Walle A, “Prediction of the material with highest known melting point from *ab* initio molecular dynamics calculations,” in *Phys. Rev. B* **92**, pp. 1-13, 2015.

VITA

Jonathan Allen Scott was born in Decatur, GA and raised in Bryant, AR. After graduating Bryant High School in 2014, Jonathan began attending Missouri University of Science and Technology studying Ceramic Engineering. During his undergraduate career, he was an active member of Keramos and acted as Treasurer from 2017-2018. He was also an undergraduate researcher in the Ultrahigh Temperature Ceramics Research Group working under Drs. Gregory Hilmas and William Fahrenholtz. He assisted in research on metal-matrix composites, and investigated entropy-stabilized diboride ceramics, focusing on processing-property relationships.

After completing his bachelor's degree in 2018, Jon began pursuing a graduate degree in Materials Science and Engineering. The main focus of his work was on the selective oxidation of hafnium carbide, but assisted in numerous different research projects, such as the characterization of intragranular tungsten-titanium carbide composite ceramics, high pressure aerodynamic levitation, characterization of doped ZrO_2's, and joining of SiC-SiC ceramics. Due to somewhat unforeseen circumstances, Jon left Missouri S&T to begin work as materials engineer at CoorsTek near his hometown in Benton, AR. Somehow, he managed to end up back where he had started.

Jon completed his studies with one paper published, two papers submitted, one poster presentation and three conference presentations. Jon was awarded his Doctor of Philosophy degree in Materials Science and Engineering from Missouri University of Science and Technology in May 2024.